

FACHBEREICH MATHEMATIK UND NATURWISSENSCHAFTEN
FACHGRUPPE PHYSIK
BERGISCHE UNIVERSITÄT WUPPERTAL

Atlas Pixel Opto-Board Production and Analysis and Optolink Simulation Studies

Dissertation zur Erlangung des Doktorgrades
von
Simon Kirichu Nderitu

Die Dissertation kann wie folgt zitiert werden:

urn:nbn:de:hbz:468-20080137

[<http://nbn-resolving.de/urn/resolver.pl?urn=urn%3Anbn%3Ade%3Ahbz%3A468-20080137>]

Abstract

At CERN, a Large collider will collide protons at high energies. There are four experiments being built to study the particle properties from the collision. The ATLAS experiment is the largest. It has many sub detectors among which is the Pixel detector which is the innermost part. The Pixel detector has eighty million channels that have to be read out. An optical link is utilized for the read out. It has optical to electronic interfaces both on the detector and off the detector at the counting room. The component on the detector is called the opto-board.

This work discusses the production testing of the opto-boards to be installed on the detector. A total of 300 opto-boards including spares have been produced. The production was done in three laboratories among which is the laboratory at the University of Wuppertal which had the responsibility of Post production testing of all the one third of the total opto-boards. The results are discussed in this work. The analysis of the results from the total production process has been done in the scope of this work as well.

In addition to the production, a study by simulation of the communication links optical signal has been done. This has enabled an assessment of the sufficiency of the optical signal against the transmission attenuation and irradiation degradation. A System Test set up has been put up at Wuppertal to enhance general studies for better understanding of the Pixel read out system. Among other studies is the study of the timing parameters behavior of the System which has been done in this work and enhanced by a simulation. These parameters are namely the mark to space ratio and the fine delay and their relatedness during the optolink tuning. A bit error rate test based on the System has also been done which enabled assessment of the transmission quality utilizing the tools inbuilt in the System Test. These results have been presented in this work.

Contents

Abstract	I
Contents	IV
Introduction	1
1 Physics Goals at LHC and ATLAS	3
1.1 The Standard Model	4
1.2 The Range of the Fundamental Forces	5
1.2.1 The Electromagnetic Interaction	5
1.2.2 The Weak Interaction	5
1.2.3 The Strong Interaction	7
1.3 The top and the Higgs at LHC	9
1.3.1 The top-quark	9
1.3.2 Properties of the top	9
1.3.3 The top-quark decay modes	10
1.4 The higgs at LHC	12
1.4.1 Higgs production and Analysis	13
2 The LHC and the ATLAS Detector	17
2.1 The Large Hadron Collider	18
2.2 The ATLAS Detector	20
2.2.1 The Muon Spectrometer	21
2.2.2 The Calorimeter	22
2.2.3 The Inner Detector	24
2.2.4 The ATLAS Trigger System	25

3	The ATLAS Pixel Detector	29
3.1	Electronics of the Pixel Detector: The Module	30
3.1.1	The Sensors	33
3.1.2	Radiation Hardness Property by Type Inversion	33
3.1.3	Radiation Hardness Property by Oxygenating Silicon	33
3.1.4	The Sensor Design Features	34
3.1.5	The Deposition of Charge and Signal Generation	36
3.1.6	The Pixel Cell: Design and Operational Features	37
3.1.7	The Module Controller Chip: Design and Operational Features	39
4	The ATLAS Pixel Optolink and the Opto-Board	43
4.1	Introduction	43
4.2	Overview of the Off-detector Electronics	44
4.3	Overview of the On-Detector Electronics	46
4.4	The Link Between the Off-Detector and the On-Detector	46
4.4.1	The Off-Detector TTC Transmission Part (BOC TX)	46
4.4.2	The Off-Detector Data Receiving Part (BOC RX)	48
4.5	The Opto-Board	48
4.5.1	The PiN Diode and the VCSEL Optopacks	50
4.5.2	The ASICs: DORIC and the VDC	51
4.6	The Optical Fibres	56
4.6.1	The Light Signal Coupling	56
5	The Opto-Board Production and Results	59
5.1	Fabrication of the Single Components	61
5.2	The Qualification Specifications	62
5.3	Thermal Characterization Requirements	63
5.4	The Test Set Up	63
5.5	Standardizing the setups	65
5.6	The General Production Measurements Steps	68
5.7	Measurements before Assembly	68
5.8	Measurements After Assembly	71
5.9	After Assembly Functionality Measurements	71
5.10	Quality Assurance Measurements	71

5.10.1	Burn-in Testing	71
5.10.2	Thermal Cycling	73
5.10.3	Full Characterization	74
5.10.4	The Optical Characterization at 10°C	78
5.10.5	The Optical Characterization at optoboard -10 °C	79
5.10.6	The Optical Power Measurement at Saturation	81
5.11	Conclusion	83
6	The Optical Power Calculation	85
6.1	The Components in Consideration	85
6.2	Calculation Strategy	86
6.3	Attenuation and Irradiation Effects	88
6.3.1	Total Attenuation	91
6.4	Power Loss Due to Irradiation	92
6.5	The Data Link Optical Power Calculation	94
6.5.1	The RX-plugin Working Range	94
6.5.2	The Optical Power	96
6.5.3	The Minimum Optoboard Power Required	99
6.5.4	Opto-boards with an Optical Power Dispersion	100
6.6	The TTC Link Optical Power Calculation	103
6.7	The TTC Limits	107
6.8	Conclusion	109
7	Timing Characteristics and Bit Error Rate	111
7.1	The System Test at Wuppertal	112
7.2	The Parameters Concerned	113
7.3	The General Procedure of the Study	113
7.4	The Tuning Process	114
7.5	Expected Effect	114
7.6	The Mark-Space Ratio	115
7.6.1	The MSR and the RX-Threshold	118
7.7	The Fine Delay	119
7.8	The Inter-relation between MSR and the Fine Delay	121
7.9	The Optimum MSR Settings when No Fine Delay is Applied	123

7.10 The Opto-board PiN Current in relation to MSR and the Fine Delay settings 125
7.11 The Interplay of Parameters and Tuning 125
7.12 Bit Error Counting in the System Test 126
7.13 Conclusion 129

Conclusion 131

List of Figures 133

List of Tables 137

Bibliography 139

Given that a settled position was reached on design of the first phases of operation the production and integration of the components has been the prevailing activity within the last 2 years. The components had to be strictly assessed each step during the production process against the detector design set standards.

This work is concerned with the ATLAS detector and specifically within the data transmitting system, the optical link, of the Pixel detector positioned in the innermost part (within $R=15$ cm of the beam line) of the ATLAS detector. The system is utilized in transmitting the timing trigger and control signals (TTC) to the Pixel detector and module particle hit data back to the off detector electronics for analysis. The technology of optical transmission of data (opto-link) has the key advantage in offering a non magnetic solution thus avoiding perturbation in the magnetic field. It also offers a fast readout over long distance, proper decoupling of the detector-end electronics and the off-detector electronics and no cross talk.

The opto-board which is an interfacing optical electronic component of the opto-link on the detector-end has undergone production and testing. The results are discussed in chapter 5. An optical power calculation of the optical link has been performed with an aim to know the quality of the optical signal against fiber attenuation and irradiation effects thus assessing sustainability of functionality up to 10 years. In addition a simulation on timing has been performed in order to enlighten on the timing characteristic and the parameters involved that the process of data taking may be optimized. These issues have been discussed in chapter 6 and 7. A result of bit error rate count given within the system test is discussed as a section in chapter 7.

Chapter 1

Physics Goals at LHC and ATLAS

Introduction: Physics at LHC

As already mentioned the LHC experiments will offer the opportunity to explore particle physics at the TeV energy scale. Among the models of particle physics, the Standard Model of Particles and Forces (SM) has been most successful in describing the constituents of matter and the forces keeping them together. This model has been precisely tested at low energy scales and confirmed by the data collected by many particle physics experiments among them the Large Electron Positron Collider (LEP) at CERN and the Tevatron^a. However at the TeV scale the model needs extensions to explain new phenomenas arising from normalization requirements to the SM. In this chapter the SM is discussed and in addition the issues remaining to be tested regarding the *top – quark* mass precision measurements and the Higgs discovery are discussed. In general at LHC, among the many points, the following specific points will be explored:

1. Further study of the B-hadrons physics and the charge and parity violation in their system.
2. Search for the SM Higgs above the limit set by LEP (115.6 GeV) [2]
3. Precisely measure the W mass of $WW\gamma$ and WWZ Triple Gauge Couplings and of the mass, the couplings and the decay properties of the *top – quark*.
4. More QCD measurements such as the running of the strong coupling constant α_s over a wide range of Q^2 offered by the energy scale at LHC.
5. Test the extension models and as well seek to resolve the hierarchy problem in the SM. The Higgs mass parameter μ receives quadratically divergent one loop radiative corrections namely:

^aThe main collider in Fermilab in the United States

- (a) The top loop $\approx 2 TeV^2$.
- (b) The W/Z loops $\approx -750 GeV^2$.
- (c) The Higgs loop $\approx -1.25 m_h^2$.

at the quantum level and hence is very sensitive to ultraviolet physics. Thus normalization in the Higgs sector is expected to give rise to new physics.

1.1 The Standard Model

The Standard Model (SM) predicts that matter is made of two kinds of elementary particles. These are the point-like quarks and leptons. The force exchangers between the particles are called bosons. The quarks are six positioned into three generations according to mass and charge properties.

Generation	Leptons			Quarks		
	Flavour	Charge	Mass (GeV)	Flavour	Charge (e)	Mass(GeV)
1 st	ν_e	0	$<3 \cdot 10^{-9}$	u	2/3	1 to $5 \cdot 10^{-3}$
	e	-1	$511 \cdot 10^{-6}$	d	-1/3	3 to $9 \cdot 10^{-3}$
2 nd	ν_μ	0	$<0.19 \cdot 10^{-3}$	c	2/3	1.15 to 1.35
	μ	-1	$105.7 \cdot 10^{-3}$	s	-1/3	75 to $170 \cdot 10^{-3}$
3 rd	ν_τ	0	$18.2 \cdot 10^{-3}$	t	2/3	172.5 ± 2.3
	τ	-1	1.777	b	-1/3	4.0 to 4.4

Table 1.1: *The mass and the charge of the Standard Model elementary particles. The particles consist of three generations for both the quarks and the leptons. [3].*

Shown in Table 1.1 is a summary of the SM particles. In the quark sector the *up – quark* is the lightest and the *top – quark* is the heaviest. In the lepton sector the charged three are the electron (e), the muon (μ), and the tau (τ). The neutral three are the electron neutrino (ν_e), the muon neutrino (ν_μ), and the tau neutrino (ν_τ) which got no known mass hierarchy, but exactly three generations have been shown to exist [4,5] by LEP data.

The general picture given by SM of matter constitution is that all stable matter is composed of the first generation of particles (see Table 1.1). The interaction among these particles is governed by 4 fundamental forces namely the electromagnetic force mediated by the photon γ , the weak force mediated by the W^\pm and Z bosons and the strong force mediated by 8 gluons. For completion, though not really apart of SM, is the force of gravity predicted to be mediated by the gravitons which have not yet been observed.

1.2 The Range of the Fundamental Forces

The strength of the forces is reflected by the coupling constant α which is dimensionless. Table 1.2 summarizes the coupling constants of the the fundamental force interactions excluding gravity.

Interaction	Strength	Boson	Electric charge	mass(GeV)
Electromagnetic	$\alpha=1/137$	γ	0	0
Weak	$\alpha_w=1/29$	W^\pm	± 1	80.450 ± 0.058
		Z	0	91.1876 ± 0.0021
Strong	$\alpha_s=0.1$	8 gluons	0	0

Table 1.2: *The dimensionless constant α showing the strength of the fundamental forces. [3].*

A brief outlook of each of these forces of interaction is discussed in the following sections.

1.2.1 The Electromagnetic Interaction

Quantum ElectroDynamics (QED) is the gauge theory that describes the electromagnetic force. The QED langragian is:

$$\mathcal{L}_{QED} = i\bar{\Psi}\gamma^\mu D_\mu\Psi - m\bar{\Psi}\Psi - \frac{1}{4}F_{\mu\nu}F^{\mu\nu} \quad (1.1)$$

where:

$$D_\mu = \partial_\mu - ieA_\mu(x) \quad (1.2)$$

which is the covariant derivative due to local gauge invariance [6]. The strength of the field tensor that describes the propagating field A^μ is given by

$$F_{\mu\nu} = (\partial_\mu A_\nu - \partial_\nu A_\mu) \quad (1.3)$$

The exchange particle is the photon, that is linked to this propagating field. The electromagnetic force acts on every charged particle. According to Feynman rules the terms that are quadratic in Ψ describe the fermions propagators while those quadratic in A describe the photon propagator, the exchange particle and the terms quadratic in Ψ and linear in A describe the interaction between fermions and the photon. These features are graphically illustrated in Figure 1.1 which shows the Feynman diagrams.

1.2.2 The Weak Interaction

All particles interact weakly through the mediation of the massive gauge bosons W^\pm and the Z . The mass of W^\pm is

$$m_W = (80.403 \pm 0.029) \text{ GeV}/c^2 \quad (1.4)$$

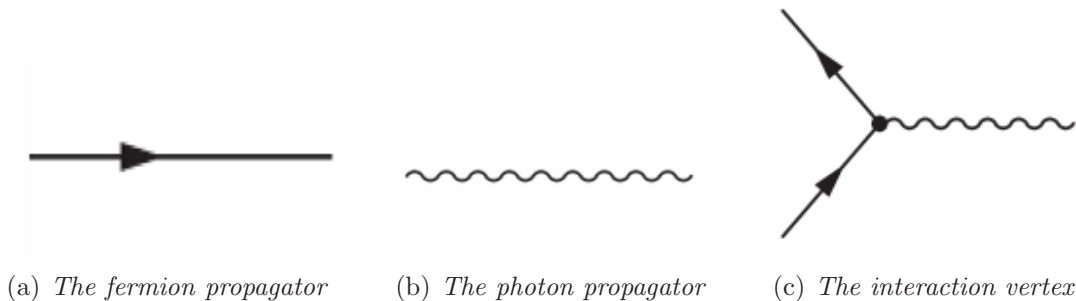


Figure 1.1: *Feynman graphs illustrating the interaction in the QED gauge theory.*

and the mass of the Z is [7]

$$m_Z = (91.1876 \pm 0.0021) \text{ GeV}/c^2. \quad (1.5)$$

Because of their massiveness, the lifetimes of the gauge bosons are small thus resulting to a short interaction-length a characteristic of the weak interaction.

In the Standard Model, the electromagnetic and the weak interaction was unified to electroweak theory basing on the $SU(2) \otimes U(1)$ group [6]. This is one of the commendable successes in the Standard Model. The local gauge invariance results to four gauge bosons: the B from the $SU(1)$ group and the W^1, W^2 and W^3 from the $SU(2)$ group. The W^1 and W^2 couple to form the gauge bosons W^+ and W^- as in equation below

$$W_\mu^\pm = \frac{1}{\sqrt{2}} (W_\mu^1 \mp iW_\mu^2) \quad (1.6)$$

The mixing of W^3 and B according to the Weinberg angle Θ_W leads to Z_μ and A_μ

$$Z_\mu = \cos\Theta_W W_\mu^3 - \sin\Theta_W B_\mu \quad (1.7)$$

$$A_\mu = \sin\Theta_W W_\mu^3 + \cos\theta_W B_\mu \quad (1.8)$$

final states and exchange particles Z^0 and $\gamma(A_\mu)$. It is in this sector that the higgs particle is postulated resulting from the fact that there is spontaneous symmetry breaking yielding to the massive W^\pm , the Z bosons and a massless photon. This process is the Higgs mechanism. As a result there is a weak isospin doublet of complex Higgs field:

$$\Phi(x) = \frac{1}{\sqrt{2}} \begin{pmatrix} \Phi^+ \\ \Phi^0 \end{pmatrix} \quad (1.9)$$

The weak boson of the electroweak theory couples to this field.

The spontaneous symmetry breaking process postulates a neutral scalar Higgs particle H^0 , the only particle not observed in the Standard Model. Searches were carried out

at LEP in the year 2000 at a center of mass energies higher than 205 GeV. An LEP experiment, ALEPH, reported an excess of about 3σ arising from signatures suggesting a Higgs boson with mass ≈ 115 GeV. The LEP data provides a 95% confidence level lower bound of $114.4 \text{ GeV}/c^2$ to the Higgs mass [2,4]. A further discussion on the Higgs physics will be done in the next sections.

1.2.3 The Strong Interaction

The Quantum Chromodynamics (QCD) is the gauge theory of strong interaction. It is based on the symmetry $SU(3)_C$ group explains the strong force. The C represents the color and the 3 refers to the three possible color states of the quarks. It is assumed to be in the fundamental representation of the group having dimension three. It is only limited to the quark sector.

The three color flavors are red, green and blue standing for the quarks q and the anti colors, anti-red, anti-green and anti-blue, standing for the anti-quarks \bar{q} . This force is mediated by 8 gluons which couple to the three flavors. The QCD Lagrangian sums this as follows

$$\mathcal{L}_{QCD} = \bar{\Psi} (i\gamma^\mu \partial_\mu - m) \Psi - g_s \sum_a (\bar{\Psi} \gamma^\mu T_a \Psi) G_\mu^a - \frac{1}{4} \sum_a G_{\mu\nu}^a G_a^{\mu\nu} \quad (1.10)$$

where g_s is the coupling constant and T_a the fundamental description of the symmetry group, with a being the eight generators of $SU(3)$. The $G_{\mu\nu}^a$ describe the gluons as gauge fields [6].

The experimental data has confirmed the existence of three color flavours by measuring the R ratio of the e^+e^- decay to quarks and to muons as shown below [3].

$$R = \frac{\sigma(e^+e^- \rightarrow q\bar{q})}{\sigma(e^+e^- \rightarrow \mu^+\mu^-)} \quad (1.11)$$

Where

$$R = 3 \sum_q e_q^2 \quad (1.12)$$

and the factor 3 represents the colors.

The Feynman diagrams in Figures 1.2 show the quark and gluon propagator and the interaction vertexes. The gluons have a color and anti-color. They hence do self interact as shown by the self-interaction vertexes 1.2(d) 1.2(e). For this reason the interaction strength increases with increase in interaction length explaining non existence of free quarks.

The quarks do mix according to a 3×3 parameterized matrix known as Cabibbo-Kobayashi-Maskawa matrix (CKM), a unitary V_{CKM} matrix parameterizing the weakly charged current interactions of the quarks [6]

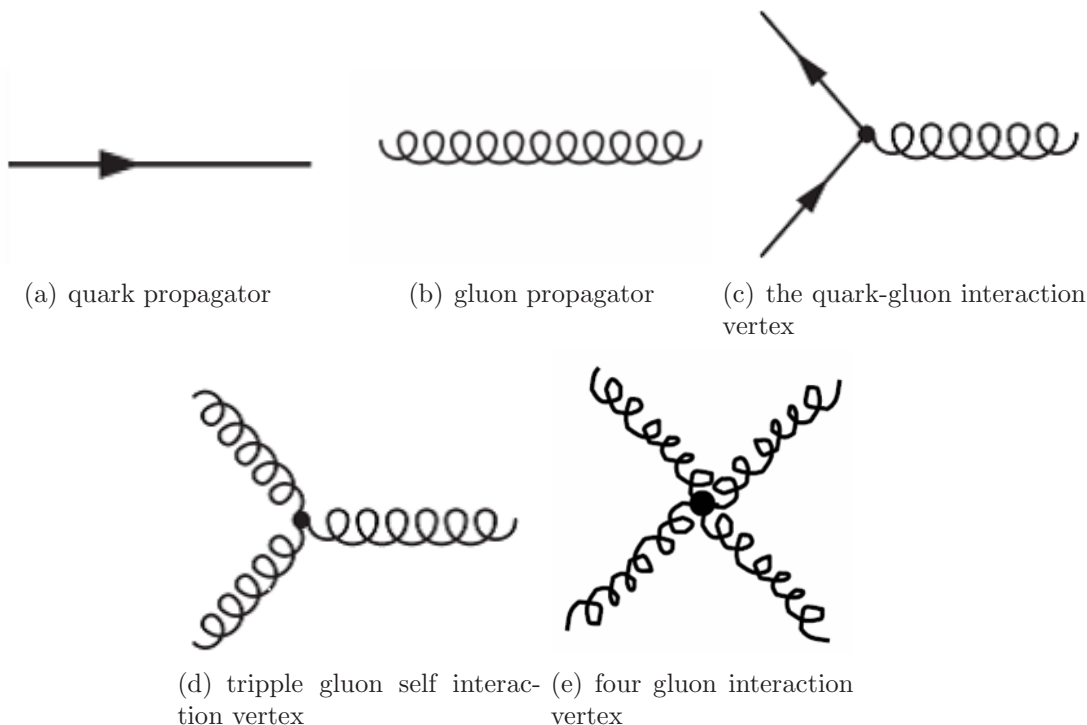


Figure 1.2: *Feynman graphs showing the interactions in the QCD $S(U3)$ group [6].*

$$\begin{pmatrix} d' \\ s' \\ b' \end{pmatrix} = \begin{pmatrix} V_{ud} & V_{us} & V_{ub} \\ V_{cd} & V_{cs} & V_{cb} \\ V_{td} & V_{ts} & V_{tb} \end{pmatrix} \begin{pmatrix} d \\ s \\ b \end{pmatrix} \quad (1.13)$$

However, the Standard Model does not predict the constituents of the CKM matrix hence the values of the individual matrix are determined from the weak decays of the relevant quarks. Four parameters describe the unitary matrix and the standard parameterizations utilizes three angles and one phase. Table 1.3 shows the matrix elements.

0.9741 to 0.9756	0.219 to 0.226	0.0025 to 0.0048
0.219 to 0.226	0.9732 to 0.9748	0.038 to 0.044
0.004 to 0.014	0.037 to 0.044	0.9990 to 0.9993

Table 1.3: *CKM quark-mixing matrix at 90% C.L from a global fit to angles and phase [3].*

As the matrix is required to be unitary, one possible unitarity test of the matrix is by

$$|V_{ud}|^2 + |V_{us}|^2 + |V_{ub}|^2 = 1 - \Delta \quad (1.14)$$

from the top row in equation 1.14. In the SM the Δ in Equation 1.14 is zero. At present this condition is poorly satisfied in which the unitarity fails by up to 2.7σ [8]. The origin of the deviation is unclear. This is one of the issues to be researched at LHC.

1.3 The top and the Higgs at LHC

The further understanding of the *top – quark* and the search of the Higgs constitute key physics points to be tackled at the LHC by the ATLAS Experiment, therefore the physics involved will be discussed briefly.

1.3.1 The top-quark

The *top – quark* was discovered in 1995 at Tevatron proton-antiproton collider. From run II of Tevatron, the *top* mass is $172.5 \pm 2.3 \text{ GeV}/c^2$ [9,10] making it the heaviest fundamental particle. The top mass is a fundamental parameter in SM precision measurement thus important. An accurate value of the *top – quark* and the *W* boson mass will help to provide a consistency check thus constraining the Higgs mass. It will also lead to searching for new physics related to electroweak symmetry breaking. The decays also offer a sensitive probe for the presence of additional gauge bosons beyond the *W* and *Z* boson of the SM. Such additional gauge bosons \hat{W} and \hat{Z} typically arise in extensions to the SM from the presence of additional symmetry groups [11]. Thus the top mass and the couplings offer an open window for further searches.

1.3.2 Properties of the top

In hadron collisions, the top quarks are produced dominantly from the QCD processes $qq \rightarrow t\bar{t}$ and $gg \rightarrow t\bar{t}$. At ATLAS the main mode of production is by gluon to gluon fusion that has a decay probability of 90% thus making LHC a *top* factory. The Figures in 1.3 a-d, show the Feynman diagrams of the *top – quark* production through the QCD processes of gluon to gluon interaction.

Within the SM the top almost exclusively decays to b-quark and W bosons pairs as shown in Figure 1.4. It has a short life time (10^{-24} s).

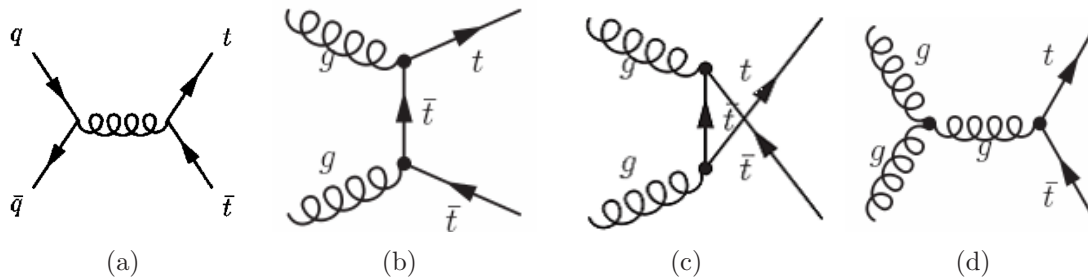


Figure 1.3: *The lowest order top–quark production QCD processes Feynman graphs. The main method of production in ATLAS is by gluon to gluon fusion [12].*

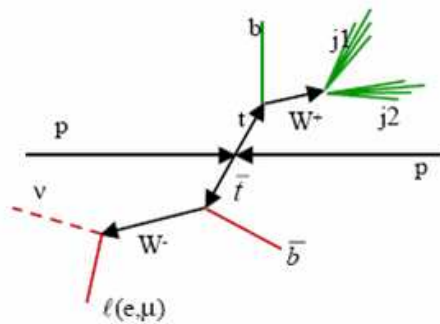


Figure 1.4: *The main top decay mode of $t \rightarrow W + b$. In addition it is shown the W decaying to leptons and jets.*

1.3.3 The top-quark decay modes

Depending on the decay modes of the W^\pm bosons from the $t\bar{t}$ pair, there is a categorization into 3 decay channels: The decay to 2 leptons (either electrons or muons) and neutrinos, referred to as the di-leptonic channel. In the di-leptonic mode, there is a case where the decay of the W bosons has a tau lepton (τ) involved. In this case the W bosons decays to a tau and a tau neutrino where the tau decays into hadrons or into leptons. The decay to all jets referred to as the hadronic channel. The decay to a mixture of electrons or muons and jets is referred to as the semileptonic channel. Figure 1.5 shows the branching ratios of these decays.

In the Di-lepton channel both of the W bosons decay leptonically with a branching ratio BR of $2/9 \times 2/9 \approx 5\%$. In the semileptonic channel the BR of $2 \times 2/9 \times 6/9 \approx 30\%$. In the hadronic decay the BR $\approx 6/9 \times 6/9 \approx 44\%$. The decay of the W bosons that involves a tau lepton (τ) occurs with a BR $\approx 20\%$. For many cases of physics analysis the trigger is mainly on electrons or muons. Table 1.4 summarizes the 4 distinguishable decay mode topologies. During analysis the e and the μ are usually combined.

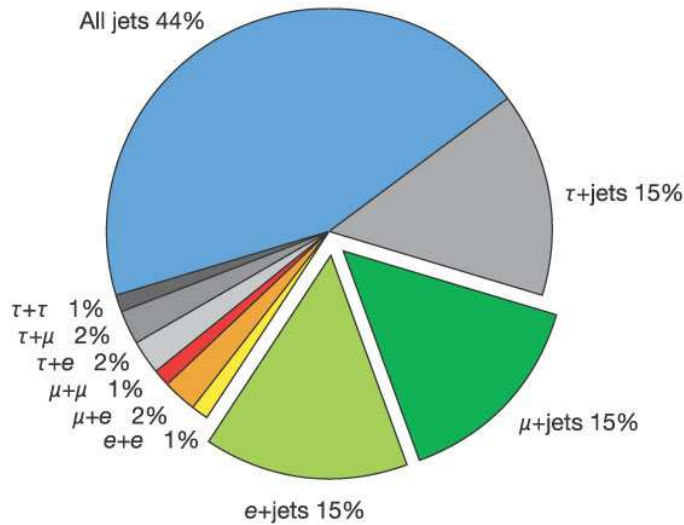


Figure 1.5: The $t\bar{t}$ branching ratios and the final states [12].

Decay Mode	Branching Ratio	Final topology
leptonic	5%	$t\bar{t} \rightarrow W^+bW^-b \rightarrow l^+\nu b l^-\bar{\nu}b$
$\tau + X$	21%	at least one of the W decays to $\tau + \nu_\tau$
semi-leptonic	30%	$t\bar{t} \rightarrow W^+bW^-b \rightarrow l^+\nu q\bar{q}b$
hadronically	44%	$t\bar{t} \rightarrow W^+bW^-b \rightarrow q\bar{q}bq\bar{q}b$

Table 1.4: The $t\bar{t}$ quark branching ratios and the topologies. The leptonic channel mainly refers to the decay to electrons and muons which is most utilized in analysis. The decay involving τ leptons is categorized on its own.

Analysis in the Dileptonic channel

The dilepton events are characterized by two high transverse momentum (p_T) isolated leptons, large traverse missing energy, E_{miss}^T and two jets coming from the fragmentation of the b-quarks. The background is mainly from Drell-Yan processes and $Z \rightarrow \tau\tau$ associated with jets, and from WW +jets and $b\bar{b}$ production.

In ATLAS, events can be selected by requiring two opposite sign isolated leptons with $p_T > 35$ GeV and $p_T > 25$ GeV respectively within $|\eta| < 2.5$, $E_{miss}^T > 40$ GeV, and two jets with $p_T > 25$ GeV. The dileptonic channel has signal over background ratio of ≈ 10 [13].

Analysis in the Semi-leptonic Channel

The lepton plus jets channel is probably the most promising channel for an accurate determination of the *top-quark* mass. Three methods to measure the top mass are used.

First the top mass can be deduced from the three jets invariant mass of the hadronic *top* decay. A second method is where the entire $t\bar{t}$ system is fully exploited to determine the top quark mass from a kinematic fit. The last method is where the top mass is determined from a kinematic fit, but the jets are reconstructed using a continuous algorithm. The *b* – *tagging* in this channel helps to improve the signal over the QCD background. In ATLAS, a selection with high rejection of the background can be obtained by using the following requirements: one isolated lepton with $p_T > 20$ GeV, $E_{miss}^T > 20$ GeV, and at least four jets reconstructed with a jet cone size of $\Delta R = 0.4$ with $p_T > 40$ GeV and $|\eta| < 2.5$, of which at least two are tagged as b-jets [13].

Analysis in the Hadronic Channel

The all jets channel final state consists of six jets which includes two b-jets, no high p_T leptons, and small E_{miss}^T . This is in the absence of initial or final state radiation. There are no energetic neutrinos in the final state, the all hadronic mode is the most kinematically constrained of all the $t\bar{t}$ topologies, but it is also the most challenging to measure due to the large QCD multijet background. To obtain a clean sample, events can be selected in which both reconstructed *top* and *antitop* quarks have a transverse momentum $p_T > 200$ GeV.

1.4 The higgs at LHC

In this section the discussion is limited only to the Standard Model (SM) higgs which postulates a light Higgs particle of ≈ 115 GeV. Extension to SM predict the existence of massive and charged higgs particles within which there is rise to other massive *W* and *Z* bosons. As mentioned in section 1.3.1 one of the physics program at ATLAS, LHC is to search for the SM Higgs particle. In order to solve the existence of a mass term $M^2 A_\mu A^\mu$ that is not local gauge invariant under transformation $A_\mu \rightarrow A_\mu - \delta_\mu \kappa$, it was postulated that the massless gauge bosons results to massive gauge bosons by an algebraic transformation. The Lagrangian of a simple Abelian case is: [14, 15]

$$\mathcal{L} = (D_\mu \phi)^* (D^\mu \phi) + \mu^2 \phi^* \phi - \lambda (\phi^* \phi)^4 - \frac{1}{4} F_{\mu\nu} F^{\mu\nu} \quad (1.15)$$

The ϕ in Equation 1.15 is a complex scalar field and is A_μ a massless gauge boson. The parameter are constrained by $\lambda > 0$, to assure a lower bound, and $\mu^2 > 0$. The $F^{\mu\nu} = \partial^\mu A^\nu - \partial^\nu A^\mu$ is the antisymmetric tensor of the boson field. Under a local gauge transformation, the invariance of the theory is guaranteed if, in the Lagrangian, the covariant derivative:

$$D^\mu = \partial^\mu + igA^\mu \quad (1.16)$$

is used instead of the ordinary derivative ∂^μ . Thus the potential for the scalar field has its minimum at $\phi = \sqrt{\frac{\mu^2}{2\lambda}}$ as illustrated in Figure 1.6. The field ϕ can be expanded around

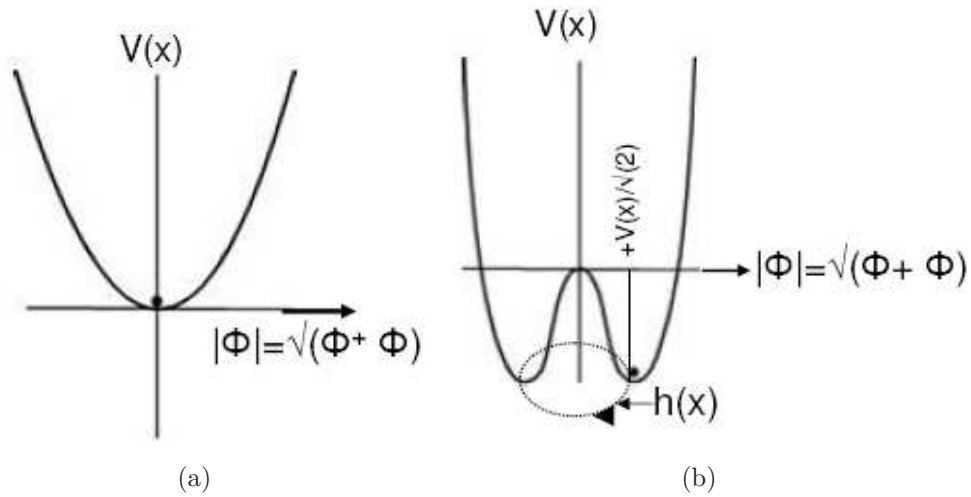


Figure 1.6: *The higgs scalar potential before transformation (a) and after transformation (b): It has a minimum value at $\phi = \sqrt{\frac{\mu^2}{2\lambda}}$. [15]*

its minimum thus leading to a continuous minimum region defined by

$$\phi = \frac{[v + h(x)]}{\sqrt{2}} \quad (1.17)$$

where $h(x)$ is a real field.

When Equation 1.17 is substituted back to the Lagrangian, it results into a term representing the mass of the gauge boson Z , a term for the W^\pm , a term for the massless photon and a mass term for the scalar boson - the Higgs and the interaction terms with the related strength. Referring again to Figure 1.6, the value ϕ , the Higgs field, acquires a non zero vacuum expectation value at a point on the circle of minimum away from $\phi=0$ thus the symmetry is spontaneously broken giving mass to the bosons. This is known as the Higgs mechanism. The SM-Higgs is the only remaining parameter, in the SM, which has not been observed. Since the W and the Z bosons have already been discovered and their masses determined, there is therefore strong expectation for the discovery of the Higgs.

1.4.1 Higgs production and Analysis

At hadron colliders the most important production processes are by: gluon fusion $gg \rightarrow h^0$, in association with the vector boson $W^\pm h^0$ or $Z^0 h^0$ or with a *top* quark pair ($t\bar{t}h^0$) and the W^+W^- processes (qqh^0 or $q\bar{q}h^0$).

At LHC the main channels to be used for h^0 discovery can be classified as those in the low mass region ($m_{h^0} \leq 130$ GeV), those in the mid region ($130 \text{ GeV} \leq m_{h^0} \leq 2m_Z$) and at the high mass region ($m_{h^0} \geq 2m_Z$) [15]. Processes in each of these regions are

reviewed below. The possibilities to use these channels has been extensively explored by simulation [15,16]. Figure 1.7 summarizes the production cross section of the SM Higgs boson. The gluon fusion process dominates the complete possible mass range.

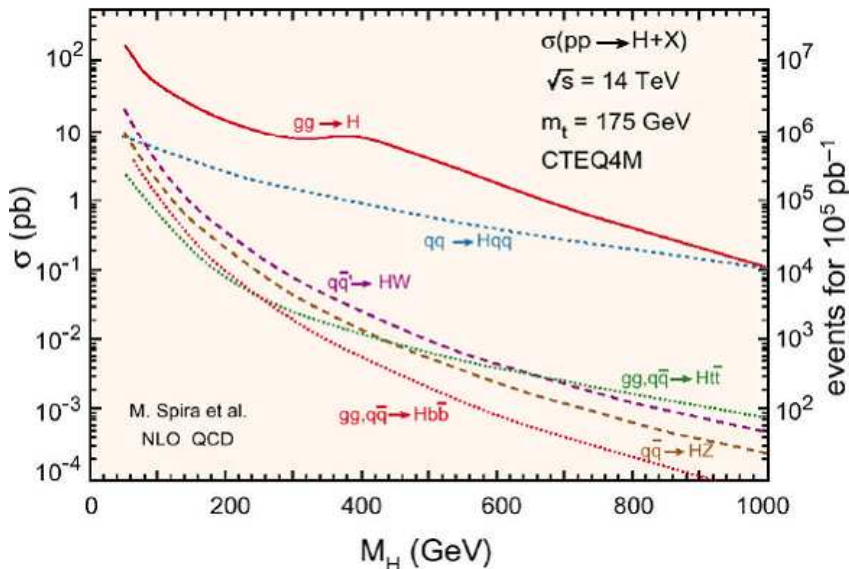


Figure 1.7: *The higgs production cross section significance at LHC below 1 TeV [16].*

Figure 1.8 shows the Higgs branching ratios as a function of the Higgs mass. At low mass region, the dominant decay mode is to $b\bar{b}$. Above the weak gauge bosons threshold, the dominant decay is to W^+W^- .

At Low Mass Region

The two modes of decay where analysis can be done is $H \rightarrow b\bar{b}$ and $H \rightarrow \gamma\gamma$. The decay to $b\bar{b}$ has a branching ratio of $\geq 90\%$. The channel however is challenged by the QCD background [15]. The associated production of $t\bar{t}H$, WH, ZH with $H \rightarrow b\bar{b}$ and with the additional lepton from the decay of accompanying particles offer additional options that can be extracted from the background thus purifying the sample. The b tagging capabilities will be useful for this channel. The $H \rightarrow \gamma\gamma$ is more accessible in this mass region though having small branching ratios of 10^{-3} , it has a better signal to background ratio. Since decay for this channel is forbidden at tree level, it occurs through top quark or W loops. The final states has high p_T photons that reconstruct to the H mass.

Also the $H \rightarrow \tau\tau$ decay channel is quite promising. An advantage of this channel, in particular compared to the dominant $H \rightarrow b\bar{b}$ mode, is the lower background from QCD processes. The channel thus offers the best prospects for a direct measurement of the Higgs boson's couplings to fermions.

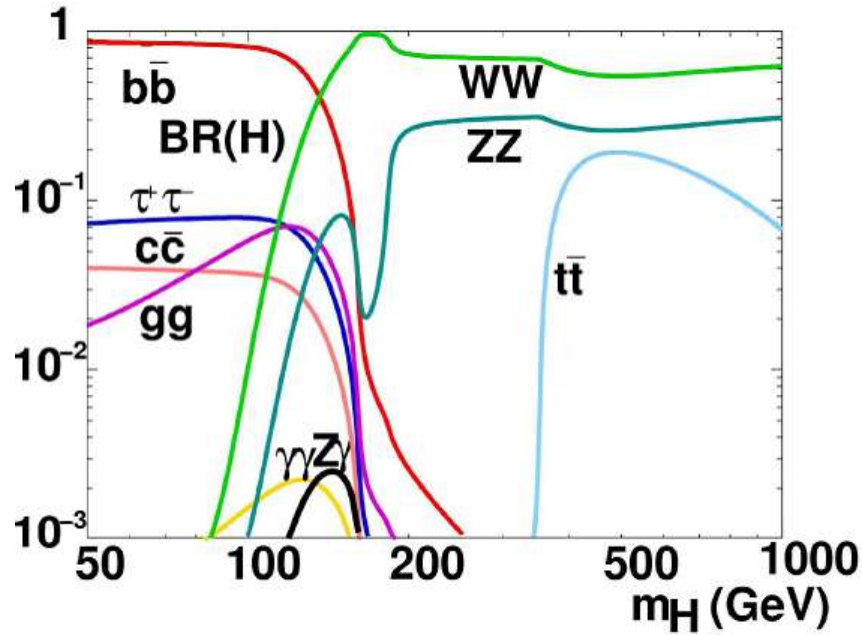


Figure 1.8: *The branching ratios for the SM higgs decay into fermions as a function of the Higgs Boson mass [15, 16].*

The Mid Mass region

In the Mid mass region the most promising channels are the those with the leptons as the final states whereby triggering by lepton is made possible. These are the $H \rightarrow WW^* \rightarrow l\nu l\nu$ and $H \rightarrow ZZ^* \rightarrow 4l$.

The High Mass Region

This region has a channel offering best H discovery opportunity. $H \rightarrow ZZ \rightarrow 4l$ mode has an almost no background result hence known as the goldplated channel. For $m_H \geq 500$ GeV, there exists also modes such as $H \rightarrow ZZ \rightarrow ll\nu\nu$ and $H \rightarrow WW \rightarrow l\nu jj$ which have larger branching ratios that can compensate for the decrease of the production cross-section of other channels [15].

Chapter 2

The LHC and the ATLAS Detector

Introduction

To achieve the physics goals discussed in Chapter 1, the Large Hadron Collider (LHC) is to provide proton to proton collisions at 14 TeV centre of mass energy thus physicists can access the TeV scale for investigations. This machine utilizes the tunnel of the former LEP^a. However additional facilities unique to the LHC have been put in place. As already mentioned there are four large experiments at the LHC classified as:

1. The general purpose detectors(ATLAS^b and CMS^c) for across-board physics investigations.
2. An experiment to study heavy lead or gold ions collisions.(ALICE^d).
3. An experiment dedicated for B mesons physics thus investigating issues like the CP-violation(LHC-b^e).

In this Chapter, a brief introduction of the LHC machine is done and thereafter the design of the ATLAS detector is discussed in some detail.

^aLarge Electron Positron Collider that operated between 1989 and 2000

^bA Toroidal LHC Apparatus

^cCompact Muon Solenoid

^dA LHC Ion Collider Experiment

^eLHC B physics Experiment

2.1 The Large Hadron Collider

A chain of accelerators are used to reach the TeV energy scale. The protons are to be ejected attaining 50 MeV then into two Synchrotrons in series (PS^f and SPS^g) after which they attain to 450 GeV, then released into the LHC ring where they are maintained at an energy of 7 TeV. The LHC is a ring accelerator of 27 km in circumference. In Table 2.1 the LHC machine parameters are summarized. Bunches amounting to 2808, each having $\approx 10^{11}$ protons are to circulate the LHC ring at a distance of 7 m apart. A stream of the bunches form the beam. Two of these beams are accelerated in opposite direction. At the points where the detectors are constructed the beams are to cross each other into collision. An event as shown in figure 2.1 can only be “viewed” by detecting machinery. Every collision is expected to yield ≈ 25 inelastic scatterings that results to 1000 new particles.

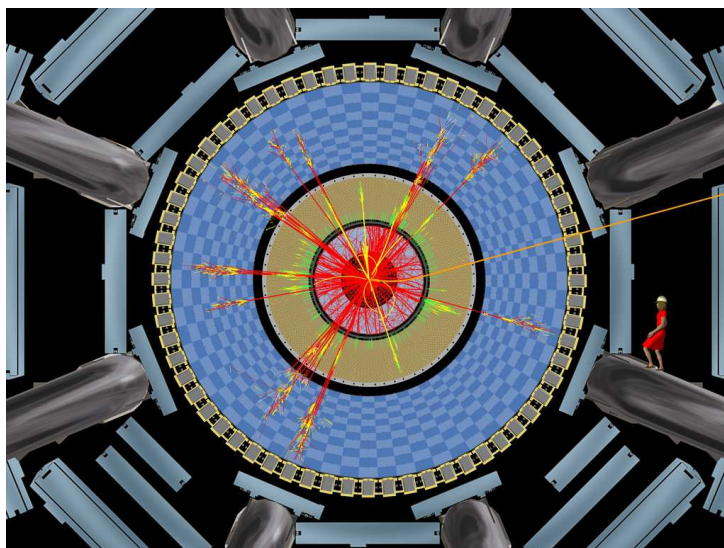


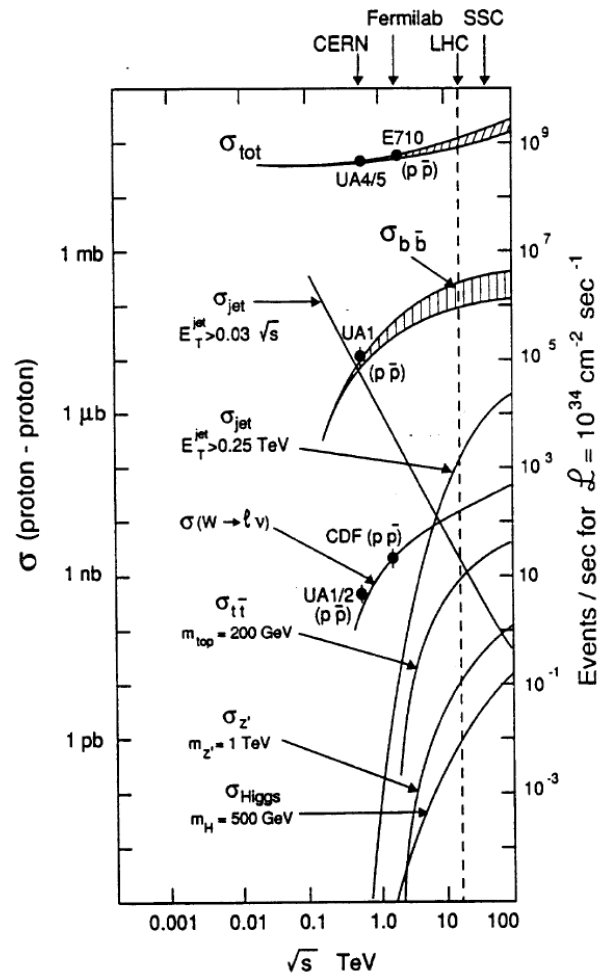
Figure 2.1: *A simulated collision event in which a mini-black-hole was produced in the collision of two protons as viewed along the beampipe. It then decayed immediately into many particles. The color differentiates the tracks. The woman is shown to set the scale of the detector [1].*

At a center of mass energy of 14 TeV physicists will have access up to the 5 TeV scale. This makes it possible to investigate physics postulated by the extension models to the Standard Model . At this energy it is possible have a wide range of measurable cross-sections. For this reason the reaction rate R must be high. This quantity depends on the cross section σ of all processes and the collider parameters such as given in Table 2.1 for the LHC. In this aspect LHC has a lead as can be seen in Figure 2.2 showing cross sections present at proton colliders and accessibility to physics events.

^fProton Synchrotron, see fig1

^gSuper Proton Synchrotron, see fig1

Property	Measure and Unit
The centre of mass energy	14 TeV
Luminosity	$10^{34} \text{ cm}^{-2} \text{ s}^{-2}$
Number of proton bunches	2808
Circumference	26658.883 m
Energy of the beam	362 MJ
Bunch to Bunch separation	25 ns (7 m)
Particles per Bunch	$\approx 10^{11}$
Rate of collision	40 MHz

Table 2.1: *The LHC machine parameters*Figure 2.2: *The cross section of processes of interest at the existing colliders [17].*

The reaction rate R is given as

$$R = \sigma \bullet B \frac{n_1 n_2 f}{A} \quad (2.1)$$

where

- n_1, n_2 is the number of particles in each of the crossing bunches.
- B is the number of bunches per beam.
- A is the cross-section of the colliding bunches.
- f is the circulation frequency.

The factor attached to the σ in Equation 2.1 is the Luminosity \mathcal{L} . At LHC luminosity $\mathcal{L} = 10^{34} \text{cm}^{-2} \text{s}^{-1}$ there is an open exploration window for physics.

To collect collision information, the momentum, the charge and the energy of the particles have to be measured. By use of analysis software, the information is used to reconstruct the events and deduce on the physics. The ATLAS detector is one of the 4π detectors designed in angle, symmetry and space (defined by the z , the Φ , the η in detector symmetry) to optimize collection of particle information.

2.2 The ATLAS Detector

The ATLAS detector is designed with the physics in chapter 1 in view. It is the largest of the 4 detectors at LHC in dimensions. It has a large collaboration of scientists. Over 2500 physicists from over 150 institutes and laboratories all over the world are putting up the 7000 tonnes machine, 22 m in diameter and 44 m in length.

As Figure 2.3 illustrates, the ATLAS experiment is composed of the **muon spectrometer** the *blue* outermost part, the **Tile calorimeter** *grey*, the **Liquid Argon calorimeter** *orange*, the inner detector (ID) in which the **Transition Radiation Tracker** (TRT) *dark – grey*, the **Silicon Tracker** (SCT) *blue – grey* and at the innermost part of the ID is the **Pixel detector** *yellow* colored small strip. The ID is enclosed in a solenoidal magnetic field of 2 T in strength and the muon system is placed within a toroidal magnetic field of 0.5 T.

The collision point is the center of the ATLAS detector as it is built symmetrically in reference to that point. The beam axis is the z – *axis*, the azimuthal angle Φ and the η describe the partial region. The η is referred to as the pseudo-rapidity and is related to polar angle θ by:

$$\eta = -\ln \left(\tan \left(\frac{\theta}{2} \right) \right) \quad (2.2)$$

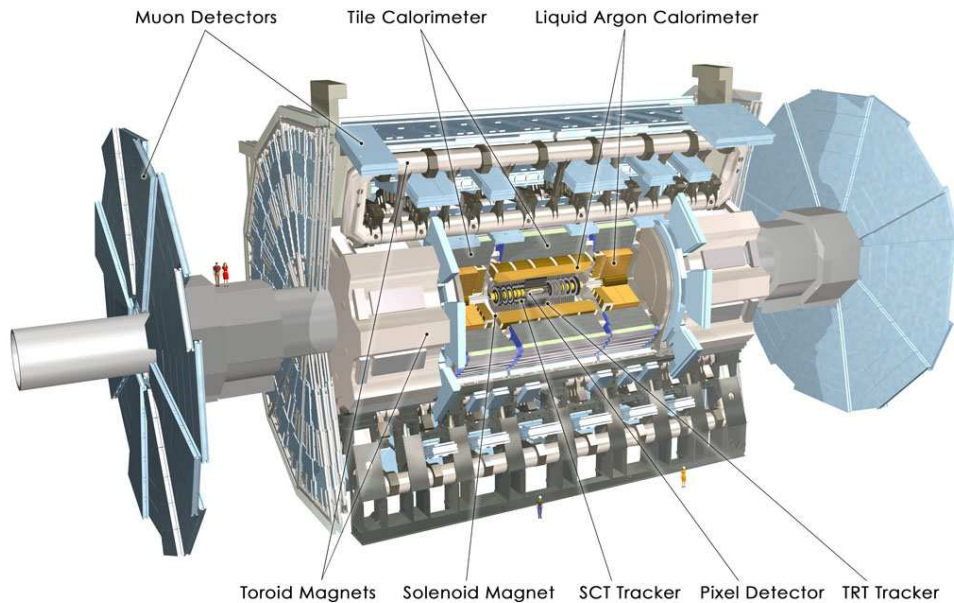


Figure 2.3: *The schematic of the ATLAS experiment [1].*

In the next sections a brief summary of the technical details and design of the ATLAS sub detectors is discussed beginning with the outermost part, the muon spectrometer, to the innermost part, the Pixel detector, the latter which this thesis is limited to. The Pixel Detector finer details will be again discussed in Chapter 3. The complete details are from the ATLAS Technical Design Report [18]

2.2.1 The Muon Spectrometer

The Muon spectrometer is designed to measure the track and the momentum of the muons. The spectrometer is composed of the monitored drift tubes (MDT), the cathode strip chambers (CSC), the resistive plate chambers (RPC), and the thin gap chambers (TGC). These parts are designed such that they can register muon particle hit information to the nearest $z=70 \mu\text{m}$ and $\Phi = (0.1-1) \text{ mrad}$. The MDT system is dedicated to precision measurements.

They are made of aluminum tubes, 70 to 630 cm long which are 30mm in diameter. A tungsten wire is encapsulated at the centre. They are filled with a mixture of argon methane and nitrogen at 3 bar and arranged in multi layers of 3 to 4 tubes. The signal is read out at the end of the tubes giving time of flight information. The MDT-chambers are arranged into 3 barrel layers of 5m by 7.5m and 10m in radius. In the forward and backward region there are 2 disks of MDT chambers on each side oriented parallel to the toroidal magnetic field optimizing the muon momentum measurements. The resolution for momentum measurements is 2% for $p_T < 100 \text{ GeV}$ and $< 8\%$ for $100 \text{ GeV} < p_T < 1000 \text{ GeV}$.

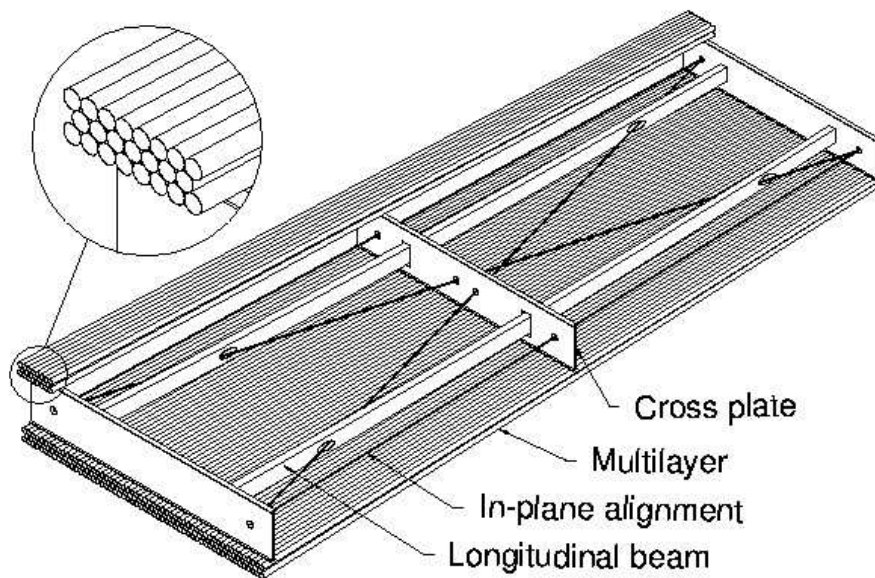


Figure 2.4: A schematic of the monitored drift tubes.

The cathode strip chambers are positioned at the forward region near to the beam pipe where the voluminous MDT cannot be used. They collect signal on strip segmented cathodes.

For the ATLAS physics program, triggering by leptons is foreseen to be a main aspect in establishing the region of interest. Thus the RPC's and the TGC's parts of the muon system are foreseen for this. The RPCs are built on top of the MDT's in the barrel region, and are designed for 2-d track points measurement while the TGC are in the forward region. Both have a very short response time generating trigger information.

2.2.2 The Calorimeter

Two types of calorimeters are utilized: The Hadronic calorimeter for measuring the energy of hadrons also gives the spartial information of the single particles and jets. The Electromagnetic calorimeter (EM) measures the energy of electrons and photons and a fraction of the hadronic jets energy. The two calorimeters are used to define the Region of Interest (RoIs). All ATLAS calorimeters are of sampling type. They combine an active medium and a passive absorption material. While there are differences in geometry and the absorber materials, the active material is liquid argon (LAr) apart from the tile calorimeter. It is preferred in that it possesses the property of intrinsic radiation hardness. The tile calorimeter in the barrel section utilizes scintillators as the active material.

The whole calorimeter system is located inside the muon spectrometer in a 11.46 m long support cylinder of diameter 8.5 m. The LAr calorimeter is surrounded by a large scintillating tile calorimeter. The barrel cryostat that is around the inner detector cavity

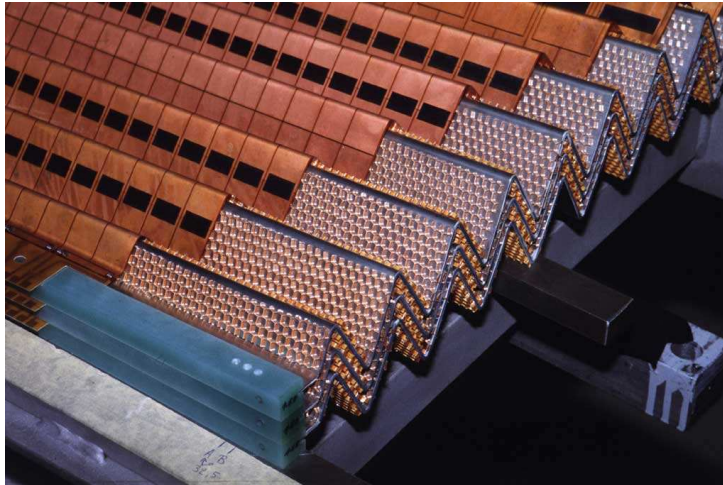


Figure 2.5: *The electromagnetic calorimeter: made of accordion shaped copper sheets and filled with liquid argon in between spaces.*

encloses the coil of the ID solenoid in its innermost radius. This is followed by the LAr calorimeter pre-sampling layer and by the EM calorimeter. Each end cap consists of an EM LAr calorimeter, a hadronic end-cap LAr and a forward LAr calorimeter.

The Electromagnetic Calorimeter

For the electromagnetic calorimeter, lead is used as the absorber medium. Lead is made into sheets, shaped like an accordion and filled with liquid argon between spaces as shown in Figure 2.5. It gives spatial information of the particle hits. The Electromagnetic calorimeter has three longitudinal samplings and a transverse segmentation of about 0.025×0.025 in $\Delta\eta \times \Delta\Phi$ covering most pseudo rapidity. It is to measure 50 MeV photons with a resolution less than 1.6% and electrons of 20 GeV with resolution less than 6% of the total energies.

The Hadronic Calorimeter

The hadronic calorimeter is located at the barrel section (tile calorimeter) and the end caps (liquid argon calorimeter). The tile calorimeter has plastic scintillators as the active material and steel as the absorber material. The liquid argon endcaps use tungsten and copper as absorber material. The scintillators of the tile calorimeter are read out by wavelength shifting fibres in three longitudinal samplings having transverse granularity of $\Delta\eta \times \Delta\Phi=0.1 \times 0.1$, covering $\eta=1.6$ in pseudo rapidity. The end cap complements the region $\eta=1.6$ to 4.9. This region is divided into a one region covering $1.6 < \eta < 3.2$ which has copper plates as absorber and $3.2 < \eta < 4.9$ with copper and tungsten as absorbers. The latter part provides both electromagnetic and hadronic calorimeters. The energy resolution is $< 10\%$.

2.2.3 The Inner Detector

The inner detector includes the Transition Radiation Tracker (TRT), the SemiConductor Tracker (SCT) and the Pixel detector. The three form the tracking system designed to enable precise information on the momentum and the charge of a transversing particle to be obtained. The system is hence immersed in a 2T magnetic field. The momentum parameter is also deduced from the information obtained from charged particle properties in the magnetic field. The spatial information collected from the tracker will enable precise reconstruction of the primary vertex, the impact parameter and the secondary vertexes. This innermost system will experience severe radiation environment due to its proximity to the interaction point thus radiation hardness was an important consideration in its design and implementation.

The Transition Radiation Tracker

This forms the outermost part of the tracker providing ≈ 30 space points for tracking and electron identification. The TRT is made from polyamid straws coated with aluminum, 4 mm in diameter and 1.4 m length. They are filled with a gas mixture of 70% Xenon, 20% CF₄ and 10% CO₂. Along the axis there is a 30 μm thick tungsten-rhenium wire.

There are about 3.7×10^5 TRT channels (straws) in total with 5.0×10^4 in the barrels and 3.2×10^5 in the disks -18 disks on each side. In the barrel between the tubes is a radiator, made from polypropylene-polyethylene fibres, and foils of polypropylene - polyethylene at the forward region thus alternating the dielectric constant in the material. A charged particle traversing this material with a relativistic velocity will emit transition radiation given that the energy of the radiated photons is proportional to $\beta = \frac{v}{c}$. It means electrons and positrons can be identified since they emit significant transition radiation at very high velocities v . The spatial resolution provided by the TRT is 170 μm in z and $r-\phi$. Tracking can be done for transverse momentum greater than 0.5 GeV and within $\eta < 2.5$.

The Semi-Conductor Tracker

The SCT is located inside the TRT. It is made of silicon strip detectors. The aim is to provide more than 3 space points per charged particle. It is in 4 layers, at the barrel region, and at each end it has nine disks all assembled with silicon strip detector modules. The modules are composed of four silicon strip detectors mounted in pairs on both sides of a carrier structure. The mounting is done with tilt of 40 mrad in between in order to resolve hit ambiguities. The silicon sensors are 300 μm in thickness and have an active area of $6 \times 6 \text{ cm}^2$. An SCT module has two sensors mounted on, thus the module has 768 silicon strips each 12 cm long with a pitch of 80 μm between them. The SCT will provide 6.2×10^6 million channels for read out and can do tracking within $\eta < 2.5$. The SCT Barrel has 500 μm effective z resolution and 23 μm $r-\Phi$ resolution.

The Pixel Detector

The Pixel Detector is in the innermost part of the tracking system. This will be discussed in chapter 3, being the key area within which this work is based.

2.2.4 The ATLAS Trigger System

At the designed luminosity of $10^{34} \text{cm}^{-2} \text{s}^{-1}$, an average of 25 proton to proton interactions will take place in each of the bunch crossings. Thus there is need to have an efficient selecting system to reduce the amount of data by selecting the relevant physics events from the background of soft interactions. A multilevel system has been developed [19]. Shown in Figure 2.6 is a schematic illustrating the selection process.

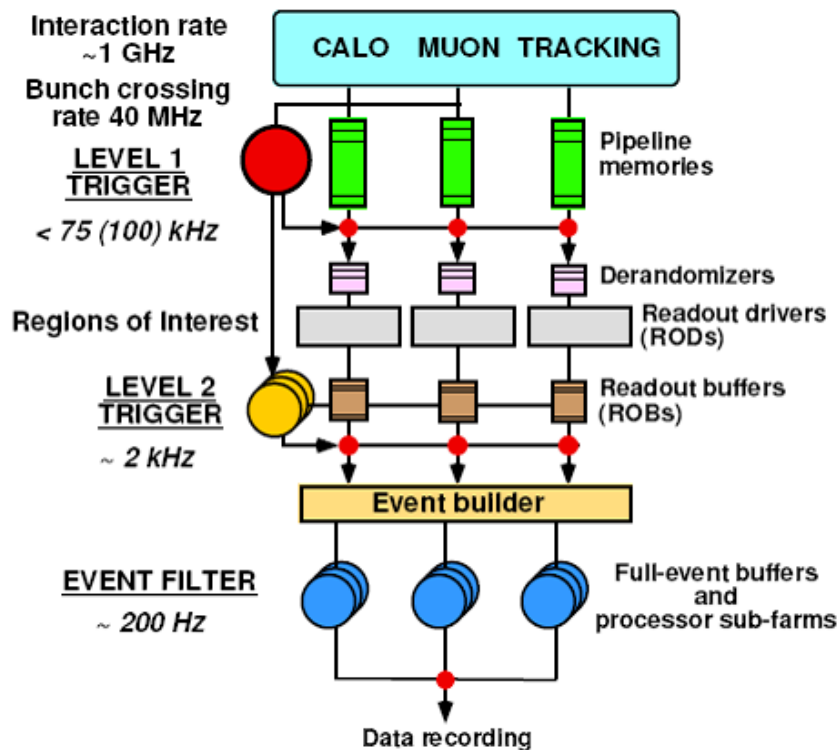


Figure 2.6: *The ATLAS Trigger scheme [19].*

The system reduces the rate of events from 40 MHz , which is the interaction rate, to about 200 Hz (1.6 MBytes) per second the rate at which events are to be written to a mass storage. The trigger is separated in three levels: Level 1 (LVL1), Level-2 (LVL2) and the Event Filter (EF). The LVL2 and EF make up the High Level Trigger (HLT).

The Level 1 Trigger

LVL1 is a hardware based system that receives signals from the calorimeter and muon sub-detectors. It reduces the events rate to 75 KHz within a latency of $2.5 \mu\text{s}$ time at which all the data from all detectors is stored in pipelined memories. The LVL1 accepted events are transferred to the readout buffers (ROB) where the data is stored awaiting the LVL2 decision.

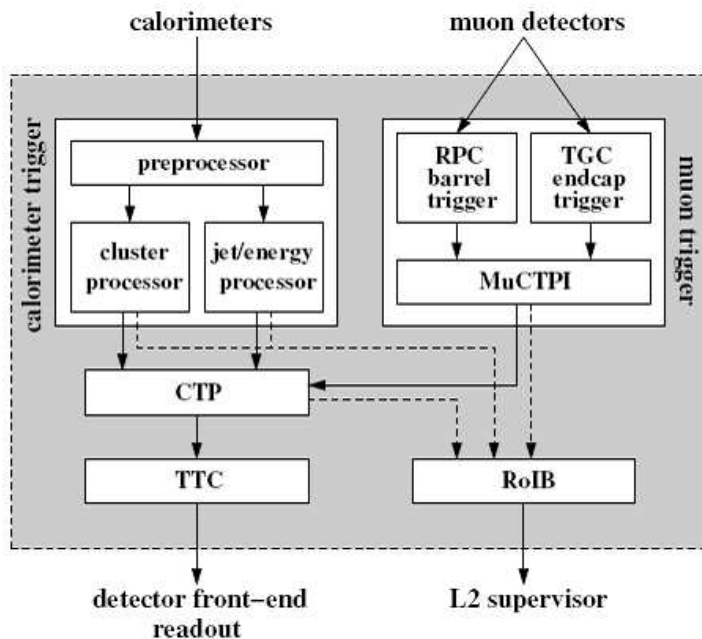


Figure 2.7: An overview of the LVL1 trigger system [19].

In a LVL1 trigger process information from the calorimeter and muon sub-detectors is combined in a Central Trigger Processor (CTP). This information is composed of the multiplicity of objects passing programmable transverse energy thresholds. In addition the calorimeter provides the global energy sum to measure the total and missing transverse energy in an event. These sums are discriminated against eight thresholds for missing transverse energy and 4 for total transverse energy. The multiplicity of each is sent to the CTP. Similarly the muon trigger derives the multiplicity count from RPC's and TGC's for the muon candidates passing 6 programmable thresholds and then sent to the CTP. A decision is made and it is sent via the Timing Trigger and Control (TTC) system to the sub-detector Readout devices (ROD). The CTP also, sends information to the Region of Interest Builder (RoIB) which compiles a list of Regions of Interest (RoI) from the event for the LVL2 trigger. This is sent to the L2 Supervisor. The type, position and threshold information constitutes the "regions of interest" (RoIs).

The High Level Trigger

The LVL2 trigger and the Event Filter (EF) composes the High-Level Trigger (HLT). An overview of the HLT is shown in Figure 2.8. The process of HLT is as follows: The L2 (denoted as LVL2 in Figure 2.8) supervisor sends the LVL1 result containing the spatial information of the objects identified by LVL1 (the “region of interest information”) to L2 Processing Unit. The Unit performs the LVL2 selection for the event by retrieving the data in RoIs from the Read out System ROS. If a positive decision is made, then the result is sent to the Event Builder which assembles the full event. The complete event is then sent to the Event Filter IO then to one of the Event Handlers which performs the event selection (EF) that are written to a mass storage [19].

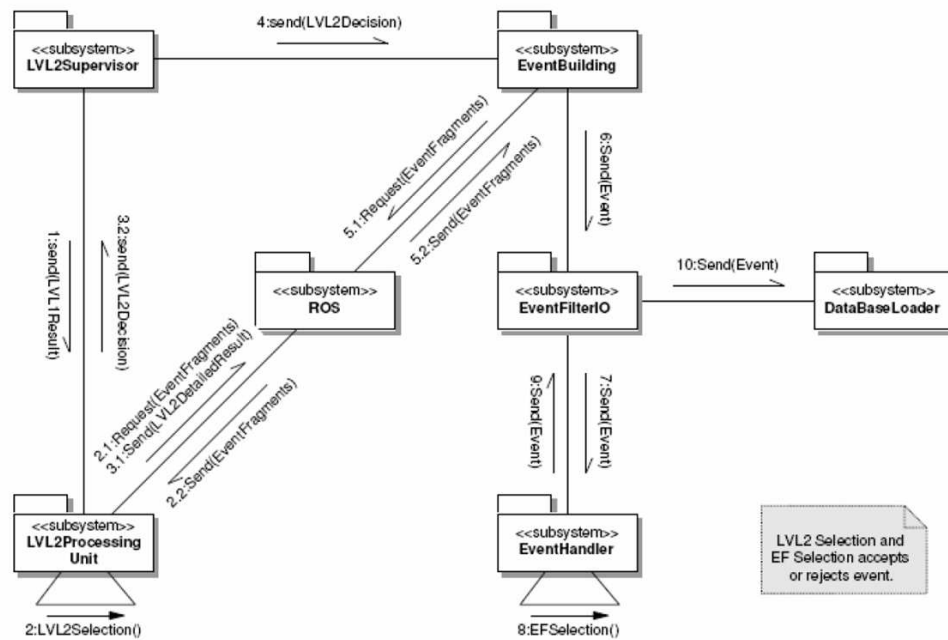


Figure 2.8: *The High Level Trigger overview [19].*

Chapter 3

The ATLAS Pixel Detector

Introduction

This chapter deals with the ATLAS Pixel detector, the innermost part of the tracking system, with some detail. The general layout of the detector and the specific parts are discussed. Figure 3.1 gives a complete layout of the detector showing the three barrel layers and 2×3 disks in the forward side. The innermost layer, close to the beam pipe has 5.0 cm radius and is referred to as the B-layer which is vital for good vertexing [18]. The layer next is called Layer-1, 8 cm in radius and the outermost layer is Layer-2, 12 cm in radius.

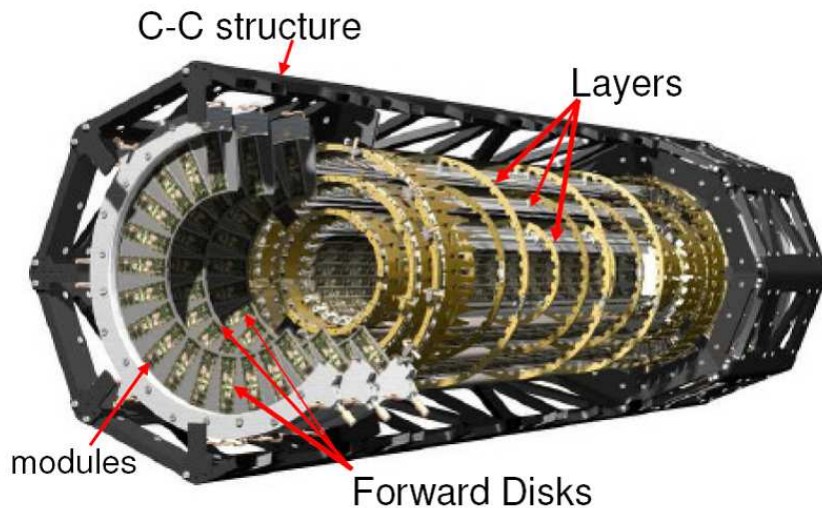


Figure 3.1: *The Pixel detector layout.*

The Disks, labeled as Disk 1, Disk 2 and Disk 3 are positioned at ± 49.5 cm, ± 58.0 cm and ± 65.0 cm consecutively in z . The geometrical designing of the layers and the disks is such that it will record 3 space point information for every passing particle within pseudo rapidity of 2.5. The design provides spatial informations close to the interaction point. The spatial resolution is $< 15 \mu\text{m}$ in $r\Phi$ and $< 120 \mu\text{m}$ in z . Precise reconstruction of the secondary vertex is therefore possible.

The supporting structure is Carbon-Carbon (C-C) and has commendable properties of stiffness for support and thermal management and has low mass. The pixel detector front end electronics mounted on the layers and the disks yield to 80 million channels.

3.1 Electronics of the Pixel Detector: The Module

In the design of the pixel detector, the guiding issues were that, the detector, being the innermost part of the tracking system had to provide good spacial resolution, high occupancy and most of all be radiation hard. Thus all the on-detector electronics had to be designed with radiation hardness technology, the deep $0.25 \mu\text{m}$ submicron technology by employing enclosed layout transistors and guard rings and this has proven to be radiation hard [20, 21]. Radiation effects on the silicon sensors will be counter-effected by using high voltage. In addition, the sensors layout is such that they have low field gradients inside and are oxygen enriched to trap defects [22].

Shown in Figure 3.2 is the basic building electronic component, the Pixel module.

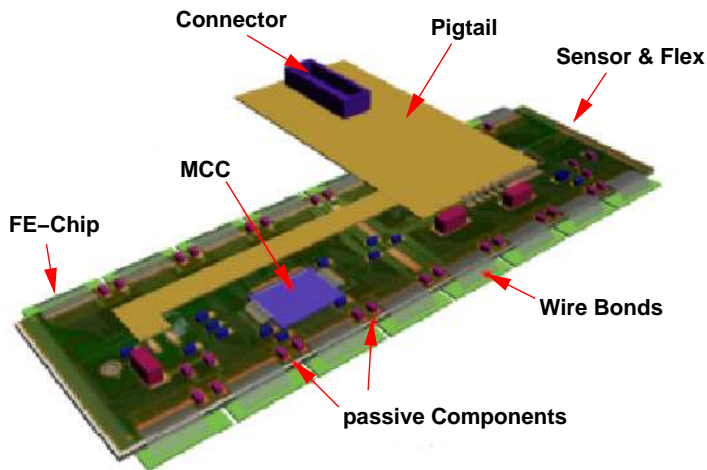


Figure 3.2: *The schematic of the Pixel module.*

It is composed of a silicon sensors, 16 Front-end chips (FE) for read out and the controlling and interfacing logic, the Module Controller Chip (MCC). The silicon sensors have a size of $63 \times 18.6 \times 0.25 \text{ mm}^3$. This design provides the 2 dimensional spatial information for each traversing particle. The sensors are divided into 46080 pixel cells. Each of the FEs is divided into 2880 readout pixel cells arranged in 18 columns and 160 rows. An FE has a size of $7.2 \times 10.8 \text{ mm}^3$. Each silicon sensor pixel is “bump bonded” to a reading out pixel cell where the signals from the sensors are amplified and digitized. An MCC controls 16 FEs. The connection between the MCC and the FE is by $25 \mu\text{m}$ thick wire bonds and the “flex”, a flexible caption foil.

The modules are then assembled into staves and sectors. A stave is a carbon-carbon support structure 83.2 cm long and 1.8 cm wide [23] on which modules are mounted. Each stave supports 13 modules symmetrically in 1.1° tilt and with an overlap in the z direction for a complete cover. The staves are then paired into bi-staves (see Figure 3.3(a)), which are then loaded into half shells (half a single layer) as shown in Figure 3.3(b). Two half shells form a complete layer.

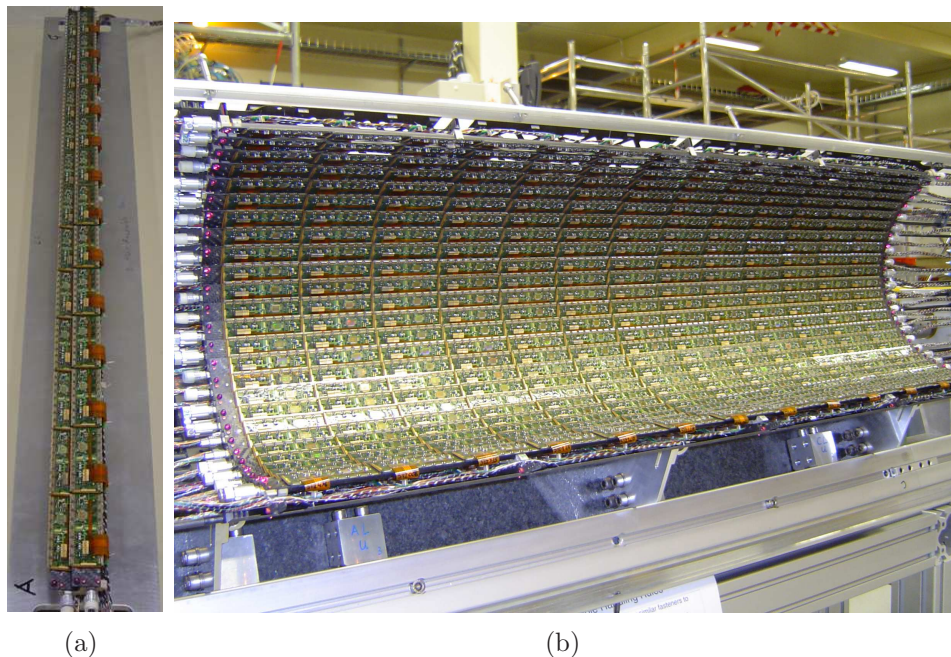


Figure 3.3: A bistave is shown in (a) on a support test structure before they are build onto the half shell. Figure (b) shows a completed half shell for layer 2 of the Pixel detector on a support structure. The half shell has 26 staves mounted [24].

A sector shown in Figure 3.4(a) is the basic building section for the disks. Each disk is made of 8 sectors. Three disks make up the end-cap shown in 3.4(b).

In Table 3.1 the geometrical values of the Pixel detector are summarized and the distribution of the module mounting is indicated. The whole detector is to use 1744 modules. This provides an active area of 1.53 m^2 and the 80 million channels to readout.

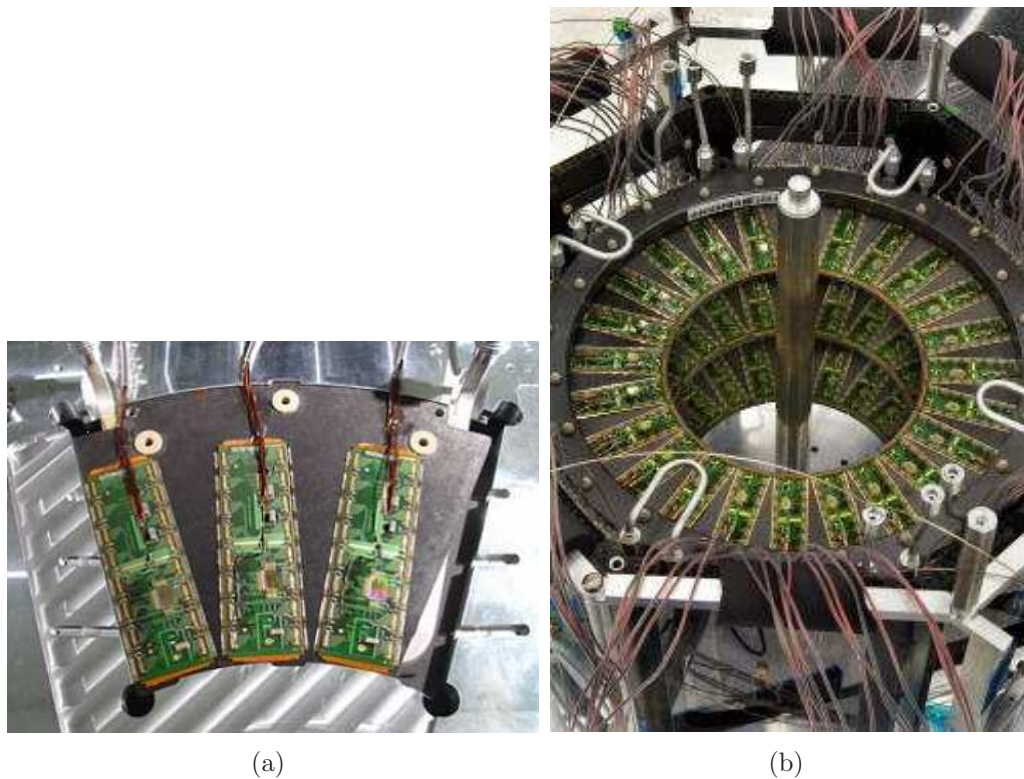


Figure 3.4: *Figure (a) shows one side of a sector with 3 modules. The back-side has 3 more modules arranged for proper coverage. In Figure (b) a completed end-cap in the testing structure is shown. The three disks can be seen [24].*

PART	Radius	Staves	No. of	Active area	Channels
PART	cm		Modules	m²	
BLayer	5.05	22	286	0.28	$1.3 \cdot 10^7$
Layer 1	8.85	38	494	0.48	$2.2 \cdot 10^7$
Layer 2	12.25	52	676	0.65	$3.1 \cdot 10^7$
Sub Total		112	1456	1.41	$6.7 \cdot 10^7$
	Position cm	Sectors			
Disk 1	± 49.5	$3 \times (8/8)$	$3 \times (48/48)$	3×0.4	$3 \times 4.4 \cdot 10^6$
Disk 2	± 58.0				
Disk 3	± 65.0				
Total			1744	1.53	$8.03 \cdot 10^7$

Table 3.1: *A table showing the geometrical positions and the distribution of the mounted modules in the Layers and Disks. There are 80 million channels in total.*

Discussed next is the technology implemented for the sensors, the front end chips and the MCC. The specific properties are briefly outlined.

3.1.1 The Sensors

The sensors are made of depleted silicon pn-junction. Ionizing particles interact producing electron-hole pairs in the depleted n-type silicon resulting into pulses that are processed by the FE. The sensor implemented for use in the Pixel detector has special design and enhancement features ensuring optimal operation in the radiation severe environment. They have utilized the property of the pn-junction to type invert under irradiation [25]. In addition the silicon has been enriched with oxygen which has been shown to withstand radiation better than normal silicon [26].

3.1.2 Radiation Hardness Property by Type Inversion

For type inversion, the n-type Silicon bulk at room temperature, converts at a fluence of $\approx 10^{13}$ n_{eq}/cm^2 to a p-type. This aspect is implemented by having an n^+ on n type. The concentration of effective doping of the sensor silicon bulk changes with increased radiation. This change of effective doping concentration means the depletion voltage needed for operation changes. While in an n-type bulk the depletion zone grows from the back side, after the type inversion the depletion zone grows from the pixel side as illustrated in Figure 3.5. Before irradiation the full depletion is needed and this uses smaller depletion voltage. After irradiation which results to type inversion, the sensor is not depleted completely. But the pixels are isolated against each other and can operate.

The active volume increases with the depletion depth. The pixel high voltage supply is designed to reach a depletion voltage of 700 V thus offering a good range to keep the sensors operative. In the n^+ on n type, the n^+ side is at ground potential preventing sparking from the sensor bias to the FE.

3.1.3 Radiation Hardness Property by Oxygenating Silicon

By enriching silicon with a measure of oxygen [22, 27] through introducing $< 5 \times 10^{16}$ of oxygen impurity into silicon, the sensors were observed to increase in radiation hardness. Shown in Figure 3.6 is a comparison between pure silicon sensors and the oxygen enriched silicon. Oxygenated silicon clearly shows radiation hardness properties indicated by the level of depletion voltage required. The B layer which experiences high irradiation due to its proximity to the beam pipe, can therefore operate by using the enriched silicon and the type inversion property. It would have had to be replaced 2 or 3 times in 10 years if pure silicon was used. Layer 1 silicon enriched sensors can operate for 10 years without replacement.

In addition the annealing process, the healing the radiation effect by temperature, also contributes to radiation hardness in semiconductors by inducing self healing. Thus for

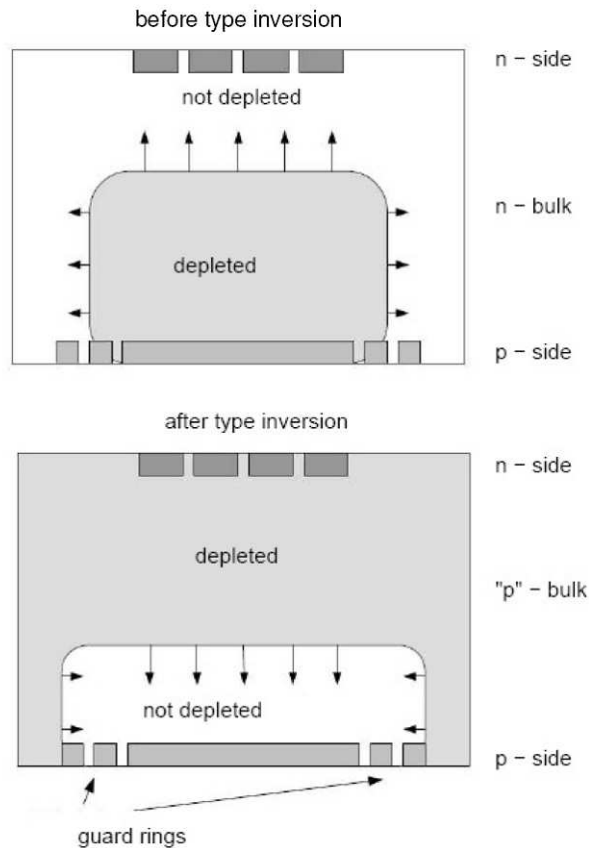


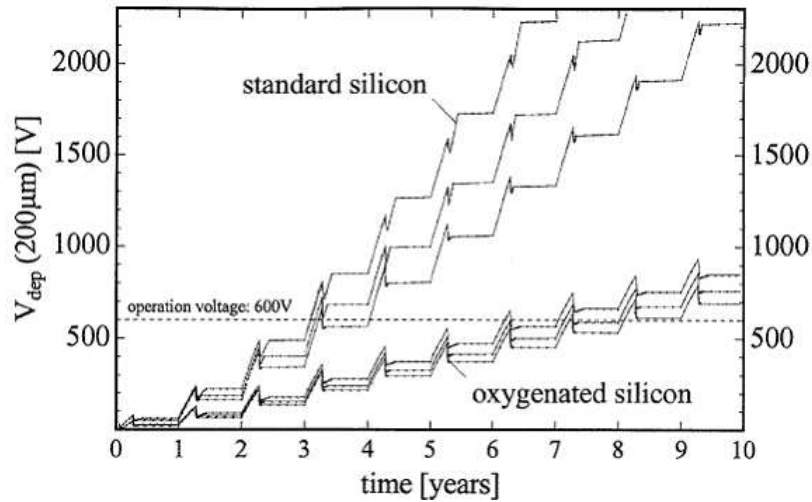
Figure 3.5: *The Silicon bulk utilized for the sensor. The property of type inversion after irradiation is utilized. Shown also are the guard rings at the backside of the bulk [28].*

the sensors, they will operate at $-10\text{ }^{\circ}\text{C}$ with a requirement that they be maintained at $20\text{ }^{\circ}\text{C}$ for 20 days during inactive periods to avoid reverse annealing effects. The mentioned temperature and time conditions have been shown to be necessary for beneficial annealing [22].

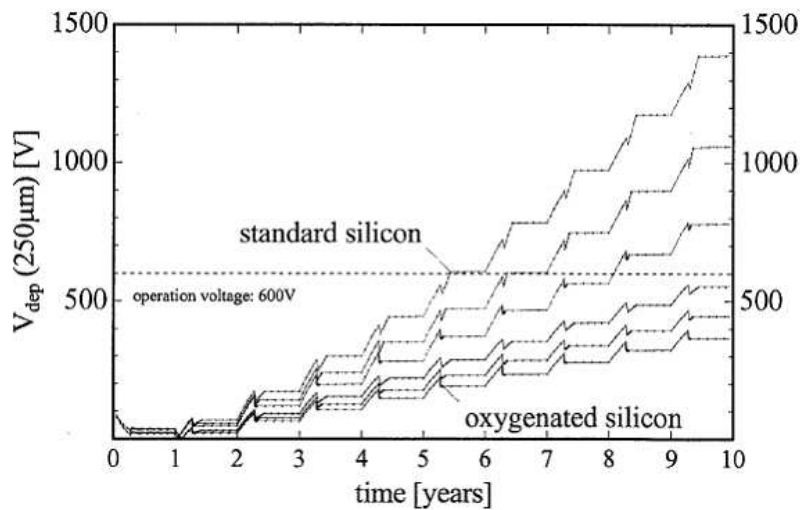
3.1.4 The Sensor Design Features

As mentioned sensor pixels are designed to giving a spatial resolution of $15\text{ }\mu\text{m}$ and $115\text{ }\mu\text{m}$ in $r\Phi$ and z direction respectively. Each of the sensor cell is connected singly to a read out electronic circuit, the pixel cell by bump bonding. There is a special design to avoid dead module region by having pixels between the long side of the chips larger by $200\text{ }\mu\text{m}$ and at the short side of the chips there are 8 uncovered pixels. These uncovered pixels are then paired to be read out by 4 readout cells.

To isolate the pixels, a p -spray technique is utilized. The surface of the sensor is sprayed with a weak p -implant. Thus the properties of the n^+ implants are not changed. The space between the sensor cells is filled with the implant yielding a $p-n$ junction that



(a) B-Layer



(b) Layer-1

Figure 3.6: A study result on the Pixel sensors under irradiation and annealing for an equivalence of 10 years. Figure (a) shows the behaviour of the silicon utilised for the B-layer and (b) shows that of Layer-1. Pure silicon sensors are compared with oxygenated silicon. The Oxygenated silicon which shows high radiation tolerance is used for the Pixel sensors. The 3 curves per silicon type show different annealing scenarios [26].

suppresses the electron travel [29]. The p -spray technique increases the device high voltage stability with irradiation. The irradiation-induced surface charge compensates the space charge of the p -spray region leading to lower electric fields after irradiation [?].

Using the p -spray technique a guard ring structure is obtained so as to isolate the electrically conductive cutting edges of the sensor from the high voltage. There are 17 p^+ rings

on a floating potential around the back-side implant (see Figure 3.5). The high potential is decreased from ring to ring and this prevents a direct contact between the sensor edge and the high voltage implant. The bias grid enables tests on the sensor to be done without the read out chips where connection is made possible via punch through. Thus the whole pixel array can be tested with only two contacts. The connection by punch through is also precautionary in case of a missing bump. The punch through method prohibits uncontrolled potential in the affected cell [26, 29].

3.1.5 The Deposition of Charge and Signal Generation

A charged particle passing through a crystalline semiconductor loses its energy to the crystal producing electron-hole pairs along its path. The energy loss per length due to ionization is given by a Bethe-Bloch formula [30] that generally relates the energy transfer of a charged particle in matter. For the silicon sensors the mean energy required to generate an electron-hole pair is 3.62 eV. For ionization to occur the energy gap in the energy band structure has to be overcome and for silicon this is 1.12 eV. However, generation of the phonon that leads to thermal energy has to be accounted for as well.

Figure 3.7 shows the behavior according to Bethe-Bloch formula, of the various high energy particles in the high energy experiment environment. The particles pass through the sensor at very high energies.

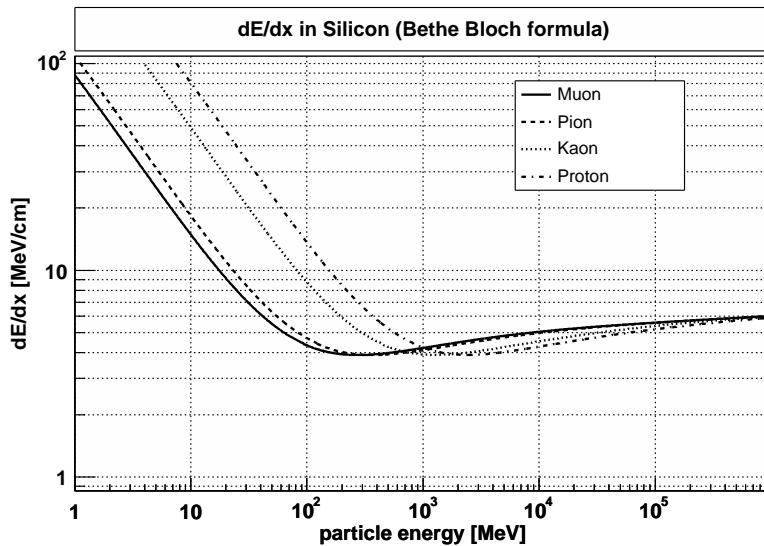


Figure 3.7: *The energy loss in silicon of the different particles according to Bethe-bloch relation. This loss depends on the energy of the particle. [31]*

At a particle velocity of $\approx 0.96 c$ a minimum in the Bethe-Bloch formula is reached and particles at this point are called the minimum ionizing particles (MIP). From the Figure shown in 3.7, the $m_\pi = 139.57$ MeV, for example, generates energy of ≈ 97.5 keV in silicon. This generates 27000 electron hole pairs for a 250 μm thick sensor. But from the Landau

distributions it follows that, for thin absorbers, the energy loss probability functions are not gaussian but have a tail to the higher energies due to possible interactions with high energy transfer [32]. Thus for the $250\ \mu\text{m}$ thick sensor ≈ 20000 electron hole pairs are produced which corresponds to 70 % of the produced total. The electrons and holes produced in the sensor are separated by applying reverse bias voltage giving rise to the signal. The readout of the signal is discussed below.

3.1.6 The Pixel Cell: Design and Operational Features

The pixel detector is designed to measure the passage of ionizing particles with 3 space points. A MIP that pass through the $250\ \mu$ thick sensor results to a charge of $20000e^-$ as indicated. If the particle interacts at 90° the deposited charge is shared by up to 4 pixels. In this case a charge of $5000e^-$ has to be recognized otherwise the hit is lost. At the pixel cell the discriminator threshold can be set. There is an association of the hit to the correct 25 ns bunch crossing. The discriminator threshold is nominally set to $4000e^-$. Particles with charge of $\approx 1500e^-$ above the threshold can be be associated correctly to the relevant bunch crossing. Hence $5500e^-$ is the minimal charge measurable to the correct triggering window. [28].

The pixel cell electronics is shown in Figure 3.8. There is an analog and a digital part. The analog part has a fast preamplifier that integrates the sensor charge into a feedback capacitor which discharges with a constant feedback current.

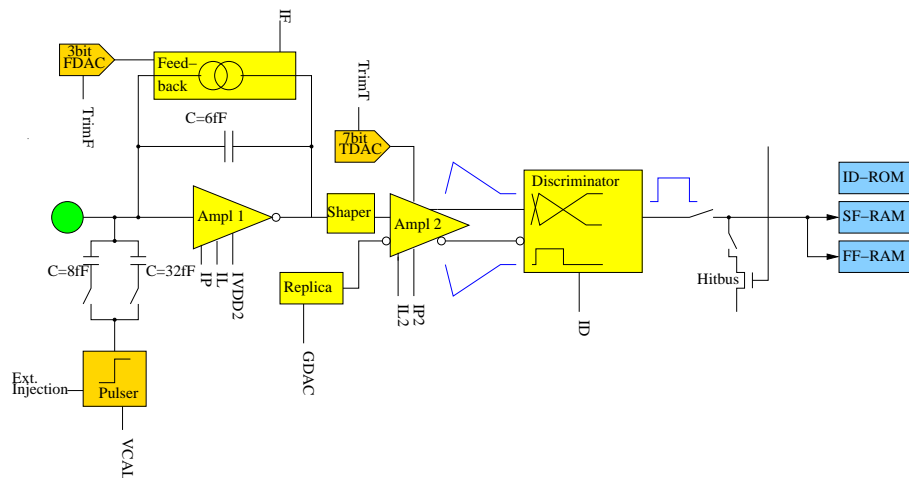


Figure 3.8: A single pixel cell: 2880 cells in 160 rows by 18 column matrix make up a single pixel cell [28].

The outgoing current signal is then amplified differentially. In the digital part a signal is generated by replica circuit that reproduces the DC potential of the first amplifier part. The discriminator that follows translates the analog pulse signal into binary.

This translation from analog to digital signal is lengthwise in steps of 25 ns. The constant discharging current signals have time above the threshold that is proportional to the

height of the signal as shown in Figure 3.9. This is proportional to the deposited charge and constitutes the Time Over Threshold (TOT). The rise time and the fall time is stored into RAM, one for each, which is then read out. The proper assignment of the this TOT information to the correct 25 ns window of the correct bunch crossing is essential for physics data taking and vast studies have been done [28] and constitutes an important aspect of detector timing.

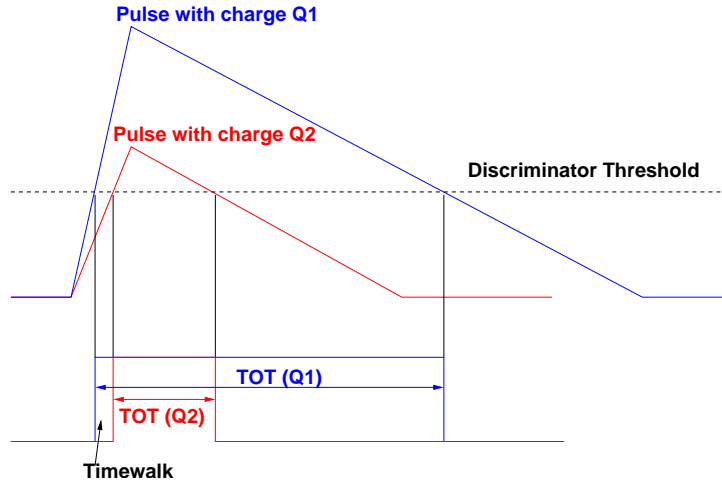


Figure 3.9: *An illustration of how hits with different deposited energy are collected in the pixel cell. The minimum charge that can be associated with the correct bunch crossing gives the in time threshold. The time of rising above the threshold is observed to depend on amplitude of the pulses (the timewalk) [28].*

The binary hit information is stored in the hit-bus. This hit-bus information which is “ORed” over each column can be used for test purposes or as a trigger signal, but it is not utilized in the physics data taking.

Several settings can be set to optimize the functionality of the FE’s. The discriminator threshold can be set globally by the FE Global DAC (GDAC) setting and locally for each pixel by an individual 7-bit-DAC, the TDAC which controls the timing of the thresholds. The TDAC adopts the threshold in a fine way to reduce the variation of the pixel individual thresholds.

The TOT characteristic can be reduced in the module by adjusting the feedback current by which the steepness of the discharging curve in each pixel is adopted by setting the FDAC’s. the DAC settings that control the feedback current. The pixel settings are stored in a 14 bit memory allocated as follows: 7 bits for the TDAC settings, 3 bits for the feed back settings, the FDAC. The remaining 4 bits are used to enable the pixel for 4 different purposes: An enable bit enabling the pixel for readout, a hitbus-bit that enables the hitbus line, the kill bit that disables the preamplifier, and a select bit that can opt for a pixel setting to test pulses. Two capacitors C_{low} and C_{high} in each pixel are used to pulse a charge, which simulates a hit registered at the sensor hence tests without the sensors are possible.

3.1.7 The Module Controller Chip: Design and Operational Features

The MCC interfaces the FE and the readout. It receives the configuration, converts it to the relevant mode, and passes it to the front end chips. It also distributes the received trigger signals to the front end chips and builds an event fragment by reading the hit data from the front end chips per event. This is in turn sent to the readout.

The MCC also generates different reset signals to synchronize with the data acquisition and to reset the front end chips in case of errors. Signals can also be sent to the MCC for calibration and tuning purposes. Figure 3.10 shows the general layout of the MCC logic.

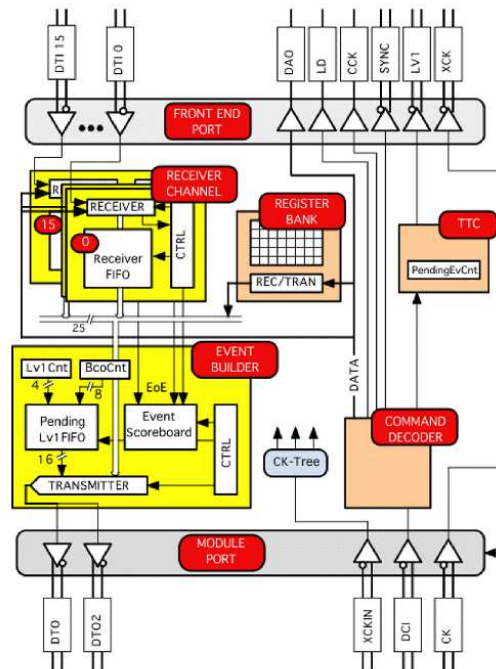


Figure 3.10: *The module controller chip logic [33].*

The module port interfaces between the MCC and the opto-board^a for data transmission. The opto-board will be discussed in Chapter 6. The front end port interfaces between the MCC and the front end chips. The module port has 3 LVDS inputs for clock and command signals input and 2 LVDS outputs for returning the data. The data outputs DTO and DTO2 can be set either in a mode to send data in 40Mb/s or 80 MBits/s on each line. The result is a total transfer bandwidth of 40 MBits/s or 80 MBits/s or 160 MBits/s. At 80 MBits/s two settings can be utilized where one sends data out with 80 Mb/s or two data out with 40 MBits/s. At 160 MBits/s two data out with 80 MBits/s are utilized.

^aThe Pixel on-detector opto electronic interface. See later Chapters.

The front end port has 7 output lines and 16 input lines. While the signals DAO, LD, and CCK are distributed over single ended signals to the front end chips, the timing signals XCK, LV1 and SYNC are distributed via multi drop differential lines to the chips. The front end chip output is connected via a differential line per chip to the MCC.

For each LV1 trigger the 16 front chips pass the hit data to the MCC. Each hit is encoded using a fixed length frame of 18 bits or 26 if the optional ToT information is selected. There are following bits: 1 headerbit to wake up the receiver, 4 bits to identify the LV1 trigger number, 8 row number and 5 column number bits. All possible errors, warnings and EoE messages from the FE's are coded in the unused 8-bit row number (row numbers from 224 to 255). A row number above 224 is always interpreted as an EoE.

Individual hits, that belong to the same event, can be separated by any number of zeroes. Once an event is finished an End-of-Event (EoE) word is sent to the MCC. This EoE word has to be sent to the MCC even if there are no hits associated with the event. One EoE word for each FE is in fact needed by the MCC in order to start the event building. The data rate on these links is relatively low, which allows automatic data recovery if a gap of more than 18(26) zeroes appear in the data stream.

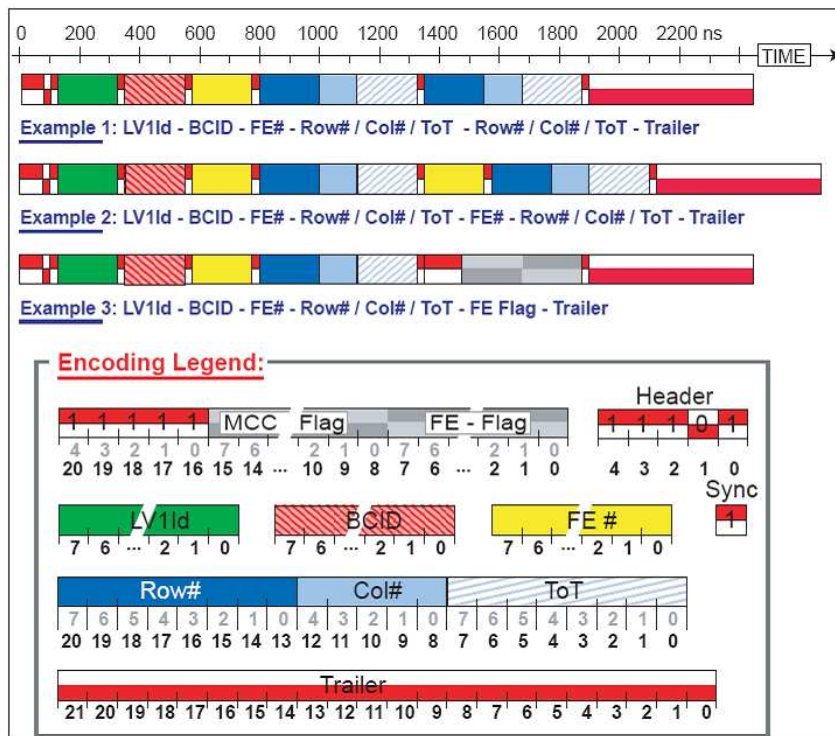


Figure 3.11: *Event Data format at the MCC output to the readout. Example 3 illustrates the case of an event with a FE error Flag [33].*

Figure 3.11 shows an example of MCC data format. The data stream generated by the MCC is organized on an event format. All information sent out by the MCC is organized in data-blocklets preceded by a header (“11101”) and followed by a trailer (“100 000 000”). This trailer is a unique pattern if the data stream is interleaved by synchronization

bits (“1”). Each event is defined by an 8 bit LV1 number, which labels the event, an 8 bit FE number followed by all hits that belong to that FE organized in an 8 bit row number, 5 bit column number and possibly by an optional 8 bit ToT. After the first non empty FE data has been transmitted a second 8 bit FE number followed by row, column, ToT is serialized. Possible error or warning flags produced by the MCC are coded in the data stream.

Thus during the module data transmission to the read out, a header is transmitted first followed by the LV1 ID and the bunch crossing ID. Following these IDs is the front end number, the column, the row, and the TOT of each hit per chip. Any error flags are attached and a trailer finalizes the read out data.

Chapter 4

The ATLAS Pixel Optolink and the Opto-Board

4.1 Introduction

In this chapter the components of the optical-link, utilized for data transmission in the ATLAS Pixel sub-detector are discussed.

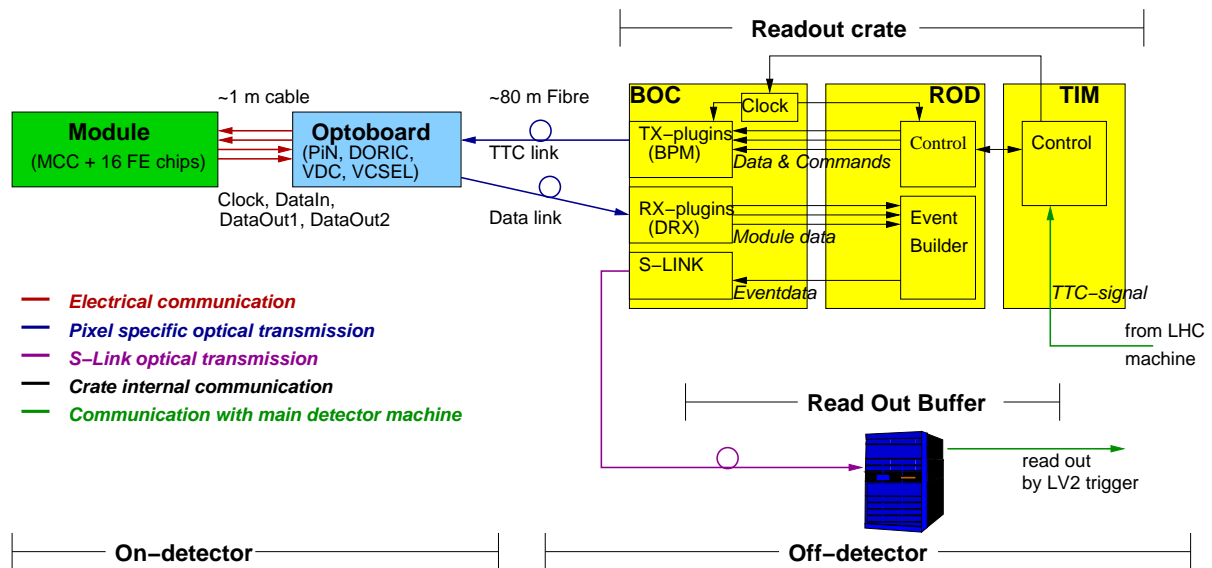


Figure 4.1: *The Pixel detector readout chain. A multiplicity of the set up is to read all detector channels using an optical link for communication to both ends [28].*

Figure 4.1 summarizes the layout of the ATLAS Pixel readout chain where the *to* and *from* the detector communication paths are shown. The detector timing, trigger, and control signals (TTC) are transmitted optically from the off-detector electronics to the on-detector electronics and module data on the return path to the off-detector electronics. There is an optoelectronic interface on each side and an 82 m optical fiber connection. The general overview of each part and their special characteristics is given in this chapter.

Optical data transfer was preferred for a number of reasons: first the requirement of non magnetic materials to avoid perturbations of the inner magnetic field, then the need of low mass hence the produced particles experience low radiation length. These are well met by using the optical link. The fibers offer a low mass path as many channels are packed into a small volume, and also decouple well the front-end and on-detector electronics. By transmitting optically, the signal quality loss is reduced. Signal quality loss is more by use of electrical transmission due to ohmic signal quality loss which is greater than optical loss.

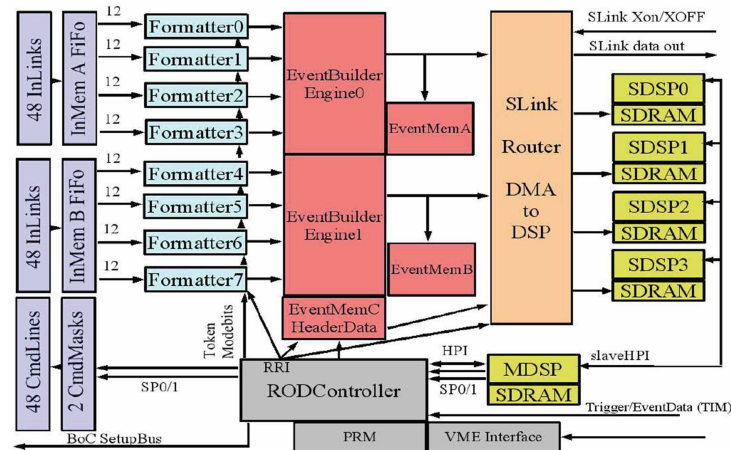
The following section is an overview discussion of the electronics making up the whole readout chain. The part of the optoelectronic transmission will be emphasized since this consists the major part of this work and the finer details of the other electronics will be referred to literature.

4.2 Overview of the Off-detector Electronics

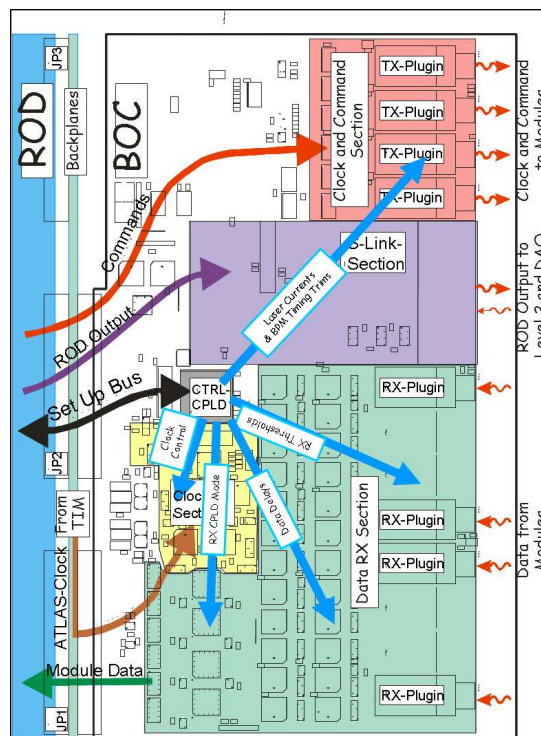
On the off detector side as shown in Figure 4.1, the Readout driver (ROD) and the Back of Crate card (BOC) constitute the main active parts of the opto-link to be placed in the counting room in nine 9U VME crates. A single BOC card serves one ROD. A total of 132 of each are needed to build the off detector part of the chain. The trigger timing and control signals from the LHC machine reach these electronics by a TTC Interface Module (TIM) and communication to the Readout Buffer (ROB) is via an S-Link interfaced optically from the BOC card. A single board computer stationed in each crate controls the ROD and the BOC card and communicates by ethernet to the computers that steer data acquisition.

At the ROD (see Figure 4.2) is where the command to the Pixel modules are generated and rebuilding of the events from the module data. The FPGAs and the DSP-chips mounted there are programmed to format the incoming data streams into events while checking for MCC error flags, FE chip error flags or detect any unphysical data. The final data format is passed on to the ROB via S-Link. The triggers coming from the ATLAS trigger processor through the TIM are received at the ROD then sent to the modules via the electrical to optical interfacing Transmission optical plugin (TX-plugin) stationed on the BOC.

The BOC is the main optoelectronic interfacing board with key functionalities of detector timing adjustment purposes. The LHC machine clock from the TIM is received at the BOC card and distributed accordingly. Coming from the ROD through the BOC card are the electrical control signals to modules. They are encoded into a Bi-Phase Mark signal



(a) A schematic overview of the Read out Driver (ROD) [34].



(b) An overview of the Back of crate Card [35].

Figure 4.2: *The ROD and BOC card overview: The two parts are connected back to back.*

(BPM) and dispatched optically to the Modules. The interfacing part between the BOC and the module will be discussed next. The masking, timing, laser current adjustment, receiving threshold adjustment, and clock synchronization for the TTC sending and module data receiving parts is done at the BOC card. It also provides the S-Link path to transferring the formatted data from the ROD to the Readout Buffer.

4.3 Overview of the On-Detector Electronics

At the on-detector, the electronics of the optical-link are mounted on the Opto-board. They provide the optical-electronic interface linkage to the module. Mounted on the opto-board is the Digital Optical Receiver Chip (DORIC) that receives electrical BPM signal through the PiN diode. For the module data transmission is the Vertical Cavity Surface Emitting Laser (VCSEL) and its driver Chip, the VCSEL Driver Chip (VDC). The opto-board will be discussed in detail in the later sections. The electronics on the module have already been discussed in detail in chapter 3. Figure 4.3 shows the communication flow at the front end electronics.

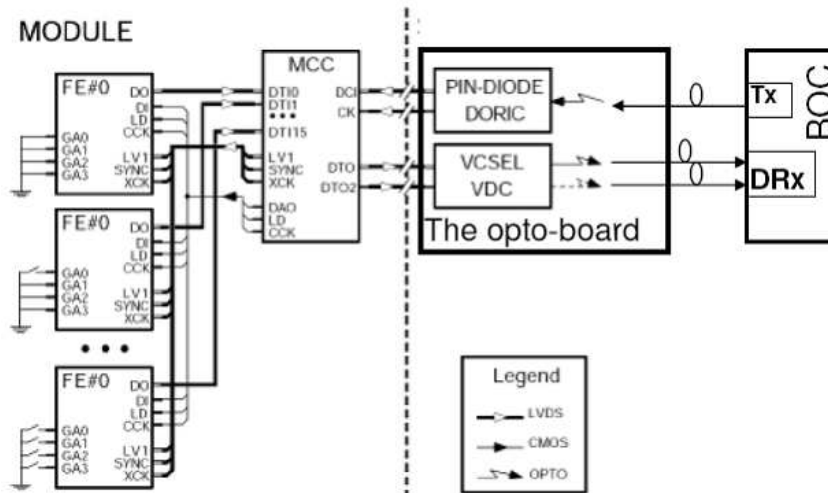


Figure 4.3: *The communication flow in the detector end electronics [28].*

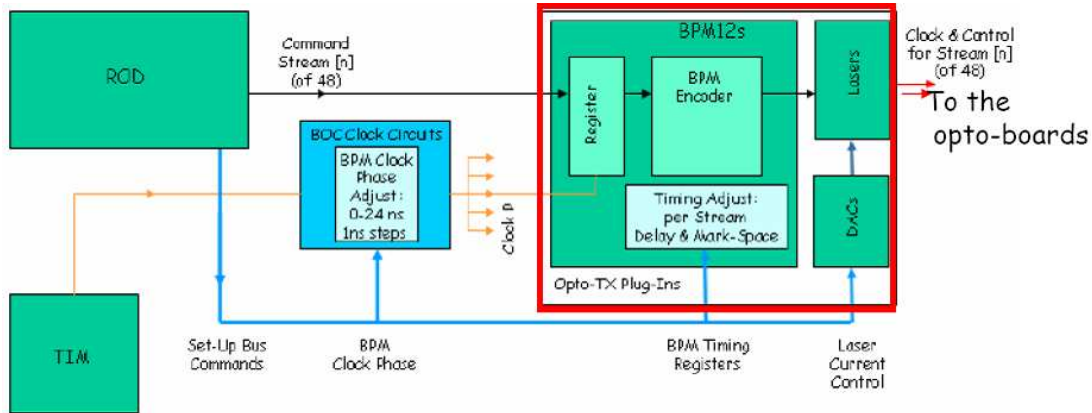
4.4 The Link Between the Off-Detector and the On-Detector

The specific parts that are dedicated to optical linking are situated on the BOC and at the opto-board. At the BOC card, there are two types of plugins mounted, that is, the TX-Plugin for transmission, and the RX-plugin, for receiving [36]. All the electronics in the specialized plug-ins are steered at the BOC card.

4.4.1 The Off-Detector TTC Transmission Part (BOC TX)

The Tx-plugin hosts the BPM^a chip and a VCSEL array having 8 channels. Each channel links to one module and settings are set separately for each channel such there is one to one communication-modularity to the modules with respect to transmission properties.

^aBi-phase mark encoding chip

(a) The TX-plugin. Size:1.5 by 3.5 cm². [28].

(b) The schematic view of the TTC sending section on the BOC [35].

Figure 4.4: The TX-plugin and the TTC sending schematic at the BOC card.

The commands received from the ROD are passed to the TX-plugin. The command and the clock signals are encoded into BPM signals and then sent to the module. Figure 4.4(b) illustrates the mentioned process while Figure 4.5 shows the BPM encoding process. To encode the 40 MHz with the command signals, transitions are sent corresponding to the clock leading edges only. Absence of data (logic 0) leads to a 20 MHz clock. Data bits are encoded as extra transitions at the clock trailing edges.

At the transmission section of the BOC the timing capabilities of delays can be set. As shown in Figure 4.4, there is a clock supplied to all module channels that can be delayed from 0 to 24ns. The clock is then passed to the BPM chip in the plugin where additional delays, fine and coarse, can be added for each module and hence possible to adapt precise timing of the module with respect to the positioning in the detector and the interacting particles to optimize data taking process [28]. The fine delay can be set between 0 to 35.56 ns in 320 ps steps on average. The coarse delay can be set between 0 to 775 ns and has a stepsize of 25 ns. Other signal properties set in the BPM include the duty cycle and an inhibit-encoding property, where no data encoded but only the clock is sent out.

The light signal amplitude of each VCSEL channel is also set at the TX-plugin. The relatedness of these functionalities has been studied in light of detector tuning process

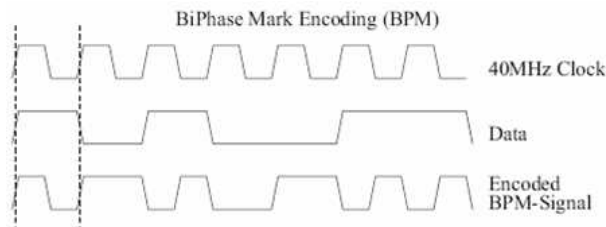


Figure 4.5: BPM encoding: Transitions are sent corresponding to the clock leading edges. Data bits are encoded as extra transitions at the clock trailing edges.

and simulated calculation has been done to determine the working space and the inter-relation of these settings, which is a part of this work, discussed in Chapter 7.

4.4.2 The Off-Detector Data Receiving Part (BOC RX)

At the receiving side of the BOC is the RX-plugin shown in Figure 4.6(a), an 8 channel device that receives the optical signals and converts to an electrical signal using a PiN diode array package [36]. The signal is amplified by the DRX^b, also mounted on the RX-plugin.

Several functionalities can be set per channel and hence it is possible to accommodate the incoming optical signal of different amplitude by setting threshold per channel. The resulting electrical differential signals at the RX-plugin are passed on to the BOC CPLDs^c chips, which perform main functions on the BOC, then to the ROD formatters as shown in Figure 4.6(b).

4.5 The Opto-Board

The optoelectronic part on-detector side is the opto-board shown in Figure 4.7. There are two types of the opto-board: The 7 links (Layer 1, 2 and disk) and the 14 links (B-layer) boards. This is differentiated by the number of the VDC^d to VCSEL^e pair mounted. The empty slots marked "X1" and "X2" are filled for the 14 links board and in addition a differently routed board is used to accommodate proper B-layer routing of the data links.

The specialized components of the opto-board are: the DORIC, the VDC, the VCSEL and the PiN diode. All are mounted on a Beryllium oxide substrate special for heat management. Each VCSEL array of 8-channels is driven by 2 VDCs, meaning a 14 links board has 4 VDC's. One VCSEL channel is not in use for the 7-links board. For a

^bData Receiving IC

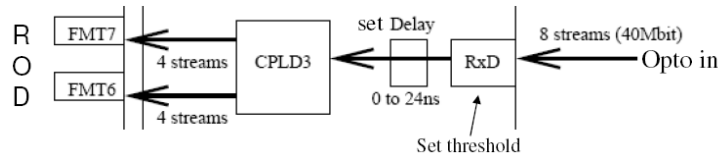
^cComplex Programmable Logic Device

^dthe chip driving the VCSEL

^eVertical Cavity Surface Emitting Laser



(a) The RX-plugin. Size:1.5 by 3.5 cm². [28].



(b) The data flow at the BOC receiving section [35].

Figure 4.6: *How a data signal from the module is processed at the BOC receiving end. An optical signal is received into the RX-PiN. A set RX-threshold blanks out the noise. The delay is applied accordingly to set the received pattern to the correct phase and the data signal is then sent to the ROD.*

14 links board, one VCSEL is fully used and the second has two unused channels. The DORIC has 4 channels that are connected to a PiN diode. The PiN diode is also an 8 channel diode array, hence two DORIC's are used. The PiN and the DORIC constitute the TTC receiving part of the opto-board while the VDC-VCSEL constitute the data sending return path.

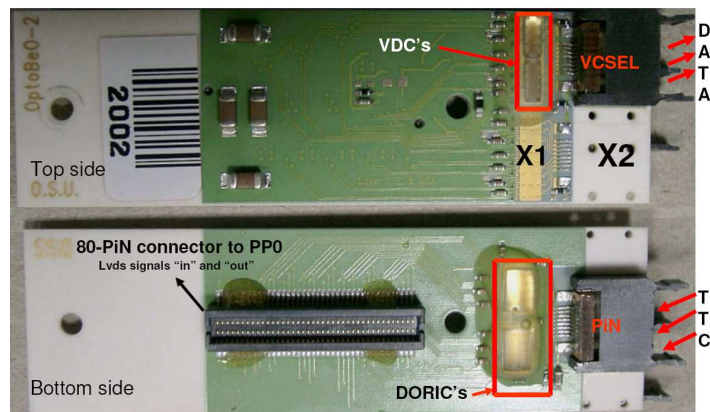


Figure 4.7: *The Opto-board: Shown is the top and the bottom side of a 7-links opto-board.*

A picture of 7 links opto-board is shown in Figure 4.7. Each of these parts will be briefly discussed as a major part of this work deals with the opto-board.

4.5.1 The PiN Diode and the VCSEL Optopacks

The PiN Diode

The PiN diode has been utilized in two places in the opto-link: At the BOC card in the RX- plugin and at the opto-board. The PiN diode basically receives an optical signal and gives out an electric current signal. The key properties of the PiN diode that give optimal operation are an optimized biasing voltage and high efficiency of optical to electrical conversion (the Responsivity (R)). A photo diode generates a current proportional to the incident optical power. To generate a current the photon energy must be at least equal to the band gap energy. Hence the limit on the wavelength λ at which a semiconductor material with band gap E_g can be used as a detector is given by:

$$\frac{\hbar}{\lambda} \geq E_g \quad (4.1)$$

where \hbar =Plancks constant λ =photo wavelength E_g =band gap energy. Applying an external voltage gives rise to a photo current I_P . The responsivity R is the ratio between I_P and the incident optical power.

$$R = \frac{I_P}{P_{in}} [A/W] \quad (4.2)$$

The PiN diodes are diodes with improved efficiency by introducing lightly doped semiconductor between P -type and N -type semiconductor. The efficiency η is given by

$$\eta = \frac{P_{abs}}{P_{in}} = 1 - e^{-\alpha L} \quad (4.3)$$

where α and L represent the absorption coefficient and the thickness of the active area respectively. P_{in} is the incoming photo wavelength while P_{abs} is the absorbed part.

These properties relate to the quality of the electrical signal in terms of signal rise and fall times and amplitude. The diode properties have been studied widely for their suitability to be used in the detector environment and have been implemented in the produced detector PiN diodes [37, 38, 39, 40, 41]. The diodes are utilized by the ATALS opto-link in the Pixel detector and the SCT. An added requirement of these diodes is that they must be radiation hard and this has also been well studied. The nominal setting bias voltage is +10 V and the responsivity is $0.59 \pm 0.05 \frac{A}{W}$ before irradiation. The responsivity drops to $0.33 \pm 0.05 \frac{A}{W}$ after irradiation affecting the signal amplitude, thus a calculation has been done (Chapter 6) verifying the sufficiency of the signal after the effects of irradiation

and transmission attenuation. The PiN diode is a detector and hence picks up charge, during operation in an irradiation environment causing pulses which may corrupt the TTC signal. For this reason the MCC is designed to protect against the effect of bit flips resulting from the single events upset by using a 5-bit long signal command for the TTC signal, specifically the LV1 [33]. For this, any single bit flip in the trigger nominal bit pattern results in a trigger. Meaning a single bit flip does not change the trigger message.

The VCSEL

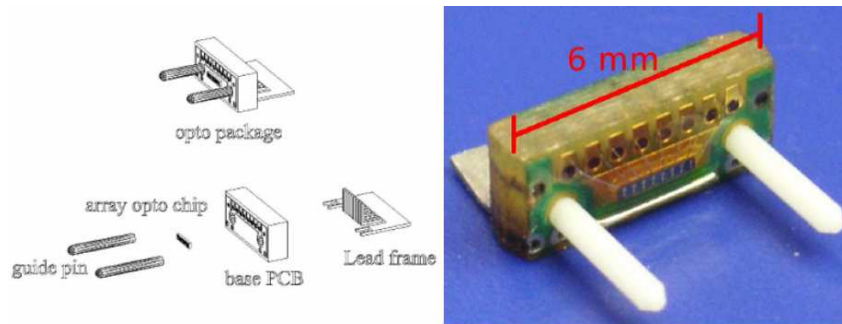


Figure 4.8: *On the left is a schematic showing the various parts that make up an optopack. The complete VCSEL optopack is shown on the right [40].*

The VCSEL lases out light power on supplying current. The key and important features to observe in a VCSEL is the lasing threshold, the minimum current at which light emission begins and the output power amplitude, the level of light emitted which must show consistency with time and temperature. For the detector use, radiation hardness is a crucial requirement. The VCSELs that have been implemented in the detector have got a current threshold of ≈ 2 mA and can output power up to ≈ 6 mW. They are designed to emit a wavelength, λ , of 850 nm [41, 42]. Irradiation studies have shown that they can lose up to 24% of power on average after an irradiation with $2.3 \times 10^{15} \frac{p}{cm^2}$ of 24 GeV protons. A worse case loss can be a loss up to 40% [39, 40]. A further discussion of the VCSEL is done in the study chapter 5 and 6.

4.5.2 The ASICs: DORIC and the VDC

The DORIC

The DORIC is a four channel chip designed to receive the BPM encoded TTC signal and decode into command and 40 MHz clock signals. The chip is powered with 2.5 V and draws a current of 80 ± 2 mA [21]. A PiN current signal (I_{PiN}) received must be above the working lower threshold of the circuit $I_{PiN} \approx 40 \mu A$. The DORIC works at the highest PiN currents that the TTC link off-detector VCSELs can deliver (≈ 1 mA). Laboratory tests

have shown the DORIC can work at 4 mA amplitude PiN currents [38]. As illustrated in Figure 4.9 the I_{PiN} signal is received and pre-amplified. The noise cancellation input cancels out noise caused by power supply by subtracting the noise from the I_{PiN} signal at the gain stage. After the gain stage a conversion to logic signals is done by a comparator. The comparator converts the linear output of the preamps to logic signals. It incorporates internal feed back to adjust its threshold so that the 50 % duty cycle is maintained over the entire input signal range of 40-1000 μ A. The decoding begins in the logic circuit shown in Figure 4.10(a).

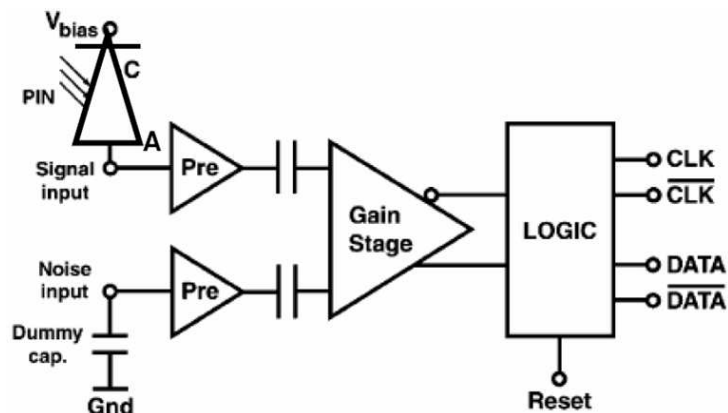
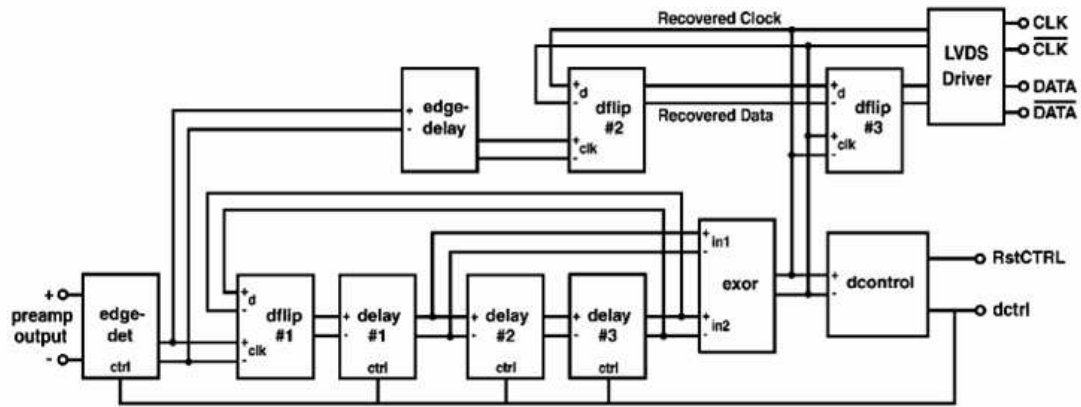
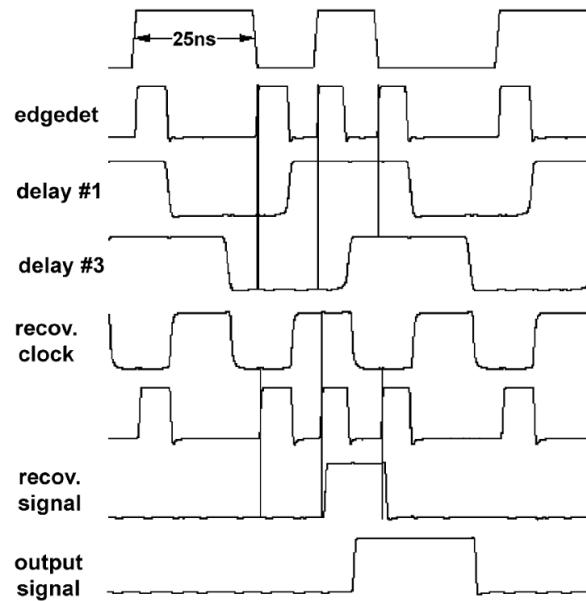


Figure 4.9: The DORIC general circuit schematic [21].

During the decoding process, an edge detecting circuit pulses at each input transition from the gain stage. These transitions correspond to the leading edge of the 40 MHz clock while others correspond to “1’s”. The circuitry is “taught” to recognize this by transmitting logic “0” after power up i.e the initialization process. As shown in Figure 4.10(b) the result of edge detection is a 40 MHz train of short pulses, a pulse per each edge of the input signal. Passing this to the dflip #1 connected to delay sets #1, #2 and #3 (see Figure 4.10(a)) each delaying by 6.25 ns, yielding a total delay of 18.75 ns. This being less than 25 ns, the dflip #1 toggles out 20 MHz. Hence at the “exor” the two inputs are 90° out of phase. This clock is passed on to decontrol for a conversion to DC voltage that controls the delays of #2 and #3 to keep the duty cycle to near 50%. The initialization period ought to last 1 ms settling the delay lock loop before sending the data bits. [21]

To recover data bits the “edgedet” pulses are sent through a short delay to dflip #2 where the “D” input is the recovered 40 MHz clock. The timing guarantees that sending a logic level 1 sets dflip #2. Dflip #3 synchronizes the recovered data to the recovered clock and increases it’s width to the full-recovered clock period creating a standard non return to zero data signal. Resetting the DORIC which is done after power up and initialization allows for slow and controlled recovery of the delay control circuit without the need to cycle the DORIC power [21]. As concerning the decoding threshold limit when no PiN current signal is sent, the DORIC has no lower limit and thus can decode noise.

The DORIC decoding activity results into Low Voltage Differential Signals (LVDS) of 40 MHz clock, with duty cycle within $50 \pm 4\%$ and with jitter below 0.5 ns and command

(a) *DORIC Logic decoding circuitry.*(b) *The decoding process.*Figure 4.10: *The DORIC decoding logic and the corresponding BPM signal decoding process [21].*

signals. Both type of signals have rise and fall times below 1 ns. The delay between the recovered clock and data is approximately 2 ns. The LVDS quality is within the range acceptable by the MCC of signal average (1.0-1.5 V) and amplitude (0.2-0.5 V). These properties of the DORIC have been found to be consistent in many tests performed prior to production and have also found not to change with irradiation [21,38,39,40,43]. Figure 4.11 shows that the lower PiN threshold of the DORIC is below $40 \mu\text{A}$ and that it does not change significantly with irradiation.

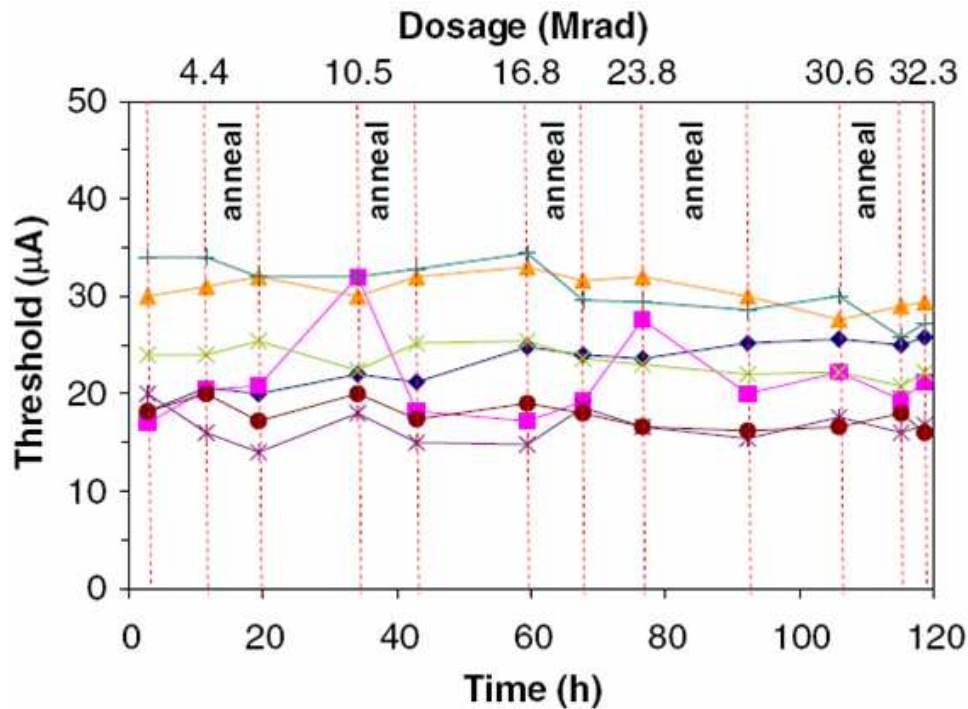


Figure 4.11: *DORIC* thresholds during irradiation measured on a 7 links board during irradiation. [21].

The VDC

Figure 4.12 shows the features of the VDC circuit. The VDC receives module data in LVDS and converts this into a single ended signal appropriate to drive a VCSEL array. The design of the circuit is such that the output current that flows into the VCSEL is variable between 0 to 20 mA. This is done externally by an V_{Iset} function.

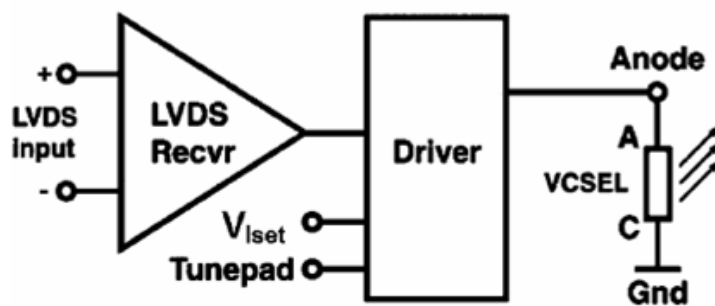


Figure 4.12: *The VDC circuit diagram.* [40]

The light signal amplitude is therefore set by this function. This function sets the same current through all channels of the VDC, thus one setting of V_{Iset} controls the VCSEL driving current (I_{VCSEL}) for all VDC chips on the board. By design the VDC amplifies

the I_{set} current by a maximum of 14 times. The amplified current is driven through the VCSEL and is given by $I_{VCSEL} \approx 14 \cdot I_{Set}$ mA. The lasing current will differ from channel to channel by $\approx 3\%$ resulting from slight variation of channel to channel resistance. Hence the light out the VCSEL is gaussian distributed. A constant default dim current of ≈ 1 mA ensures that the VCSEL is at “ready to switch on position” for good switching speed below 1 ns. The dim current can be set using the “Tunepad” function but it is set to an optimized default value of 1 mA without need of another setting. The VDC is powered with 2.5 V and has a constant power consumption of ≈ 22 mA when no VCSEL driving current is flowing through, that is, at $I_{Set} = 0$.

The sum total of the current consumption on an opto-board, the I_{vdc} , has a component that depends on the I_{Set} current and regardless of the VCSEL output state the current consumption after an I_{Set} setting is constant. This is due to a dummy driver circuit in the VDC that draws an identical amount of current as if flowing through the VCSEL when it is on. This reduces the noise on the opto-board. The dummy load circuit is controlled by the input signal states. During opto-board testing the magnitude of I_{Set} current is the reference. This is because the same V_{Iset} value will issue to different I_{Set} depending on the number of VDC chips on the opto-board. A nominal value of $V_{Iset}=0.9$ V is used during tests. Table 4.1 summarizes the I_{Set} current flowing into the opto-board type at 0.9 V V_{Iset} setting. The relation between the two parameters is shown in Figure 4.13.

opto-board type	Number of VDCs	Links	I_{Set}
Layer (1,2 and Disks)	2	7	1.1 mA
B-Layer	4	14	2.2 mA

Table 4.1: *The table summarises the I_{Set} current on the opto-board at the nominal $V_{Iset}=0.9$ V. This Voltage sets an $I_{Set}=0.56$ mA per VDC chip.*

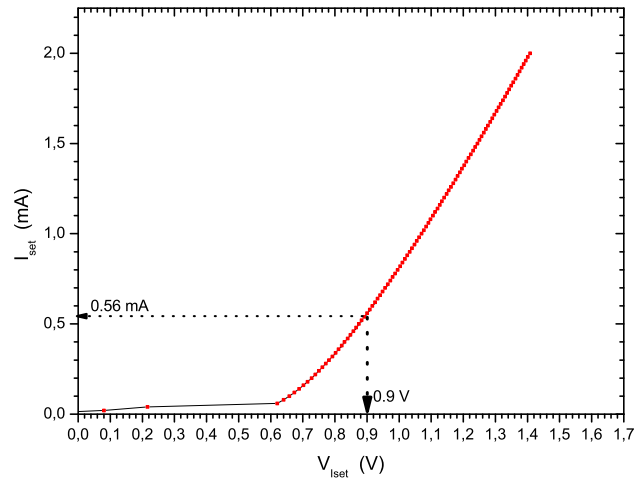


Figure 4.13: *The relation of the I_{Set} to V_{Iset} on the opto-board [39].*

4.6 The Optical Fibres

There are two key requirements for optical fibres to meet if they are to be used for the opto-link in ATLAS: first they have to be radiation hard and second the optical signal should experience least attenuation during transmission. Such fibres have been decided on after sufficient study in environments such as will be for the ATLAS experiment [44]. The Graded Index (GRIN) fibre with a predominant germanium doped core and the Step-Index Multi-Mode (SIMM) with a pure silica core are to be utilized in the transmission of the optical signal. The SIMM fibre is sufficiently radiation hard, with measured attenuation of ≈ 0.05 dB/m at 330 kGy(Si) and $1 \times 10^{15} n(1 \text{ MeV Si})/cm^2$. The extrapolated worst case total attenuation after irradiation on this type of fibre is less than 0.1dB/m working on the irradiation values at the pixel detector region which is 500 kGy(Si) for γ and $1 \times 10^{15} n(1 \text{ MeV Si})/cm^2$ for neutrons. The SIMM fibre is for the first ≈ 10 m for the region the ATLAS radiation scheme shows to have high radiation ^f [45].

At the region defined by ≈ 10 m, the 10 year radiation level is 0.8 kGy(Si), a factor ≈ 650 less for γ and $0.2 \times 10^{14} n(1 \text{ MeV Si})/cm^2$ a factor 50 less for neutrons for which the GRIN fiber shows an attenuation of 0.1 dB/m for the worst case. The GRIN type is utilized for transmission for the rest of the transmission length to the counting room (USA 15). The SIMM fibre has a modal dispersion of 30ns/km. The GRIN fibre has lower light attenuation per unit length before irradiation than the SIMM fibre thus preferred for transmission for the longer length where there is no irradiation.

4.6.1 The Light Signal Coupling

Figure 4.14 shows optolink with the fibre connection scheme. The optical fibers are built into ribbons, with a ribbon consisting of 8 fibers, which is the modularity of single optopackages. The ribbons are then made into cables for convenience in handling and for protection.

Starting from the on-detector side, the optical signal is transmitted for a length of 2.51/2.26 m from the PP0 to PP1. For this length, two types fibre ribbons in length are implemented by design with respect to opto-board positions on PP0. The connection to the opto-board on the PP0 is such that the two 8 fibre ribbons from the MF 16 connector on the PP1 side connect to the optopackages via an MT as shown in Figure 4.15.

After PP0, for a length of ≈ 12 m the 50 μm stepped index multimode (SIMM) radiation hard fiber is used. But there is a splicing where the SIMM fibres are singly connected to the Graded Index Multimode (GRIN). This splicing connection is distributed over 3 m so as to distribute the connection points. The optical connection at PP1 is via an MF 16 connector (shown in figure 4.16). The connector types apply also for data lines, colour coding differentiates the type of cables, where yellow is for data lines and blue for TTC

^fThe SIMM could have been utilized for the whole transmission but technical issues arising from fabrication led to a decision to utilize the already available length for the first 10 m.

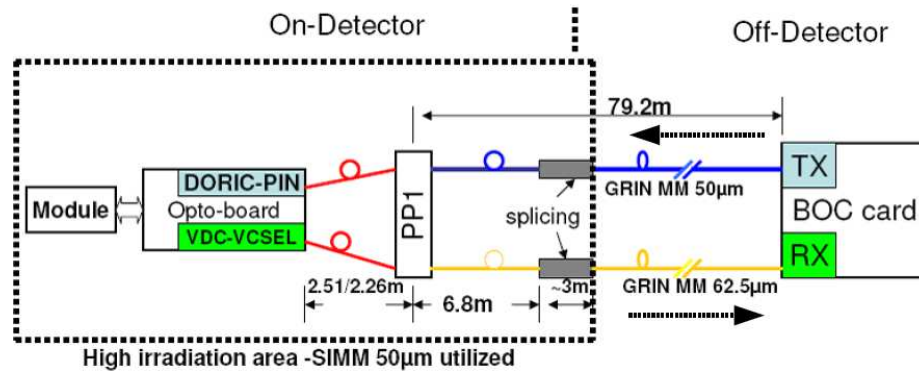


Figure 4.14: Shown is the optical linking infrastructure between the off-detector and on-detector electronics with the optical fibre lengths and type indicated.

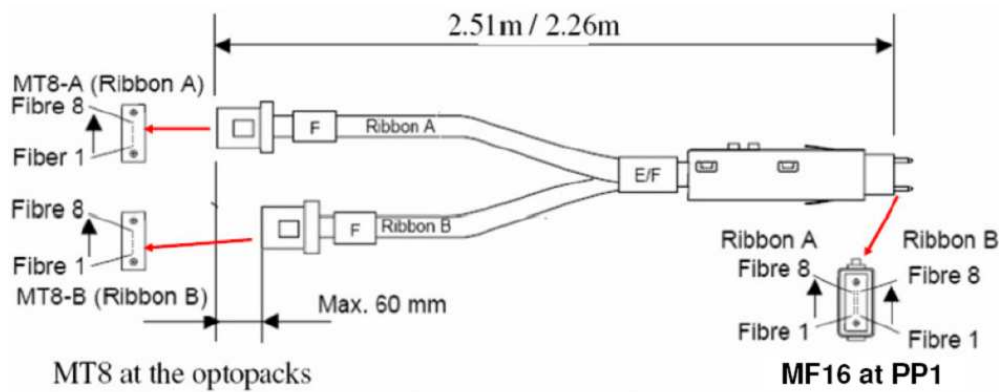


Figure 4.15: The "Y" cable implemented for connection between the opto-board and the PP1.

lines. For the data lines, the 50 µm SIMM fibre is spliced to the 62.5 µm GRIN therefore maximizing light coupling.

At the BOC card the light signal out of the TX-plugin is coupled to the fibre transmission by an SMC connector (shown in figure 4.16) utilized for all optical connections to the optical plug-ins at the BOC card.

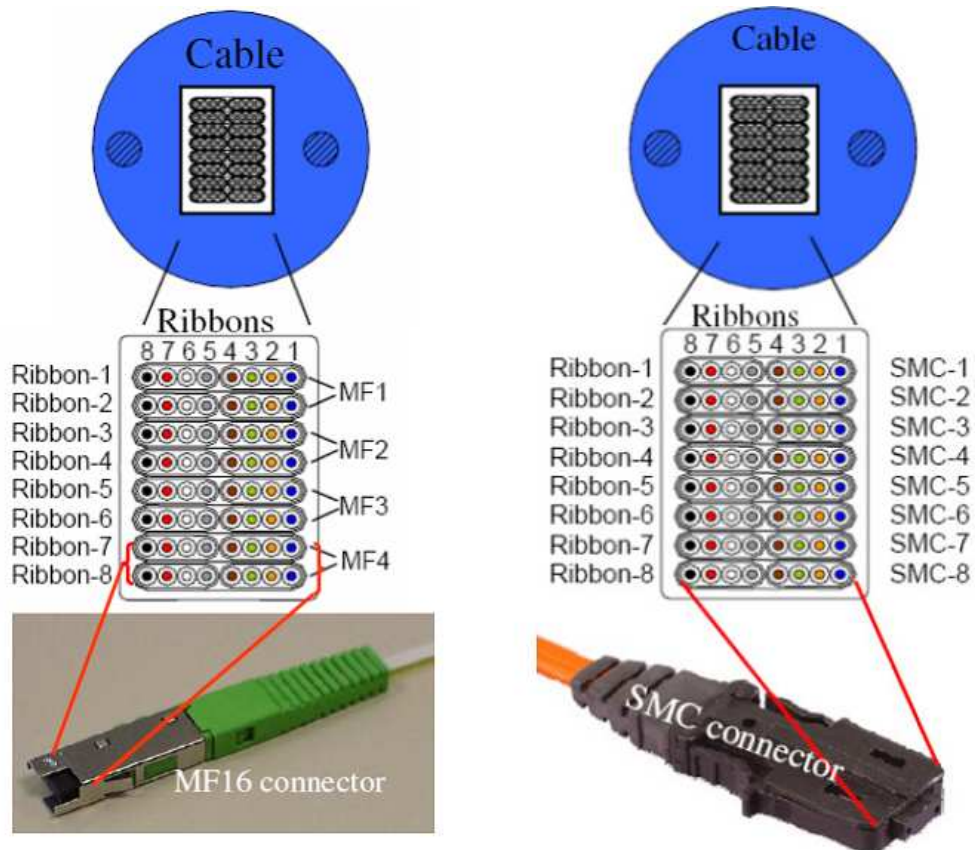


Figure 4.16: Shown are the terminating connector types utilized at the PP1 (left) and at the BOC card (right).

Chapter 5

The Opto-Board Production and Results

In Chapter 4, an introduction to the opto-board has been given. In this chapter the opto-board production and results are discussed. Below is a pictorial overview of the production set-up that was developed at the University Wuppertal. Its functionalities will be described in the sections.

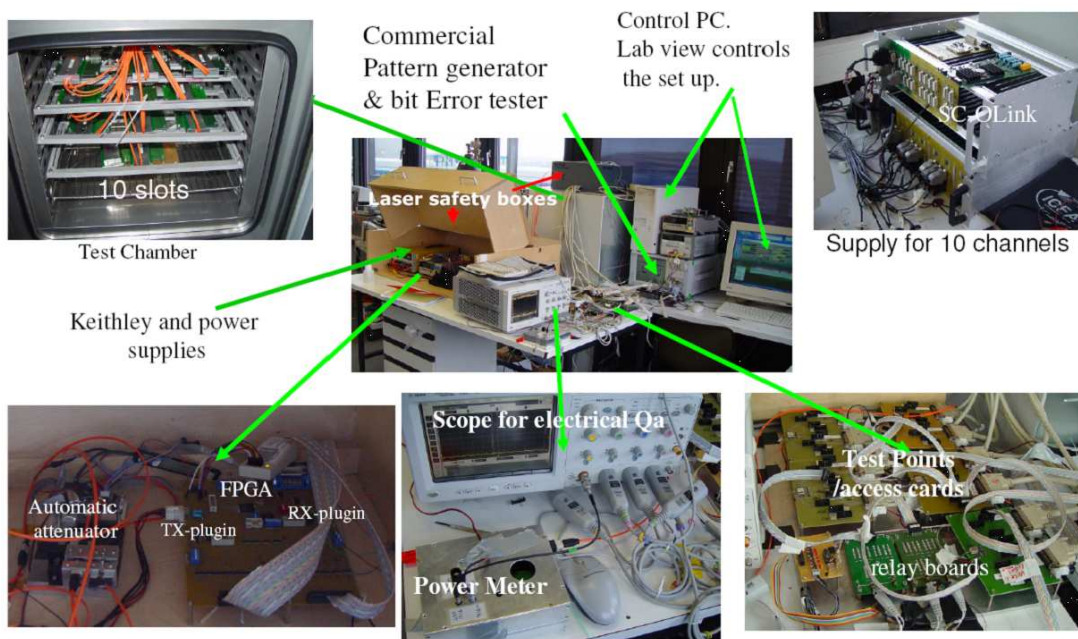


Figure 5.1: Overview of the production set up at Wuppertal.

The assembling and qualification of the opto-boards occurred in three labs of the collaborating institutes namely Ohio State University (OSU), the University of Siegen and the University of Wuppertal. Assembling process and measurements involved took place on the same site at OSU. The University of Siegen and the University of Wuppertal

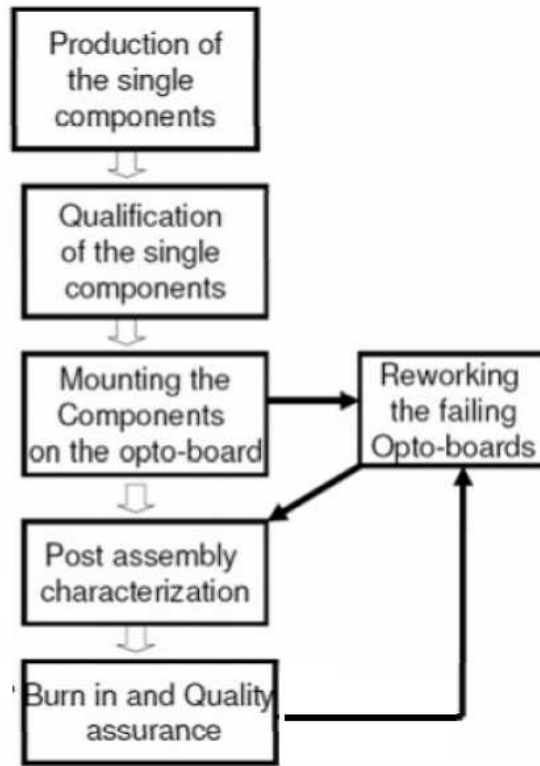


Figure 5.2: A flow chart illustrating the steps followed during the opto-board production process.

shared the role. The opto-board assembly and all pre-assembly and post-assembly functionality measurements took place at the University of Siegen and all production quality assurance (QA) measurements took place at the University of Wuppertal.

A total of 300 opto-boards were aimed for production. The overall production role between Ohio and Siegen/Wuppertal was in the ratio of 3:1. In this chapter the opto-board production and the results from all sites will be discussed. The measurements from all production sites are analyzed in this thesis while noting the institutes responsible for the measurements. The analyzes served as an input to the simulation discussed in this work as well. Apart from the analysis, the discussion is based on the setup at Wuppertal. Opto-board production process followed the flow shown in Figure 5.2. The production steps were as follows:

1. Fabrication of the individual components:
 - (a) Opto-board beryllium oxide substrate (best chosen for heat management) and mounting of the capacitors and resistors ^a
 - (b) The VCSEL and the PiN diode fabrication.^b

^aFabrication, Incorporation and population with passive components by Advanced Assemblies Incorporation. (USA)

^bFabrication and initial testing by True Light, Taiwan

- (c) The ASICs: the DORIC and the VDC. These were designed at Ohio State University (OSU) and at the University of Siegen and fabricated at IBM^c.
2. On site pre-assembly measurements of the individual components. The ASICs were checked on wafer at OSU.
 3. Mounting the optical packages (PiN diode and the VCSEL) and the Chips (the DORIC and the VDC), wire bonding and potting.
 4. Post assembly functionality measurements.
 5. Complete thermal quality assurance (Q/A) tests that included burn-in, thermal cycling and final measurements.

5.1 Fabrication of the Single Components

Part	Processes	Quantity
Beryllium oxide substrate	mounting \approx 25 passive components on each: 1) capacitors-(22 nF, 100 nF and 1 μ F), 2) resistors (0 Ω and 1 k Ω), 3) 80-pin JAE connector - connectivity tests	300
The VCSEL and the PiN diode [46]	Opto-array fabrication, minimal burn-in and thermal cycling and testing	450
The DORIC and the VDC	wafer production and testing	-

Table 5.1: *A summary of the opto-board components individual fabrication and the corresponding statistics [47].*

The Table 5.1 summarizes the details of opto-board production and fabrication of the components ^d. It also shows the components fabrication and the quantities that were delivered to the assembling sites. The fabrication was done after final design submissions. It was also after a detailed study on the prototypes under all expected operating conditions of irradiation and design of the ATLAS Pixel detector.

^cInternational Business Machines

^dDue to less numbers of the opto-boards more components have been produced even after the initial production was complete.

5.2 The Qualification Specifications

All the quality specification of the ATLAS pixel detector optoelectronic readout components are of course driven by the detector design (likewise to all detector parts in general). This is in order to achieve the physics goals described in Chapter 1 and as well adapt to the environment in which the detector is to operate.

Funtionality	units	min	max	Comment
current consumption	mA	177	depends on board type	330-400 (14-links board). 200-270 (7 links board). -fluctuations $\leq 5\%$ of the expected Q/A value.
Optical Power	μA	500	-	$I_{Set}=0.55mA$. Optical power fluctuations $\leq 20\%$ of the expected Q/A value.
rise and fall time	ns	-	1	for recovered 40 Mhz clk and data signal at PiN currents $100\mu A$, $1000\mu A$.
Jitter	ns	-	0.5	for clk and command at $I_{PiN}=50\mu A$, $1000\mu A$.
Duty cycle	%	46	54	for clk and command at $I_{PiN}=50\mu A$, $1000\mu A$.
clock and command $+/-$ common modes	V	1.0	1.5	for clk and command at $I_{PiN}=50\mu A$, $1000\mu A$.
clock and command $+/-$ amplitude	V	0.2	0.5	for clk and command at $I_{PiN}=50\mu A$, $1000\mu A$.
dark current	μA	1	-	+10V
bit errors		0	0	$I_{PiN}=50\mu A$, $1000\mu A$. for 60 mins with all links active

Table 5.2: A summary of the opto-board quality assurance limits [48].

In Table 5.2 a summary of all the optical and electrical quality specifications of the opto-board is given. These were the specifications applied to determine the good opto-boards during the characterization. They are adopted to the following: The data optical signal from the the VCSELS must survive the fiber length attenuation even after irradiation. Hence during characterization measurements, all the VCSELS must emit light above $500 \mu W$ at the nominal setting of the $V_{Iset}= 0.9 V$. The rise and fall time of all of the signals on the opto-board must be below 1 ns hence ensuring fast signal transitions for proper detector readout.

In Chapter 7 a timing simulation is presented there to studying the aspect of duty cycle behavior of the link. The duty cycle ought to be nominally $50\pm 4\%$. It is also required that the quality of the low differential voltage signals have an amplitude of 0.35 V and a common mode of 1 V, however there is a wide range for this property of the signal and

the limits are not constraining. Topping the qualification when all other properties are observed as within limits is the bit error rate. A good bit error rate requires that many bits are sent continuously over a longer period. During the Q/A bits counted for a period of one hour were giving a possibility to decide on the good boards opto-boards. A bit error test of 5 minutes was applied during other measurement phases done during the assembly to ensure that the boards are functional.

5.3 Thermal Characterization Requirements

According to the cooling scheme of the ATLAS detector the region at which the opto-boards are placed will operate at a nominal temperature of ≈ 10 °C. This temperature also provides optimal working condition for the electronics mounted there on. During the normal detector operations of power up and power down and detector rest (when not in use) different thermal-mechanical conditions will be exacted on the components of the opto-boards thus similar conditions are simulated in a thermal test in the laboratory which involves a burn-in at 50 °C and thermal cycling between 50 °C and -25 °C of the test chamber temperature^e. Burn-in test was done for a period of 72 hrs and after 10 temperature cycles done with a soak of 1 hr at -25 °C. The tests had in view to eliminate boards with weakened contacts at solders and at glued parts. It was also aimed at observing the consistency in functionality of the opto-board properties under “stressed” conditions thus increasing the confidence level of their ability to function in the ATLAS detector’s harsh environment.

5.4 The Test Set Up

The opto-board production set up meeting the test requirements of the opto-board was set with the following key properties:

1. Data generation and testing at bit pattern of choice. The key modes utilized for this are the random bit pattern (PRBS^f). The random pattern was the most useful for testing purposes. A clock pattern was utilized as well.
2. Optical electronic interfaces for optical to electrical (and vice versa) signal conversion. The ATLAS Pixel optical electronic plugins (the TX and the RX) prototypes were used for this purpose.
3. Optical and electrical signal characterization apparatus.
4. Software for automation, monitoring and data acquisition management and analysis.

^eThe opto-board experiences ≈ 16 °C more than the test chamber temperature due to self heating.

^fPseudo Random Binary Sequence: Generated by repeated selection of N bits in a bit array of PRBS having a $2^N - 1$ cycle, having all assumable bit arrays other than 0.

Modes Utilized For Testing

The testing modes utilized to do measurements on the opto-board were as follows:

1. The full loop-back mode: In this mode the BPM signal is sent to the TTC opto-board links (the DORIC) and then the decoded signals are looped back through the data links after which testing is done.
2. The optical loop-back mode: In this mode an electrical LVDS is sent to the VDC input and the optical signal generated at the VCSEL is tested or sent to the RX-plugin for optical to electrical conversion for testing.
3. The electrical loop-back: The BPM signal is sent to the DORIC and the decoded LVDS is tested.

The modes enumerated 2 and 3 above are sub-modes of the full loop-back. To test all the links simultaneously on the opto-board the full loop back mode was utilized as a main testing mode. Figure 5.3 shows a schematic of the full loop back mode.

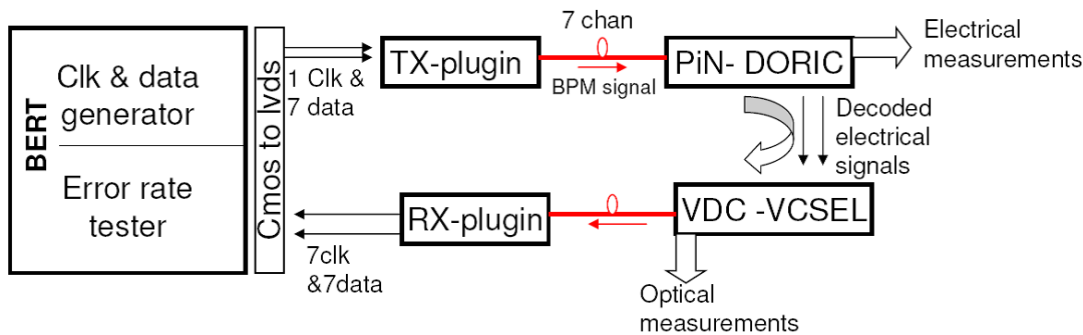


Figure 5.3: A diagram showing the minimal production test set up components in the full loop-back mode: Shown is the set up for a single slot, the set up consisted of 10 opt-oboard slots in the Test chamber.

In the full loop-back mode a data pattern was generated from a commercial pattern generator that consisted also of a bit error testing unit (the BERT). The BERT outputs CMOS, thus conversion from CMOS to LVDS was required. Set ups at OSU and Siegen utilized a programmable FPGA instead. The pattern generated was then transmitted to the TX-plugin prototype for encoding into a BPM signal. The TX-plugin optically sent the BPM signal to the opto-board TTC receiving part, the PiN connected to the DORIC. At the DORIC the BPM signal is decoded. The decoded command and the detector 40Mhz clock LVDS are then re-routed so as to send the data back through the data links of the opto-board. The data and clock signals are passed onto the VDC and then are optically sent to the RX-plugin for optical to electrical conversion. At this point the signals were linked back to the BERT for error rating. In the actual experiment set up the data channeling for reconstruction takes place after the RX-plugin hence the

reason of testing the signal bit error at this point. The other sub-modes were utilized to characterize the decoded command and clock signals after the DORIC and to characterize the optical power signal out of the VCSEL. These submodes enable a characterization of individual links, TTC or data.

The test setups in all the three production sites had all the key characteristics discussed above meant to characterize one opto-board at a time. This was the basic setting. Other on site adaptations were implemented to meet the need to increase the production and measurement rate. Hence necessary hardware and automation processes were developed. Unique to the system developed at the University of Wuppertal was the element to enable upto 10 opto-boards be tested at the same time during the burn in and thermal cycling phases and a serialized automated testing was developed for the electrical and optical characterization. All utilized the same temperature testing chamber with a procedure that 10 opto-boards would be put into the chamber in the carrier slots. They were kept in that setting till the end of all testing phases. For this reason testing was in batches of a maximum of 10 opto-boards. Another unique feature of the set up at Wuppertal was the utilization of parts of the official ATLAS Pixel power sourcing equipment for the opto-board (the SC-OLink) thus enhancing parallel testing and eased monitoring and data taking process. The needed interfacing software was developed.

5.5 Standardizing the setups

A production prototype opto-board was sent around on all sites for measurement. There was need to do a measurement on the same board on all sites and compare the results with the qualification specifications with an aim to standardize all set ups used for production. especially those done on the optical power have often showed significant differences due to the sensitivity involved (and also error prone) and given that the convenient measuring devices had to be developed in the labs using photo detectors meeting the qualification to measure the optical signal at 40 MHz with wavelength λ of 850 nm. Shown in Figure 5.4 are measurements on the optical signal at the VCSEL.

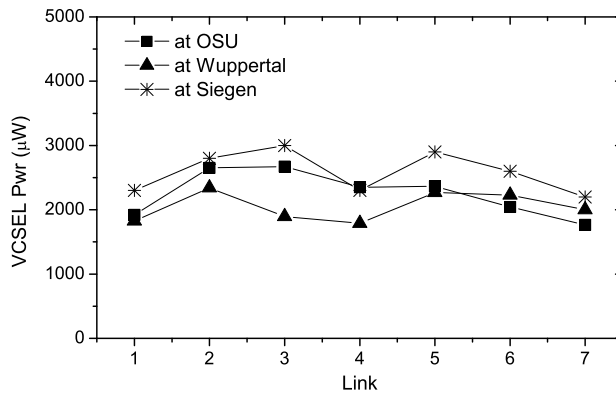


Figure 5.4: *Optical power measured on the same board. The measurements are values within the specification limits.*

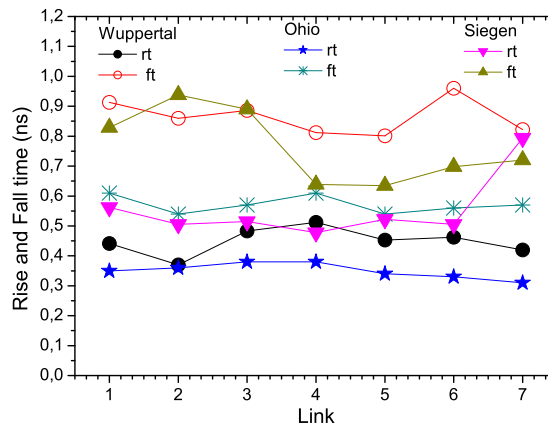


Figure 5.5: *Optical power rise and fall time (denoted by rt and ft) at the nominal I_{set} setting of 0.56 mA . Measurements from all sites below 1 ns .*

The setups measured the optical power differing with 15% on average. Some channels differed with 30% of the expected value of $2 \pm 0.4\text{ mW}$ at the nominal V_{Iset} of 0.9 V at room temperature. Thus indicating the difficulty in optical power measurement reproducibility. The optical signal rise and fall time was below 1 ns qualification value as shown in Figure 5.5.

Shown in Figure 5.6 is the decoded data and clock LVDS common mode which is 1 V on average and the amplitude 0.39 V . As mentioned earlier the allowance for these properties is a wide range but the opto-board decoded signal ought to characteristically yield these values on average for a nominally functioning board.

The duty cycle and the jitter of the recovered 40 MHz clock is shown in Figure 5.7. The

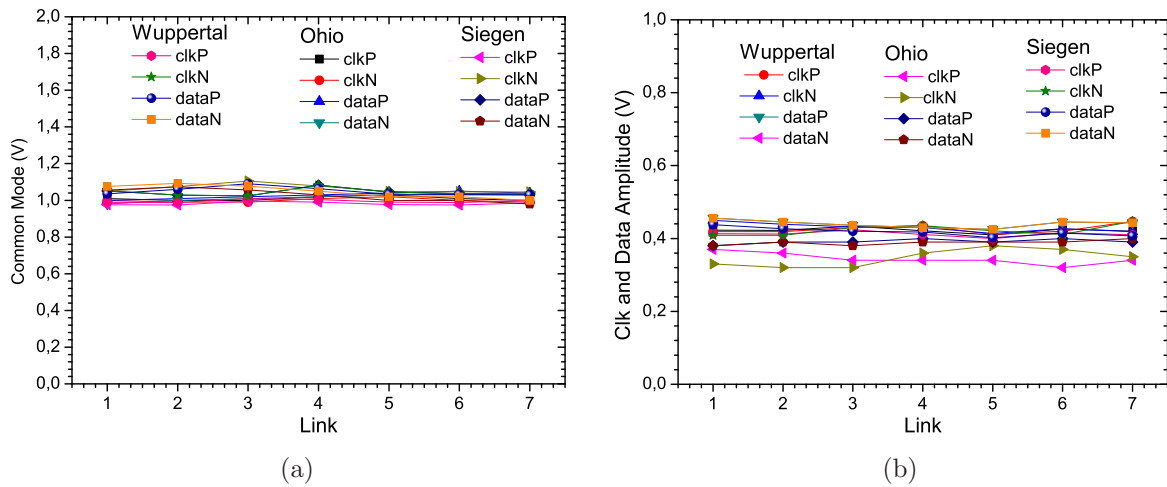


Figure 5.6: Shown in (a) is the electrical common mode LVDS measured on the decoded data and clock and (b) is the LVDS amplitude the decoded data and clock signal.

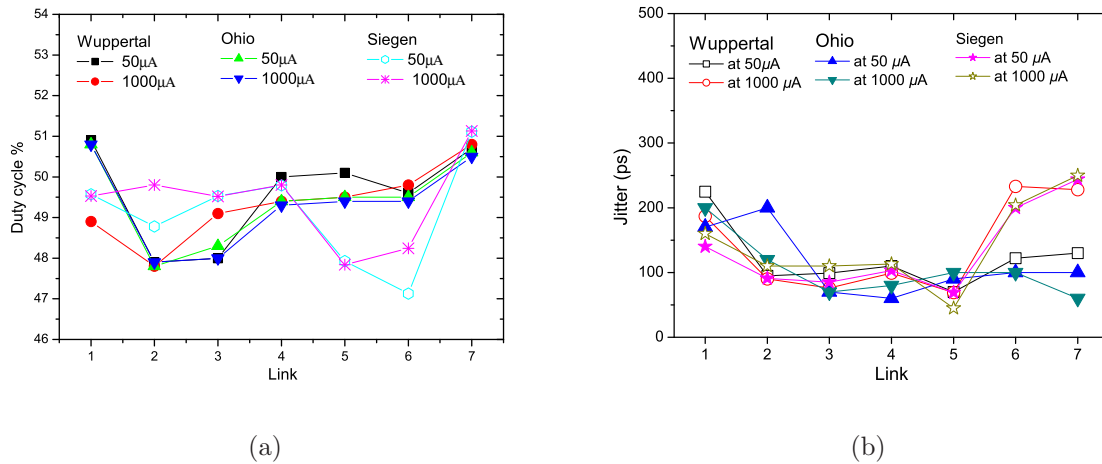


Figure 5.7: Shown in 5.7(a) is the electrical duty cycle measured on the decoded clock at the opto-board at PiN current settings near the DORIC lower threshold and at 1000 μA while 5.7(b) shows the jitter result.

result meets the specification on all sites and the differences observed between measurements are not significant apart from those of optical power. This indicates the necessity to measure optical power several times and check for consistency before the opto-boards

are to be installed in the detector^g.

5.6 The General Production Measurements Steps

In this section a summary of the main production steps and the measurements that were done are summarized. The individual production steps and all the specific evaluation are referenced to the Pixel opto-board production documents [46, 47, 48]. Table 5.3 summarizes the main measurements that were done during the production steps. In the sections to follow sets of measurements from each step will be analyzed in detail.

Production step	Site	Measurements	Limits
Before assembly	OSU/Siegen (measurement on individual components)	Mechanical tolerance and Short tests	-
		VCSEL power	power > 500 μ W power drop < 40 %
		PiN responsivity	R > 0.5 A/W
		PiN dark current	< 1 μ A
After Assembly	OSU / Siegen (functionality check of the completed opto-board)	Power consumption	Q/A limits in Table 5.2
		Electrical tests	
		Optical tests	
		5 min BER	
Burn-in at 50 °C NTC=64 °C	OSU / Wuppertal	Power consumption	
		Optical power and signal waveform	
Thermal-Cycling between 50°C and -25 °C ⁴ (-10°C NTC)	OSU / Wuppertal	Power consumption	
		Optical power and signal waveform	
Complete QA at 10°C (24 °C NTC)	OSU / Wuppertal	The complete list in Table 5.2	

Table 5.3: *The main measurements that were done during the production process.*

5.7 Measurements before Assembly

Measurements were done before assembly to verify the functionality of the components received by shipping. The single components of the opto-board were tested at this stage

^gThis step has actually been implemented: optical power has been measured several times even due to problems associated with the VCSEL to discussed in latter sections

as required by the assembly document. For this work only the measurements of the optopacks will be discussed for this step. The VCSEL packages were measured for the optical power and PiN diodes for dark current and responsivities. Here the Optical power measured at Taiwan before shipment and OSU after shipment is analyzed. The result of reponsivites of the PiN diodes measured at the University of Siegen is also analyzed.

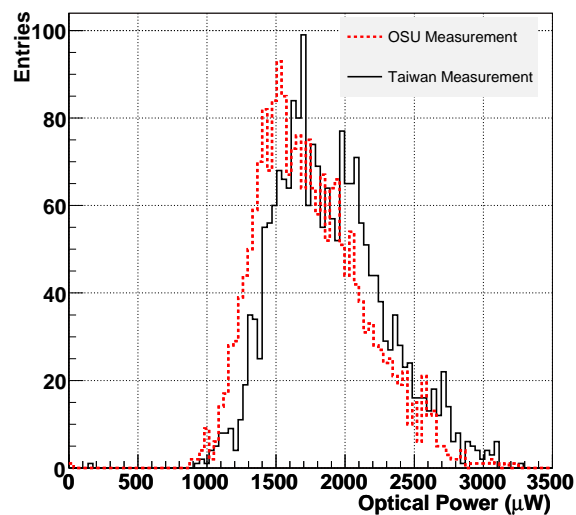


Figure 5.8: *The optical power of the 260 VCSEL opto-packages measured per channel at 10 mA forward current.*

Shown in Figure 5.8 are measurements on 260 VCSEL opto-packages measured at Taiwan after initial production and after shipping before assembly at Ohio. Figure 5.9 shows the distribution of per channel differences in these measurements. VCSEL optopacks with channels that had more than 40 % drop in power ($Taiwan/Ohio > 1.6$) were not mounted on the optoboards.

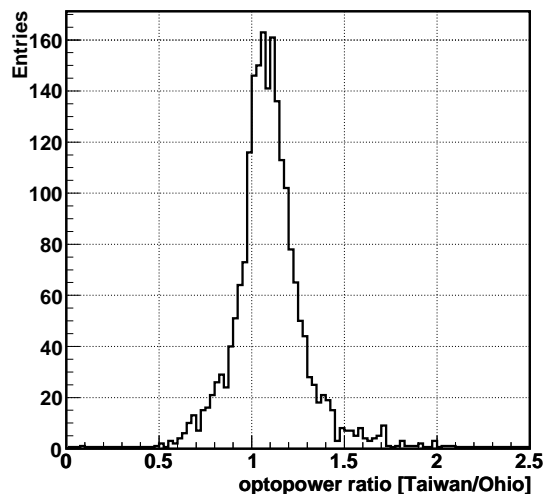


Figure 5.9: *The ratio difference between the the initial opto-package production measurement at Taiwan and after shipping preproduction measurement result at OSU. The distribution shows large drop in optical power measurement. VCSEls with channels that had power drop by factor >1.6 were not considered for mounting*

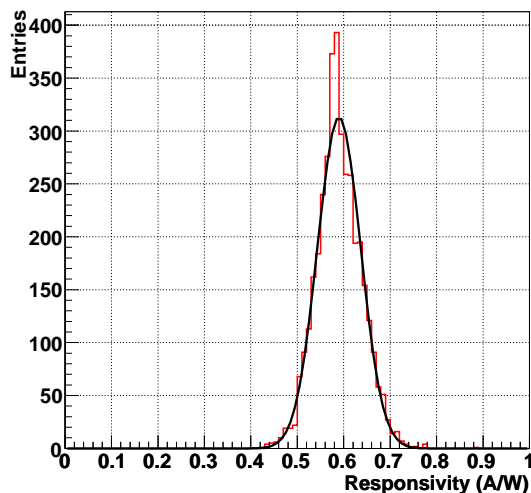


Figure 5.10: *Responsivities of 470 production PiN diode array channels measured at the University of Siegen and and OSU but analyzed within this work. The mean responsivity is 0.59 ± 0.05 A/W.*

Figure 5.10 shows the result of the PiN diode responsivities averaging $0.59 \pm 0.05 \frac{A}{W}$ before mounting. This was the only possibility to measure responsivities due to the difficulty in

accessing the mounted PiN on the opto-board for the measurement of this property.

5.8 Measurements After Assembly

Measurements done after the assembly can be divided in 3 parts namely: 1) the measurements done to check the functionality of an assembled board. 2) the measurements done during the quality assurance process of burn in, thermal cycling. 3) the quality characterization determining the detector worth opto-boards. These 3 tests phases are discussed separately.

5.9 After Assembly Functionality Measurements

At Ohio and Siegen the complete assembly of the opto-board at the current consumption of the opto-boards were measured. This was done at an $I_{set}=0$ mA, at which setting no current flows into the VCSEL, in order to check the current consumption of the VDC and the DORIC when powered with the working voltage of 2.5 V. This was also done at a setting of $I_{set} = 0.56$ mA per VDC chip, when a forward current of ≈ 10 mA is driven through the VCSEL. This was to check the functionality of the opto-board when the VDC drives a forward lasing current of 10 mA through the VCSEL channels. At this value of the I_{set} the optical power signal of the VCSEL channels is measured for amplitude and for rise and fall times assessing the quality of the signal. Likewise the TTC links of the opto-board are checked for functionality by sending an encoded BPM optical signal to the PiN and the resulting current signal is decoded by the DORIC for electrical characterization. All boards that passed this step are potted with glue and passed on to the complete Q/A phase while failing boards are reworked on.

5.10 Quality Assurance Measurements

Discussed here are the three steps of full quality assurance done on the opto-boards. All were done under a temperature condition. A summary description is discussed of each step and the results of the measurements are shown.

5.10.1 Burn-in Testing

The burn-in test of the opto-board was an important step aimed at eliminating the weak opto-boards by an accelerated but controlled aging process at 50 °C of test chamber temperature. For this test the opto-boards were powered with the nominal supply sourced by the SC-OLink voltage of 2.5 V and the nominal V_{Iset} of 0.9 V. The PiN diode was powered with 10 V. No signal was sent to the TTC links on the opto-board. Therefore the DORIC decoded noise. For the data links a 40 MHz clock signal was sent through

such that all the VCSELs lasing out the clock power keeping the VDC chip in an active state. This enabled the testing of the dummy load of the VDC sampling circuit. The temperatures of the opto-board in the test chamber were read out via the NTC channels of the opto-board. The opto-board experienced NTC temperature of 65 °C due to self heating.

During this test all the voltages, the currents and the temperatures were monitored. The functionalities of the opto-board were checked to determine any indication of failures and instabilities. The procedure of this test was to load the opto-boards onto the test slots in the test chamber and measure all the voltages and currents and this had to be ascertained whether to be consistent with the expected values and then the boards had to go an initial close monitoring observation for the first 2 burn-in hours. During the mid burn-in time, after ≈ 36 hrs the opto-boards were tested for functionality.

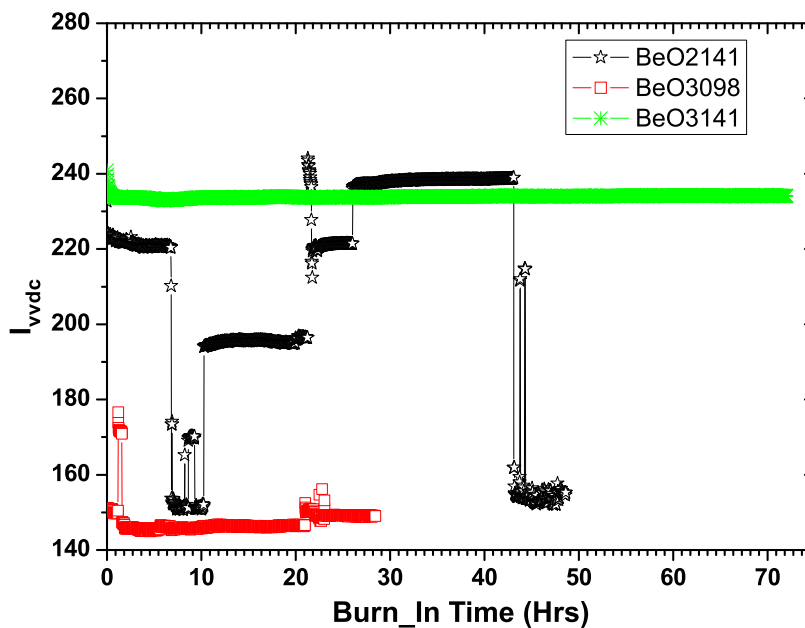


Figure 5.11: *Shown is the I_{vvdc} behavior of three opto-boards measured at Wuppertal. The straight stable line shows the current consumption of a good board while the other two plots show the power consumption of two defective boards during burn-in.*

At this stage some opto-boards showed inconsistencies associated with V_{iset} and hence the VCSEL. This was established to be so since the boards with the named inconsistencies would show current consumption (I_{vvdc}) fluctuations. In Figure 5.11 the general behavior of the power consumption of the boards is illustrated by three opto-boards. Opto-board 3098 went through the full test. Opto-boards 3141 and 2141 showed current consumption inconsistencies attributed to the VCSEL problem during the burn in phase. In Figure

5.12 the mean power consumption and the deviations are shown. The boards with large deviations (current consumption fluctuations $\geq 5\%$) and with no power emitted out of the VCSELs were declared to be faulty. The component of current consumption of the opto-board above $I_{set}=0$ is the lasing current flowing to the VCSELs or the dummy load when the VCSEL is in the off state. Any fluctuation of more than 10% in this component gives the message of unstable VCSEL or the dummy load circuitry.

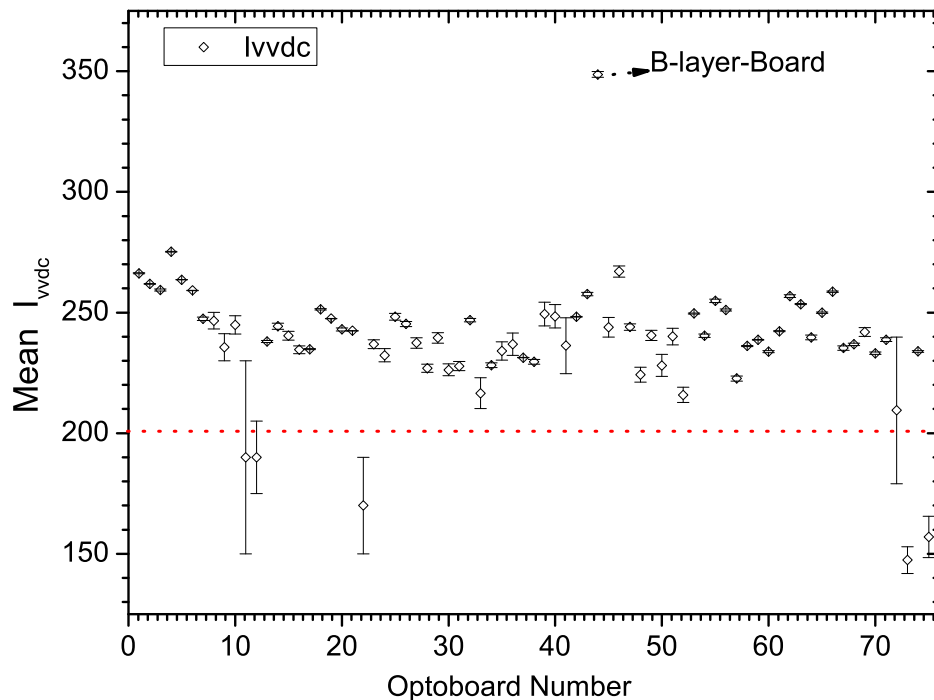


Figure 5.12: *The mean power consumption of the opto-boards during burn-in. Large I_{vvdc} fluctuations were observed on a total of 6 opto-boards measured at Wuppertal that failed the Q/A as a result. The boards had the mean I_{vvdc} below 200 mA and with large fluctuations as shown.*

As shown in Figure 5.12 6 opto-boards failed the Q/A because they had the I_{vvdc} current fluctuating by more than 5%. Some boards which had I_{vvdc} below 200 mA, though with fluctuation less than 5%, they were faulty because they had no optical power. During the burn-in and the thermal cycling phase, discussed next, a functionality check on the optical 40 Mhz signal was visualized on the scope to ensure that all channels have the correct output signal and are functional.

5.10.2 Thermal Cycling

To implement simulated cool down and warm up phases during the operation of the ATLAS pixel detector, a laboratory and achievable setting to this condition of “harshness”

was achieved setting the Climatic Test Chamber to the highest attainable ramp up and ramp down of temperature cycles. Figure 5.13 shows the result from one of the batches of 10 opto-boards during the thermal cycling phase. Temperatures are measured to the nearest half a degree. The warm up phase rate was $3\text{ }^{\circ}\text{C}/\text{min}$ while that of the cooling phase was $2\text{ }^{\circ}\text{C}/\text{min}$. This results from fitting linear to the warm up and cooling phase of the cycles. The opto-boards may in the real sense experience harsher conditions than these simulated ones while in operation in the detector but this test provided sufficient “stress” to decide on weakened opto-boards while avoiding to age them before use. A functionality check was done at the beginning and the mid of the session. All boards that successfully tested functional during the burn in phase also tested functional during thermal cycling phase.

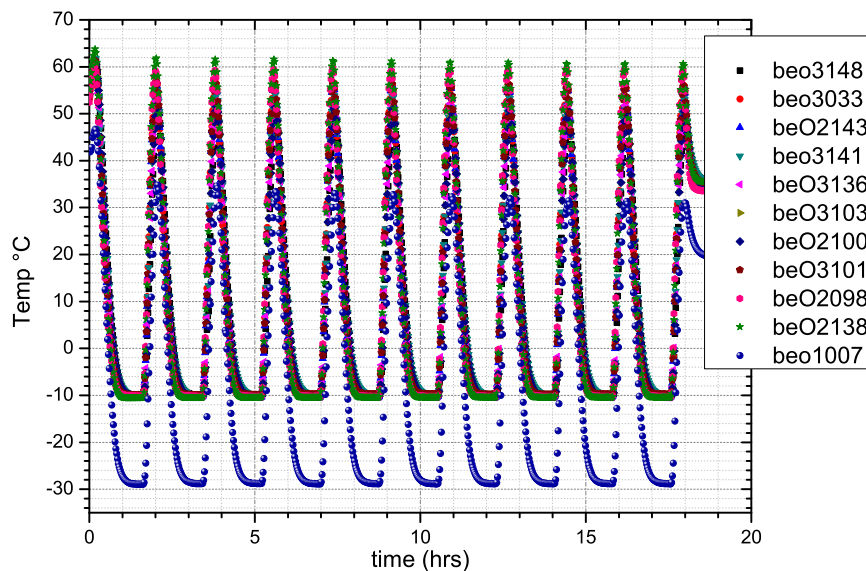


Figure 5.13: *Result at Wuppertal showing a typical thermal testing phase. BeO 1007 a faulty non powered board utilized to read out chamber temperature.*

The procedure for this phase was first to inflow nitrogen into the chamber before the start of the test at a higher rate for 5 minutes and then set to a constant low flow rate that was to remain till end of the test. This measure in addition to the moisture trap feature of the test chamber kept the environment in the chamber dry. The opto-boards were powered with the nominal voltage settings (as described for the burn in).

5.10.3 Full Characterization

Detailed measurements were done at $10\text{ }^{\circ}\text{C}$, the ATLAS detector nominal working temperature at the opto-board region, characterizing fully the optical and electrical characteristics of the opto-board. This part summarizes each measurement distribution. The

measurements obtained here not only were used to decide on good opto-board that had successfully passed through burn-in and thermal-cycle test as required by the Q/A cuts (see Table 5.2) but also the data served as input into the simulated study discussed in later chapters.

Electrical Measurements at 10°C

The electrical measurements were done on the electrical signals decoded by the DORIC (the TTC links). A comprehensive measurement set was done to ensure that the signal maintained quality at various settings of the opto-board derived from the detector working settings. Signal properties of the recovered 40 MHz clock and command signals were measured at near DORIC lower threshold defined by currents at the PiN diode of $I_{PiN} = 50 \mu\text{A}$ and $I_{PiN} = 100 \mu\text{A}$ and at the upper thresholds defined by $I_{PiN} = 1000 \mu\text{A}$. A basic procedure for an electrical measurement constituted of powering the opto-boards, measure the current consumption at the nominal settings of board supply $V_{vdc}=2.50 \text{ V}$, $V_{PiN}=10 \text{ V}$, and the V_{Iset} setting that sets $I_{Set}=0.56 \text{ mA}$ per VDC chip (for the test set up at Wuppertal this was between 0.938-0.973 V. At this setting the power consumption should be above 200 mA (see Table 5.2) and the PiN diode dark current below $1 \mu\text{A}$.

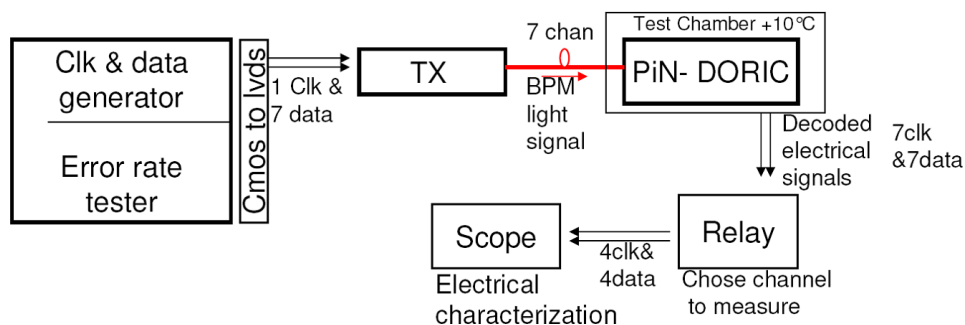


Figure 5.14: Figure showing the set up utilized during the electrical characterization of the decoded DORIC clock and command signal.

Figure 5.14 shows the basic set up utilized for electrical characterization. It consists of a data generation encoding at the TX and then the optical signal is sent to the TTC links (PiN-DORIC). The decoded signals are then routed for characterization. The electrical tests were tested using the electrical loop-back mode, thus enhancing automation. The full looping-back was only utilized for the BER measurement. A BPM signal having no data bits was then sent to the TTC links for DORIC initialization and then a reset signal. Thereafter a PRBS^h BPM signal is sent to the links and the decoded clock and command signals looped back electrically to the BERTⁱ for error test for which the links must record 0 error counts for 5 minutes before the begin of electrical tests. The electrical signals were redirected to the oscilloscope for measurements. The electrical testing was automated such that the measurement of duty cycle, rise and fall times, period and jitter at all set

^hPseudo Random Bit Pattern

ⁱBit Error Rate Tester

I_{PiN} currents mentioned earlier was done at one go per board. For the electrical signals, most sufficient was the measurements on the duty cycle and the jitter of the clock and also the rise and fall time of both clock and data signals. The absence of any polarity of the LVDS signal or the deformation of it in any channel leads to a deformed differential signal which is noted in the measurement of the characteristics. For this reason measurements on single polarities as regarding to amplitude and common mode was not emphasized at Wuppertal. However, the mentioned properties were measured during post assembly functionality check. The thermal tests would not change such a design intrinsic property. This has been tested extensively during irradiation in a cold box at $-20\text{ }^{\circ}\text{C}$ [21].

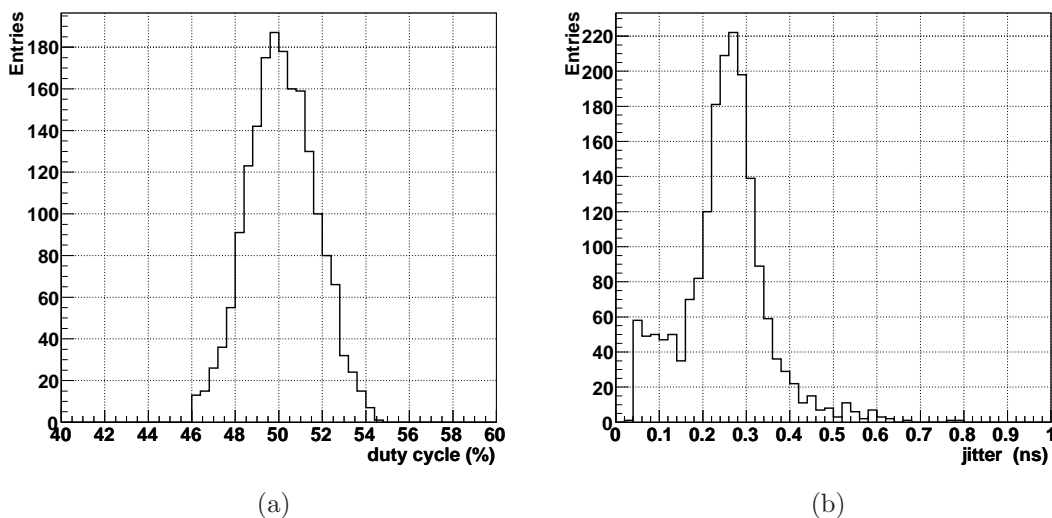


Figure 5.15: *The clock duty cycle (a) and clock positive width jitter (b) for the production optoboards measured at OSU and at Wuppertal during the Q/A. The mean duty cycle is $50.14 \pm 1.6\%$ and the mean jitter is $0.251 \pm 0.098\text{ ns}$.*

The clock and command qualities were observed not to vary by PiN current thus, presented is the result at near threshold PiN current setting being the most significant. Also the signal reaching the DORIC will be at lower ranges (see power calculation) of PiN current. In Figure 5.15 is shown the clock jitter and the clock duty cycle of the 40MHz clock at PiN current of $50\text{ }\mu\text{A}$. This meets the specification of $50 \pm 4\%$.

Figures 5.15 and 5.16 show that the 40 MHz clock and the data signal rise and fall time meet the specification requirement of time less that 1 ns. The few channels that show a slight deviation from these limits are due to systematic errors and not due to board property. This was confirmed by bit error test. These channels passed the “0” bit error count Q/A test.

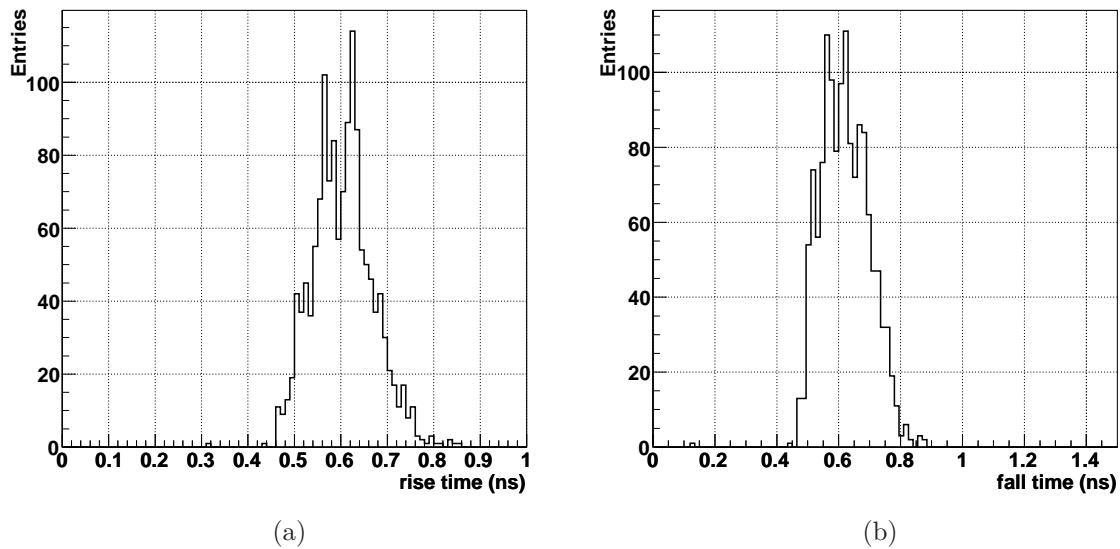


Figure 5.16: *The decoded 40 Mhz clock signal rise (a) and fall time (b) of the opto-boards measured at OSU and at Wuppertal. It meets the specification of less than 1 ns.*

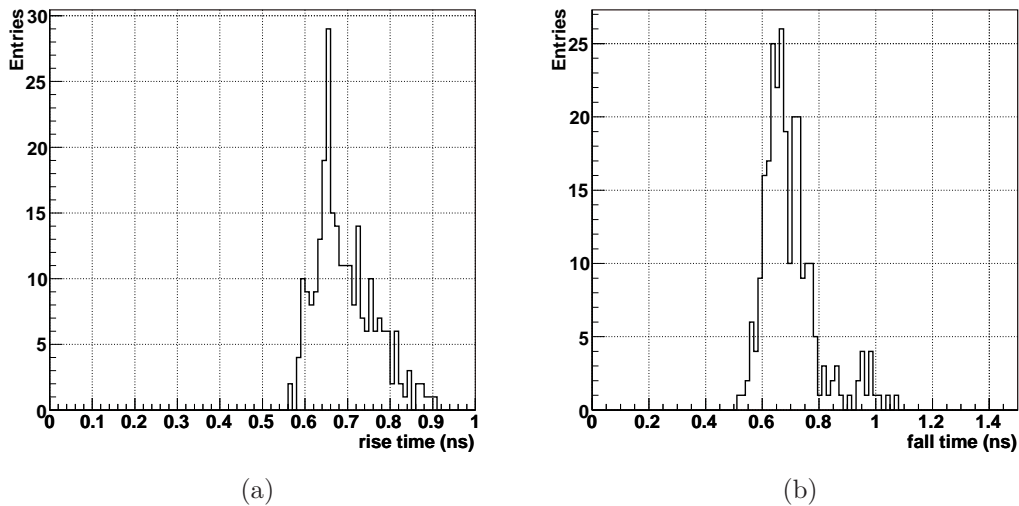


Figure 5.17: *The decoded command PRBS signal rise time (a) and fall time (b) of the opto-boards measured at Wuppertal. The signal meets the specification of less than 1 ns.*

Quality Assurance Bit Error Rate

A bit error rate (BER) measurement was done on the links utilizing the full loop-back mode and the electrical loop-back modes. A meaningful BER measurement requires long

periods. Such periods as to achieve an error rate of 10^{-12} , the experiment rate, is not realizable in a Q/A session for all boards, thus a 60 min period was defined. Hence only 1.44×10^{11} bits were sent through the links per board for two PiN current settings of $I_{PiN} = 50 \mu\text{A}$ and $I_{PiN} = 1000 \mu\text{A}$. The most significant setting was at $I_{PiN} = 50 \mu\text{A}$ being near the DORIC lower thresholds. This measurement was enhanced by checking if any cross-talk existed between channels. Thus an alternating data pattern to the links and alternating PiN current values between $I_{PiN} = 50 \mu\text{A}$ and $I_{PiN} = 1000 \mu\text{A}$ on the links from channel to channel.

A “0” error condition was required for the Q/A. All but one which had a broken channel passed this condition of no error required by the Q/A if links are functional. There were often induced error counts emanating from disturbances in the laboratory. This was due to the absence of filtering capacitors on the opto-board^j. This occurred when the surrounding utilizing the same supply lines were switched on the test as a result, during measurement all channels of the same board would record errors at the same time with few count differences but later stabilize. It was hence possible to deduce properly the errors resulting from the boards themselves or due to the system settings.

5.10.4 The Optical Characterization at 10°C

The amplitude of the optical signal out the VCSEL driven by the VDC was measured during the optical characterization. There was need to survey the waveform too. The optical power signal was surveyed during the functionality checks at -25°C and at 50°C to be discussed in the next sections.

^jConfirmed to be so during later re-tests at CERN before installation. Capacitor mounting has been organized

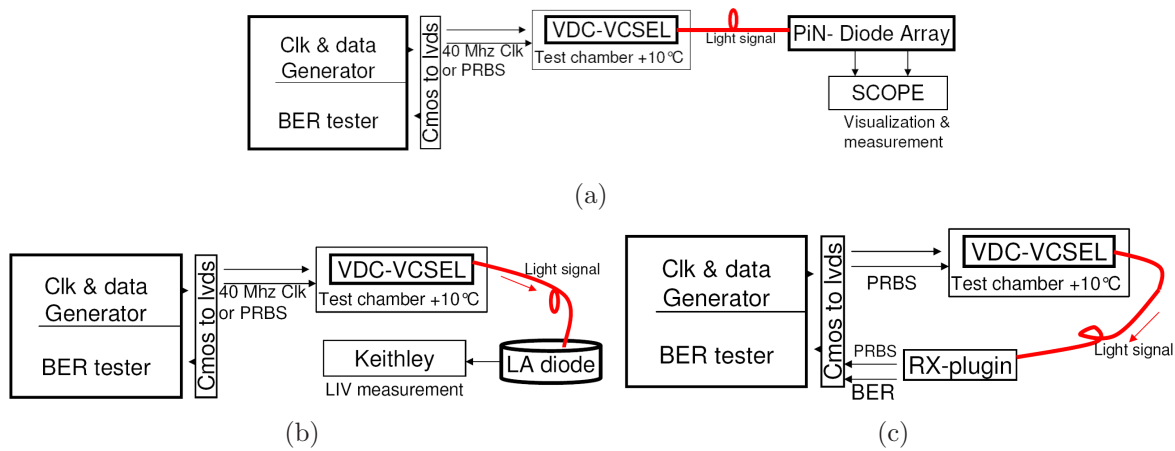


Figure 5.18: *The sub setups utilized for VCSEL signal characterization. Three modes are shown: A mode to measure light signal amplitude using the PiN diode array hence visualizing the waveform (a) an Light current and voltage characterization set up set up with the large surface area diode read out by a Keithley source and measuring meter (b) and a BER set up (c).*

The sub set up developed to achieve this is shown in Figure 5.18. The measurements were done at setting of $I_{Set}=1.1$ mA for the 7 links boards and $I_{Set}=2.2$ mA for the 14 links boards.

The procedure was have a bit error check for 30 sec with a PRBS signal then send a 40 MHz clock LVDS signal through the data link channels. Using a PiN diode (calibrated) current signal visualized on the scope to ensure that all channels have a proper waveform and then measure the signal amplitude. The VCSEL L-I-V characteristics was done by varying the V_{set} setting from 0 V to 1.5 V at 0.03 V step sizes.

The optical power distribution at 24°C NTC (10°C chamber temperature) is shown in Figure 5.19

5.10.5 The Optical Characterization at optoboard -10 °C

During the functionality checking at -10 °C at the thermal cycling phase optical power was observed to reduce in amplitude. At Wuppertal it was observed that for some opto-board channels power amplitude reduced as a result of temperature change in the test chamber. Some channels that had normal power amplitude during the burn in at 50°C were observed to reduce in optical power to what may be considered as very low values as indicated to the reduction of the level viewed on the scope. In this assessment 15 opto-boards were found to have channels with reduced optical power values and 5 had almost no light. A measurement from Ohio and analyzed here reveals that some opto-boards drastically reduced in optical power. This can be seen in Figure 5.20

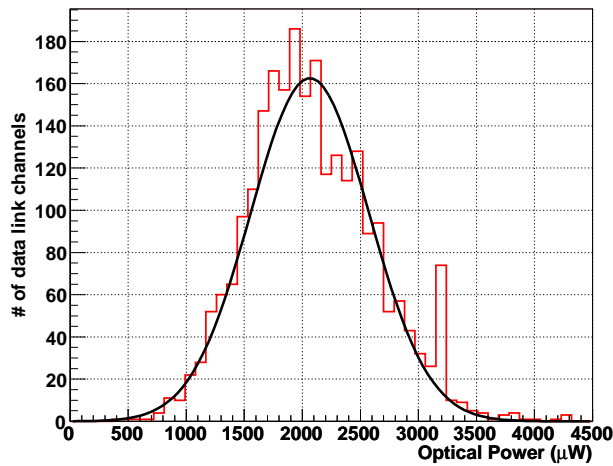


Figure 5.19: *The optical power at the nominal setting of 0.9 V ($I_{set}=0.56$ mA per VDC chip) for all the production boards measured at OSU and at Wuppertal. The average power is 2.084 ± 0.5 mW. The Q/A cut is power more than 0.5 mW.*

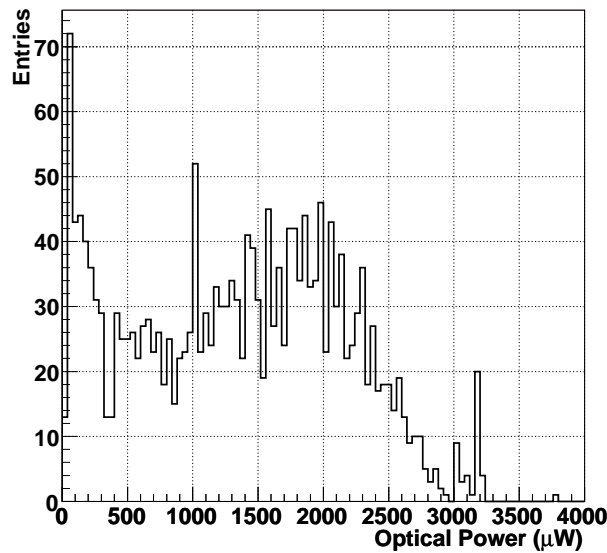


Figure 5.20: *The optical power at the nominal setting of 0.9 V ($I_{set}=0.56$ mA per VDC chip) at -10°C for the opto-board measured at OSU but analyzed within the scope of this work. The optopower was found to reduce drastically on boards that measured normal power at $+24^\circ\text{C}$ and $+50^\circ\text{C}$.*

This may largely affect the read out at since it is foreseen to have the detector end elec-

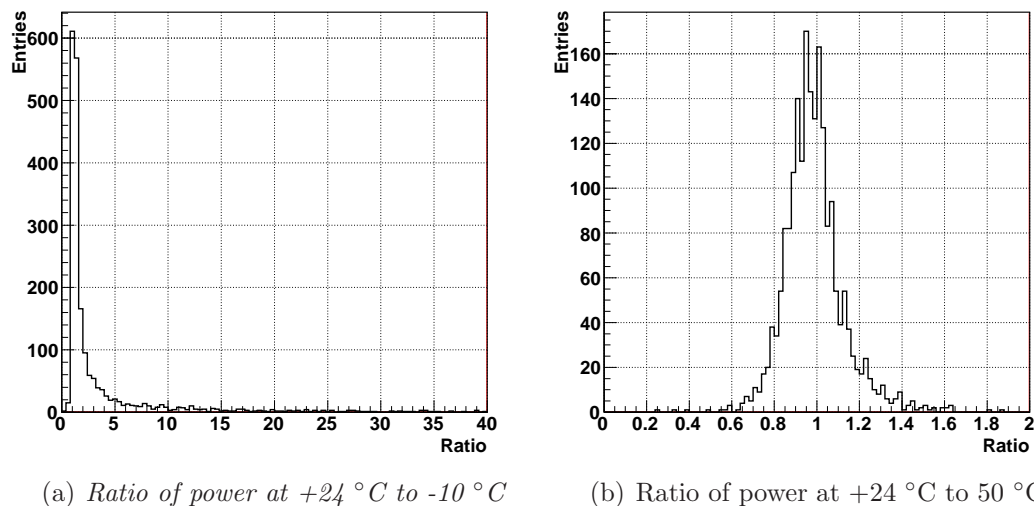


Figure 5.21: *The optical power ratios at $-10\text{ }^{\circ}\text{C}$ and $+50\text{ }^{\circ}\text{C}$ to power at $+24\text{ }^{\circ}\text{C}$. The optical power dropped drastically at $-10\text{ }^{\circ}\text{C}$.*

tronics be cooled to temperatures upto $-30\text{ }^{\circ}\text{C}$. Further studies are going on on this issue to see how best to have the opto-board operate within the temperature range that does not affect their functionality. At $-25\text{ }^{\circ}\text{C}$ opto-board ambient temperature the temperature is approximately $-10\text{ }^{\circ}\text{C}$, the temperature values where optical power of some boards decrease largely as shown in Figure 5.21. This suggests that they ought to be operated at a higher temperature.

5.10.6 The Optical Power Measurement at Saturation

An optical power measurement was done on the production opto-boards at Wuppertal at the saturation region. This was to determine the general spread of power at saturation. Figure 5.22 shows this distribution. At saturation the characteristics of the optical output is demonstrated by the board with the highest spread at saturation which is shown in Figure 5.23. It can also be observed that at this region the optical power fluctuates in addition to spreading. For this reason the saturation region will not be utilized as a usable setting.

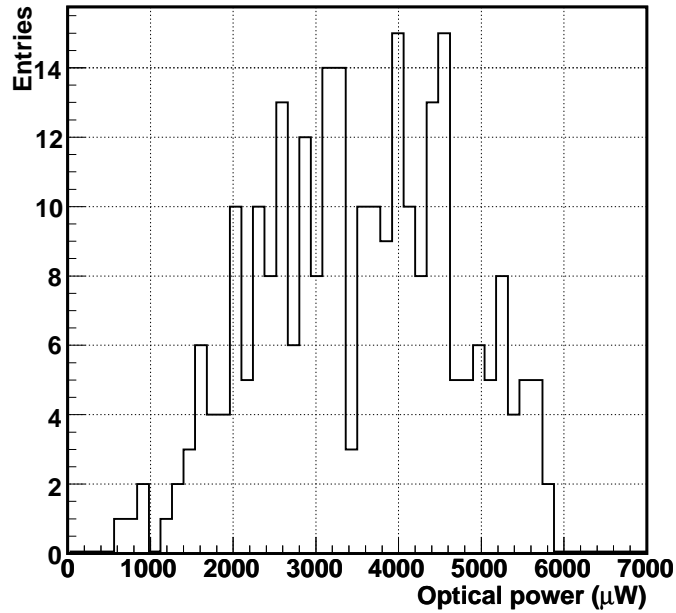


Figure 5.22: *The optical power at the saturation region defined by $V_{Iset}=1.2$ V for the production opto-board measured at Wuppertal.*

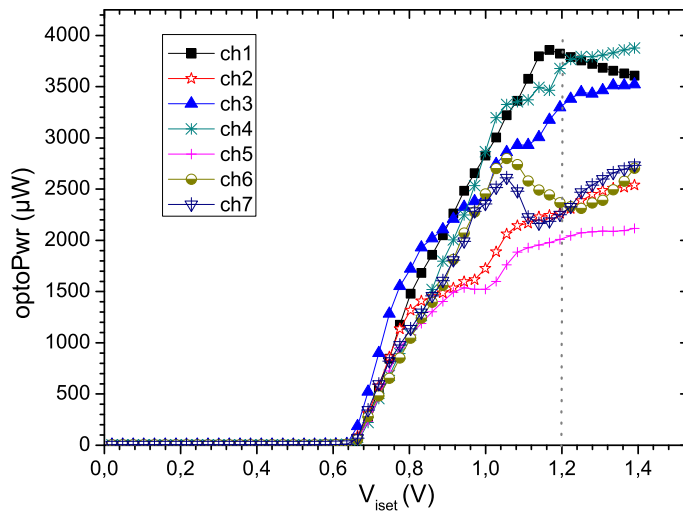


Figure 5.23: *The optical power at $V_{Iset}=1.2$ V for one of the production opto-board with the highest spread at saturation and at the working region of $V_{Iset}=0.9$ V . Optical power fluctuations can be observed in addition to spreading.*

5.11 Conclusion

From the production measurements the TTC links on the opto-board showed no functionality problem observed as compared to the data links. In the Table 5.4 below a summary is given of the optoboard yield ^k at Siegen/Wuppertal and at Ohio State University during the burn-in, thermal cycling and complete Q/A phases.

Testing site	Tested Boards	Failed Boards
Siegen/Wuppertal	75	8
OSU	186	4

Table 5.4: *Opto-board production yield during the burn-in, thermal cycling and the complete Q/A phases.*

For the Siegen/Wuppertal batch only one board failed due to a faulty TTC link. During the burn-in phase 6 opto-boards failed the Q/A with a VCSEL problem. This problem was concluded from the opto-board current consumption fluctuations of more than 7 mA in deviation from their mean consumption current and without optical power out of the VCSELs. Two more opto-boards had the VCSELs loose the light signal after a time lapse from the final Q/A. This makes a total of 8 opto-boards from the production lot at Siegen/Wuppertal with problems associated with the VCSEL. Similar problem was reported at OSU for 4 opto-boards. This problem is associated with the increased VCSEL serial has been thoroughly investigated during pre-mount measurements at CERN and there is a clear understanding of how to identify good opto-boards to be used on the detector [47]. In addition to the serial resistance, is a problem of the optical power depending on temperature as it has been shown. A solution to implement “heaters” by resistors to keep the opto-board at working temperatures independent of the ambient detector temperature is being investigated at CERN. Opto boards with optical power to temperature dependence problem have been found to turn on slowly when transmitting data. This problem has also been understood [47]. Generally all the opto-boards are undergoing pre-mount retesting. This re-testing has increased the confidence level on the opto-boards to be mounted on to the detector. To compensate for the shortages caused, more opto-boards are being produced at OSU.

^kOnly the yield by the time of compilation of this thesis is considered. The optoboard production was carried further on at Ohio State University. Further testing was done at CERN necessitated by VCSEL failure problems with time. Thus updated yield can be followed up from the Pixel Optolink wiki page and OSU production page [49, 50]

Chapter 6

The Optical Power Calculation

It is required that the optical signals transmitted through the link maintain a functional quality for the 10 years of operation. This feasibility must be understood beforehand. The optolink ought to have a bit error rate not greater than 10^{-12} [51] by the end of its usage. Irradiation and attenuation effects cause a percentage loss in signal properties that can lead to data loss during transmission. It is important to understand the significance level of these effects. A simulation of the optical link is motivated by the need to study the parameter space while irradiation and attenuation factors are taken into account. The observations made during the developmental and production measurements are taken as the basis of the simulation and the probability distributions of a successful optical link in relation to the functional parameter space are evaluated.

6.1 The Components in Consideration

The components of the opto-link taken into consideration in this calculation are the TX-plugin and the RX-plugin on the BOC card, the optical fibres and the opto-board. The opto-board has two components, the PiN diode and the VCSEL whose properties are affected by irradiation, hence by a certain percentage, dropping the performance. The RX-plugin and the TX-plugin obviously do not experience any irradiation hence their functionalities are not expected to change with time. This is apart from the normal aging process which is not considered in the simulation. During the normal laboratory tests the optical fibre lengths that has always been in use were arbitrary without any references to the actual lengths to be implemented in the experiment. Thus the production and measurement of the actual fibres together with the connectors provides the distribution of transmission attenuation.

6.2 Calculation Strategy

For this calculation the measurements done during the production of the optolink components is taken as a basis of the calculation and simulation. The key parameters of interest are the optical power, attenuation and irradiation factors of the optical power on the links. As a starting point, the measurements available from the optolink production and from the development process can be divided into: 1) measurements providing values before irradiation and 2) measurements providing values after irradiation.

Values Before Irradiation

The measurements providing values before irradiation include:

1. The production measurements result of the distribution of the optical power for all the opto-boards being installed in the detector. The result gives the optical power signal amplitude at the nominal detector operation power setting before irradiation and transmission attenuation.
2. The production result from the power signal amplitude from all the TX-plugin's that are to be mounted on the BoC cards. The result gives the distribution of the optical power at the nominal and the maximum setting before transmission.
3. The production result of the responsivities of the PiN diodes that were mounted on the production opto-boards and on the RX-plugins. For the opto-boards, this responsivity result gives the distribution before irradiation.
4. The resulting distribution of attenuation measurement done on all the fibres produced for the optical link.

Values After Irradiation

The measurements providing values after irradiation include:

1. The VCSEL optical power distribution results from irradiated production opto-board prototypes. The power result obtained is without transmission attenuation. By irradiating the opto-board prototypes, further measurement distributions of the DORIC PiN current threshold under irradiation and irradiated PiN responsivities were obtained.
2. The irradiation attenuation result from studies done on the fibre prototypes that were produced for the optolink.

In addition to the above mentioned, there is data for transmission signal working range and the range of parameters for which the data signal can be accommodated at the optolink's receiving end at the BOC card, and be recognized for correct reconstruction at

the readout out driver. The fact that all these measurements of properties do not give a single number rather they do present a distribution of parameters that issue to best and worst cases necessitates that there be a calculation in order to know the limits.

The data sets were fitted with functions that objectify the components. Each data set has been fitted with best describing function in relation to the qualification limits. The gauss fit and the Weibull^a function has been utilized most. The Weibull is given by:

$$f(x) = \frac{\gamma}{\alpha} \left(\frac{x - \mu}{\alpha} \right)^{\gamma-1} e^{-\left(\frac{x-\mu}{\alpha}\right)^\gamma} \quad x \geq \mu; \gamma, \alpha > 0 \quad (6.1)$$

Where γ is the shape parameter, μ is the location parameter and the α is the scale parameter. The Weibull function has been chosen as the most appropriate function to show qualification cuts on data sets. The cuts are determined by the qualification specifications. The data set, for example of the optical power at a single setting is best described by a gauss fit as it is expected that the distribution ought to show a deviation from the mean value as all should have the same output of power. But there is a spread of this parameter that is characteristic of the VCSEL channel slight differences.

By the deduced functions, one is able to not only calculate the optical link functionality limits, especially after irradiation, but also to study the probable distributions of the qualities at various settings, leading to a better understanding of the link's functionality in all likely conditions that may appear: something a lab setup measurement cannot achieve. Furthermore the calculated parameters will be implemented in a running system so as to learn by data the characteristics. One is able to know the limits of the optical link settings and this will help to guide during detector operations.

The Calculation Method

To calculate, the distributions objectifying the components are combined as they appear on the pixel detector optical link. Since the Data link and the TTC link are decoupled, they are treated separately. The Data link's calculation starting point is the optoboard and that of the TTC link is the TX-plugin. The various scenarios are calculated by considering step by step, the single components of the link. For the data link, the optical signal before irradiation is calculated by folding the distribution of the measured optical power to the measured attenuation factors. Then the result is folded into the PiN responsivity distribution to get the result of the electrical signal reaching the RX-plugin. The result is then compared to the measured working region of the RX-plugin. Similary the optical signal for the irradiated case is calculated by including into the calculation the distributions of the measured optical power loss due to irradiation at the optoboard and the measured attenuation increase factors resulting from irradiated fibers. A similar method was followed to calculate the TTC signal only that the TX-optical power, at BoC cards, off the detector, is not to experience irradiation while the PiN diodes on the optoboards will experience irradiation. Thus the PiN responsivity of the optoboard PiNs is reduced due to irradiation as shown by measurements. This final result of the TTC

^aA probability distribution function

signal is then compared to the measured and known working limits of the TTC link at the opto-board. The worst case scenarios are also evaluated by considering the tails of the distributions having the worst case numbers thus enabling the evaluation of the links limits on an event of a worst case scenario. For example, it can occur that a channel with low optical signal couples to a highly attenuating fiber channel after irradiation. Then it profits to know whether such a channel can still work when the result is compared to the link's working region at the RX-plugin for the data link or when compared to the opto-board's Doric-PiN threshold for the TTC links.

6.3 Attenuation and Irradiation Effects

As previously mentioned, the optical signal is subject to attenuation resulting from the fibre length and the light coupling from connector to connector. There is also the loss of signal amplitude due to the degradation resulting from the irradiation of the VCSEL on the opto-board for the data link and the drop in responsivity of the PiN diode for the TTC link. There is loss of power in both cases as mentioned in Section 4.5.1 of chapter 4. In the following section the attenuation before and after irradiation is evaluated.

Attenuation Before Irradiation

Attenuation before irradiation is only due to the optical fibres length and coupling at the connectors. The production of the single radiation hard SIMM fibres was done by Fujikura^b, while the production of the single GRIN fibres was done by Draka.^c The ribbonising and splicing was done by Ericsson^d while connector production and attachment onto fibres and all testing and measurements was done by Diamond^e. These measurements were analyzed in this work. The distribution of the measured attenuation of the TTC-links and data-links optical cables is shown in Figure 6.1 while that of the short optical cables between PP1 and PP0 is shown in Figure 6.2.

The minimum attenuation values of the fibers can be observed from the distribution (≈ -2 dB for TTC fibres, ≈ -1 dB for data fibres, and ≈ -0.1 dB for the PP0 to PP1 fibres). The attenuation cannot be less than these limit values and hence, a distribution is observed where the slope at the left is sharply rising, while it slowly falls to right after the peak value as the attenuation becomes higher. This kind of distribution is well described by a Weibull distribution function. For the PP0 to PP1 fibres it was better described by two gauss, that is, one fitting the sharp peak and the other broad distribution to the right. There were a few fibres showing almost no attenuation probably due good connector coupling.

From the specifications the maximum value of attenuation before irradiation is -3.5 dB for the TTC links, -2.5 dB for the data links, and -1.0 dB for the PP0 to PP1 for all links. The

^bFujikura Ltd. Investor Relations Group wwwadmin@fujikura.co.jp

^cDraka Holding, Netherlands

^dEricsson Optical Networks Products

^eDiamond Company: Contracted to fabricate fibers

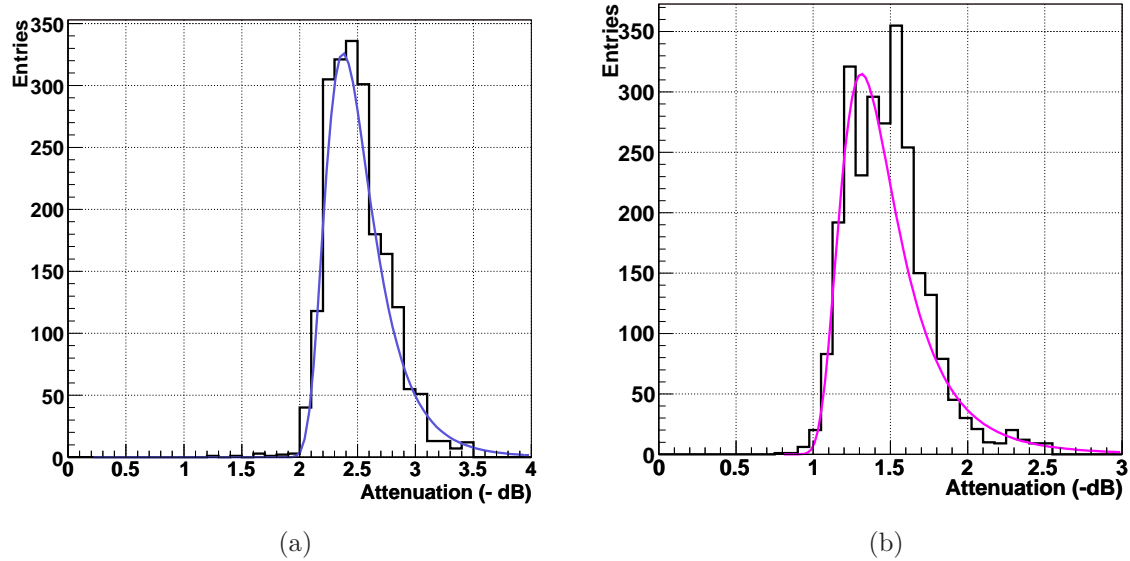


Figure 6.1: *Measured and fitted attenuation for TTC (a) and data (b) fibre cables. The mean attenuation is -2.5 ± 0.26 dB and -1.5 ± 0.26 dB respectively*

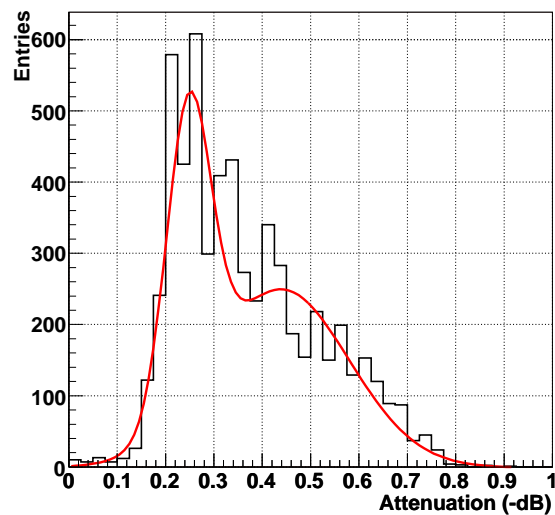


Figure 6.2: *Measured and fitted attenuation for PP0 to PP1 fibre cables. The mean attenuation is -0.37 ± 0.15 dB.*

measured values show that all meet the qualification specification. The attenuation values after irradiation have to be evaluated by simulation using the attenuation distributions in Figures 6.1 and 6.2.

Attenuation due irradiation

To calculate the attenuation due to irradiation, the worst case levels of irradiation after the high luminosity phase of the detector operation are used. These are the same values used to qualify the radiation hardness of the optical fibres [44]. The irradiation values in the region where the optolink components are located is shown in Table 6.1, while the corresponding resulting attenuation values are shown in Table 6.2. The irradiation values shown quickly fall off along the fibre path but to provide safety margins, these values were used.

	Pixel	SCT	Calorimeter	Muon
Ionizing dose kGy(Si)	500	100	0.8	0.01
neutron fluence $n(\times 10^{14}\text{MeV Si})/\text{cm}^2$	10	2	0.2	-
Neutron flux $(\times 10^9 n(1 \text{ MeV}(\text{Si}))/\text{cm}^2/\text{hr})$	180	9	0.7	-

Table 6.1: *The irradiation levels to which the on-detector fibres are assumed to be exposed. Shown are the worst case ionisation doses, neutron fluences and fluxes after 10 years of LHC operation for the ATLAS inner detectors and electromagnetic calorimeter [44]. The level at Muon chambers is insignificantly low due to effective shielding.*

level	Pixel	SCT	Calorimeter	Muon
gamma	<-0.1 dB/m	-0.047 dB/m	$-1.2e^{-4}$ dB/m	$-1.6e^{-6}$ dB/m (GRIN: -0.025 db/m)
neutrons	-0.003 dB/m	-0.0003 dB/m	≈ 0	0

Table 6.2: *The attenuation values due to irradiation on the SIMM fibre. These are worst case levels to cater for safety margins. The GRIN fibre is assumed to experience only irradiation that is for the Muon level. The “level” here indicates the distance from the interaction point defined by where these regions are in the detector [44, 45].*

To calculate the attenuation due to irradiation, the first 30 m of the optical fibre is taken into account. Within this 30 m is the first 10 m for which the radiation hard SIMM fibre is utilized^f. This fibre is exposed to the radiation contribution of the levels at SCT, calorimeter and the Muon areas: The corresponding attenuation values are shown in Table 6.2. The GRIN fibre is assumed to experience irradiation of the muon level only for 20m. Attenuation of the GRIN fibre due to neutron irradiation at the Muon level is -0.025 dB/m.

These values of attenuation by irradiation on the fibre are implemented in the calculation as a non distributed number. The understanding is that the irradiation value can be

^fthe actual lenth of PP0 to PP1 fibres is 6.8+2.26/2.51 m since there are two lengths as shown in Figure 4.15 of section 4.6.1 in chapter 4 but 10.0 m is taken on average since there is also the splicing. However these differences in lengths are short and insignificant

precisely determined according to distance from the interaction point. The values of irradiation expected have been calculated and documented [44,45]. The worst case values have been chosen to allow safety margins.

6.3.1 Total Attenuation

Total attenuation is evaluated for irradiated and non-irradiated case. Before irradiation, attenuation is only due to the fibre length and connectors as shown in Figures 6.1 and 6.2. After irradiation the attenuation is due to irradiation of the optical fibres in addition to the fibre-length and connection attenuation. Therefore the total attenuation for both data and TTC lines before and after irradiation is shown in Figure 6.4 and 6.3. This total distribution shows a probable attenuation of up to -5 dB for the total TTC transmission and up to -4.5 dB for the total data transmission. The actual meaning of these factors will be better understood when evaluated in relation to the optical signal discussed in the next sections. The main concern would be factors at the tails defined by $\geq(-3.5)$ dB from the data line total attenuation plot and $\geq(-4)$ dB from the TTC line total attenuation plot since these are the factors that can contribute to attenuation of the optical signal amplitude to a level restricted by working limits.

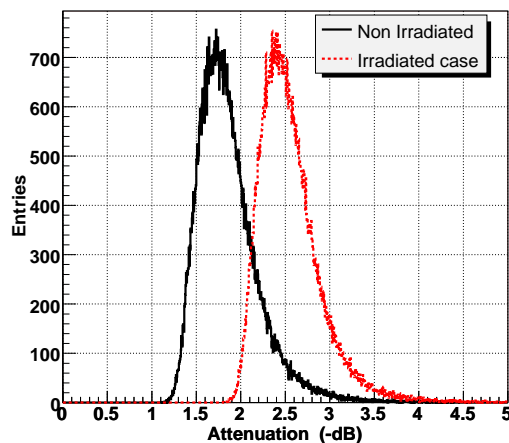


Figure 6.3: *The total attenuation of the data lines. The attenuation increases from -1.855 ± 0.34 dB to -2.545 ± 0.34 dB due to irradiation*

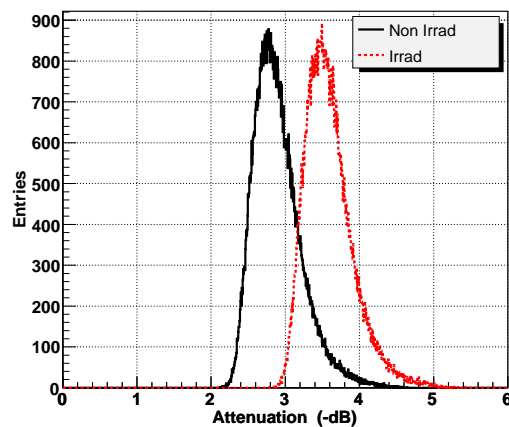
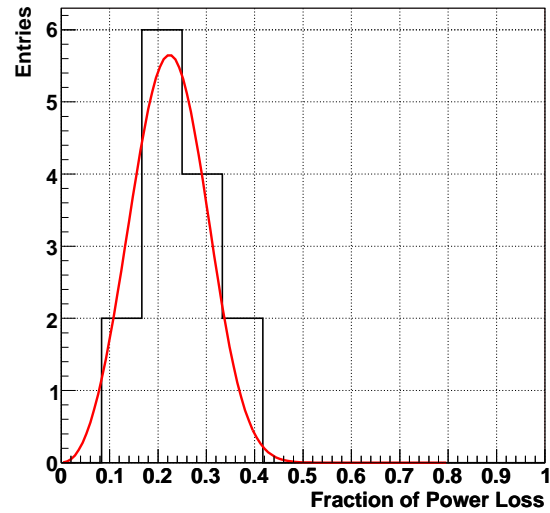


Figure 6.4: *Total attenuation of the TTC lines. The attenuation increases from -2.894 ± 0.32 dB to -3.592 ± 0.34 dB due to irradiation.*

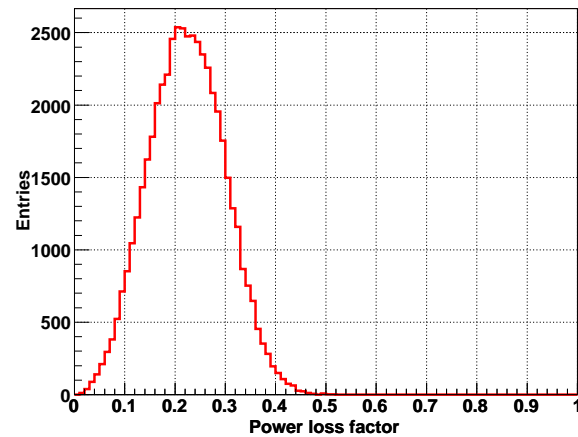
6.4 Power Loss Due to Irradiation

There has been a number of tests for irradiation hardness on the components on the opto-board. Two of the tests were done on the production prototype VCSEL optopackages as they are mounted on the opto-board, one up to 32 MRad and another test up to 50 MRad [38, 39, 40]. Tests on bare optopackages have also been carried out [?]. These

test studies have shown that the opto-board data link output power is lost by a factor ranging between 10% for the least affected channel and 40% for the worst case. Shown in Figure 6.5 are results from the latest study performed on 2 production prototype optoboards, 7 links each. The boards were irradiated with dose up to 50 MRad [40]. On average the optopower will experience a loss of power by $\approx 24\%$. The distribution deduced from these results which is implemented in the simulation is shown in Figure 6.5.



(a)



(b)

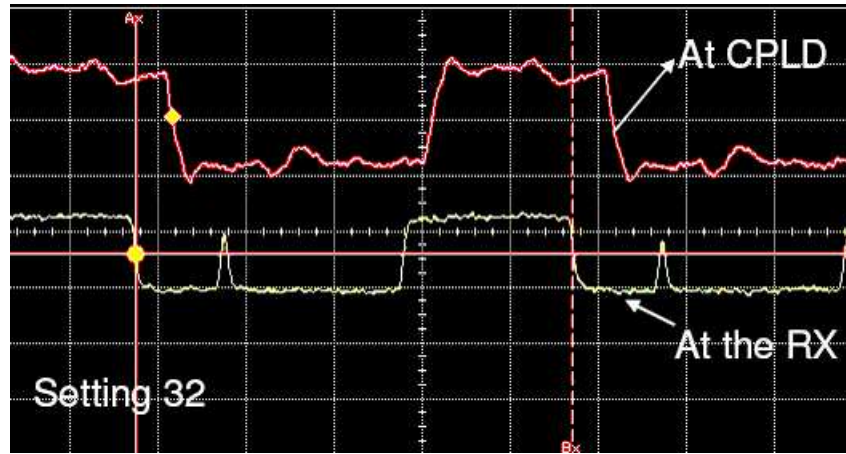
Figure 6.5: *Fraction of power lost by the VCSEL as a result of irradiation on the opto-board with 50 MRad. Figure (a) shows the measured and fitted distribution and figure (b) shows the simulated distribution which has a mean loss factor 0.2346 ± 0.073 .*

6.5 The Data Link Optical Power Calculation

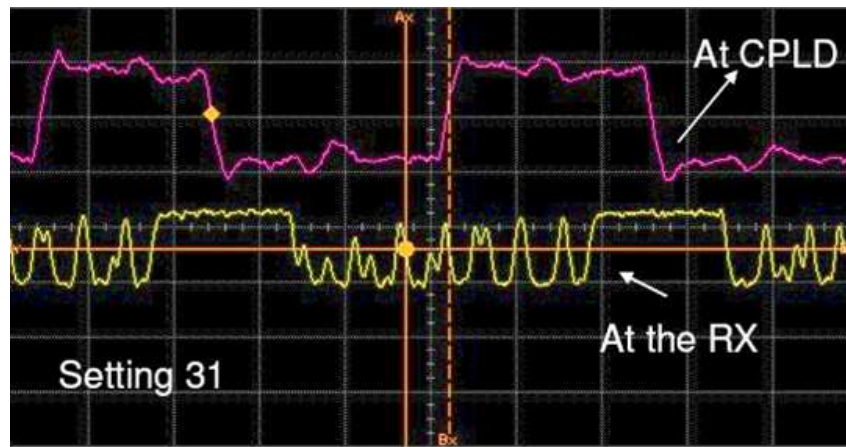
The optimization of the optical signal amplitude settings at the opto-board in view of the receiving side (RX-plugin) settings of threshold with respect to the input PiN current signal after the optical transmission is very important. The signal to be processed at the BOC card ought to have a PiN current signal amplitude above the noise and for which the threshold settings can be set. To get a clean electrical data signal, the settings of threshold must be adjusted per channel. Optimum setting values defined by the RX-plugin threshold and the PiN current must be understood in reference to the range of incoming opto-board power at the PiN.

6.5.1 The RX-plugin Working Range

The incoming light signal to the RX-plugin, which is converted to current, can be recognized by adjusting the registering-threshold between DAC setting 0 to 255. There is a minimum PiN current and a corresponding optimum threshold DAC setting. This optimum DAC threshold setting is the setting that is high enough to blank out the noise. The noise is dependent on the signal amplitude. The higher the amplitude the more the noise in the signal. Thus there is a maximum of the threshold DAC setting for which the noise in the signal cannot be blanked out since the amplitude is too high. The main concern is in the lower region. The upper region is easily avoided by lowering the amplitude of the incoming signal by the V_{Iset} function of the opto-board. This only applies if the opto-board does not have a large spread. The minimum PiN current signal recognizable by the threshold in the case a channel has low optical power must be determined. A measurement shown in Figure 6.6 shows the signal behavior of the PiN current signal at the lower threshold as recognized at the RX-plugin. It is also shown the same signal probed at the CPLD input after being processed by the electronics at the BOC card. The spikes in Figure 6.6(a) in the signal which might mistakenly be recognized as “1’s” are cleaned and the same happens to the case when the threshold is even lowered further causing more spikes as shown in Figure 6.6(b). This indicates that the lower regions of DAC values can be used as a result of this property.



(a) The signal spike cleaned before CPLD chips



(b) More spikes at lower low PiN currents

Figure 6.6: The Logic output signal of the RX-plugin and at the CPLD chips input on the BOC card. It can be observed that the noise effects are “cleaned” before the CPLD’s, where signals are sent to the ROD for reconstruction.

Shown in Figure 6.7 is a plot of duty cycles of a 25 ns pulse against the RX-plugin threshold at certain input PiN current. The duty cycle is measured at the BOC CPLD’s. The nominal duty cycle range for an ideal signal is $50 \pm 4\%$, but it can be observed from the plot that the range of duty cycles for which the signal maintains usable quality is wider than this. This is shown by the measurement points between duty cycles between 10 % and 90 % in the plot. The pulses manifest a short “0” and long “1” or vice versa, but still can be distinguished. It can be observed that PiN current as low as $16 \mu\text{A}$ has a threshold region (≈ 15 threshold DAC steps) meaning such low PiN currents can be used. However for a more stable setting the $35 \mu\text{A}$ setting is used in this calculation as the minimum. A similar observation on the upper regions show that currents as high as $1200 \mu\text{A}$ are acceptable. This gives a working range of $35 \mu\text{A}$ to $\geq 1200 \mu\text{A}$ of amplitude PiN current for which the 40 Mbits/s data mode can utilize. But for the 80 Mbits/s, a

stricter region of less than $\geq 1170 \mu\text{A}$ is required for stability.

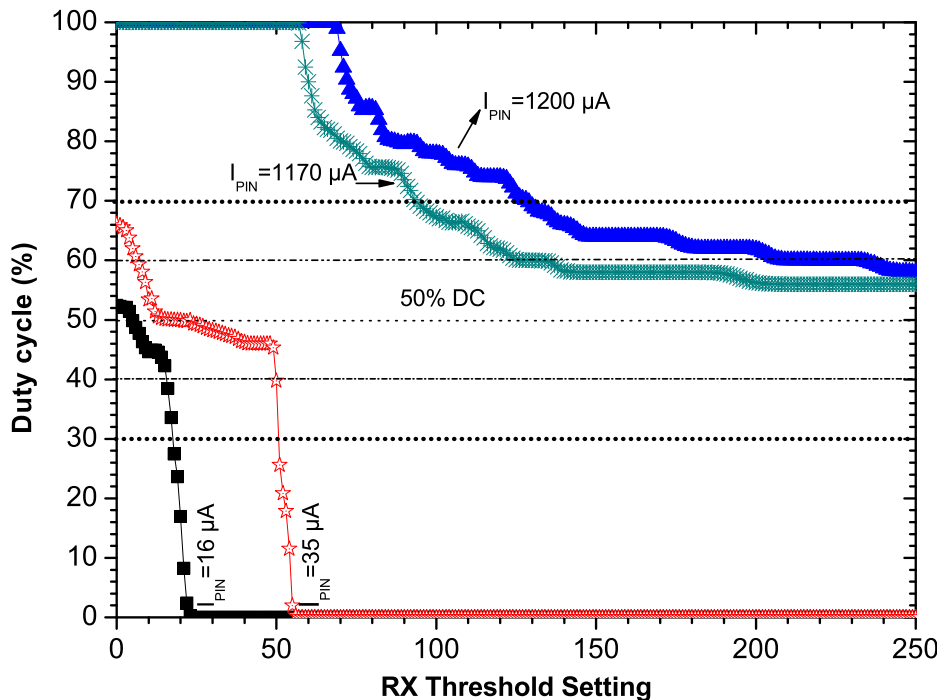


Figure 6.7: *The RX-plugin working range showing duty cycles at low PiN currents and at high PiN currents. A duty cycle range of $50 \pm 20\%$ can be utilized for readout at 40 Mhz. A stricter region of $50 \pm 10\%$ can be utilized for the 80 Mhz mode.*

Next to be considered is the optical power signal reaching the RX-plugin.

6.5.2 The Optical Power

Figure 6.8 shows the measured distribution of the optical power at the nominal $V_{Iset} \approx 0.9 \text{ V}$, measured at the opto-board at 10°C . This distribution is fitted gaussian since what is expected is that the boards should have same power at the same setting, but there are differences varying from channel to channel. This serves as the basis to simulate the optical signal of the data line transmission. Figure 6.9 shows the simulated power output before and after irradiation at the opto-board positioned at PP0 before the 79.2 m fibre transmission. The distribution is chosen at the typical working value of the opto-boards in the test setups in our laboratories, currently at V_{Iset} of 0.9 V. This is also the detector nominal value, however this will vary from board to board as called by the need to optimize the optical power V_{Iset} setting in relation to the RX-plugin working range and data readout. At this value, an approximate 10 mA lasing current is driven through the VCSELs. It is required that there is sufficient light out of the VCSELs on all

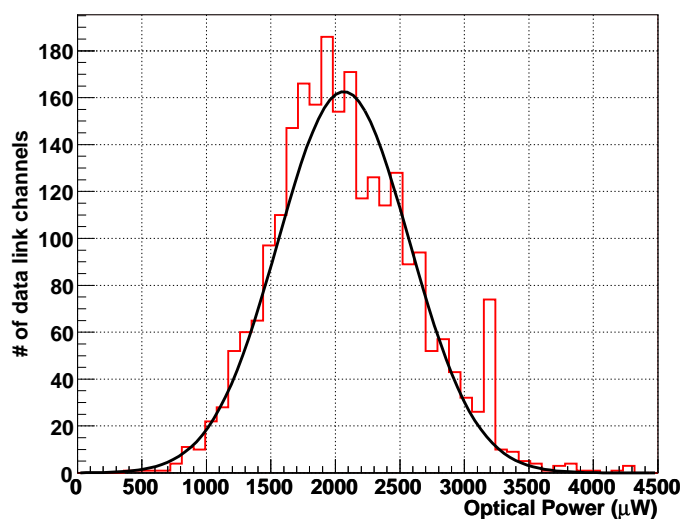


Figure 6.8: *Opto-board power measured during the Q/A data setting of 0.9 V of V_{Iset} measured at 10 °C ambient temperature. The mean optical power is 2.084 ± 0.55 mW.*

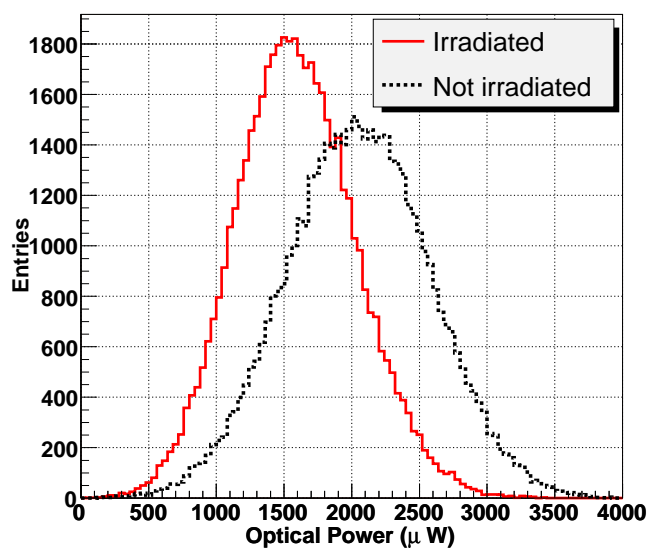


Figure 6.9: *Opto-board power before and after irradiation at setting of 0.9 V of V_{Iset} . The optical power drops from 2.084 ± 0.55 mW to 1.58 ± 0.44 mW after irradiation.*

opto-boards at this setting to survive total attenuation even after irradiation to ensure stable readout. This point is discussed in latter sections.

In Figure 6.10(a) is shown the optical signal after the 79.2m of transmission that is

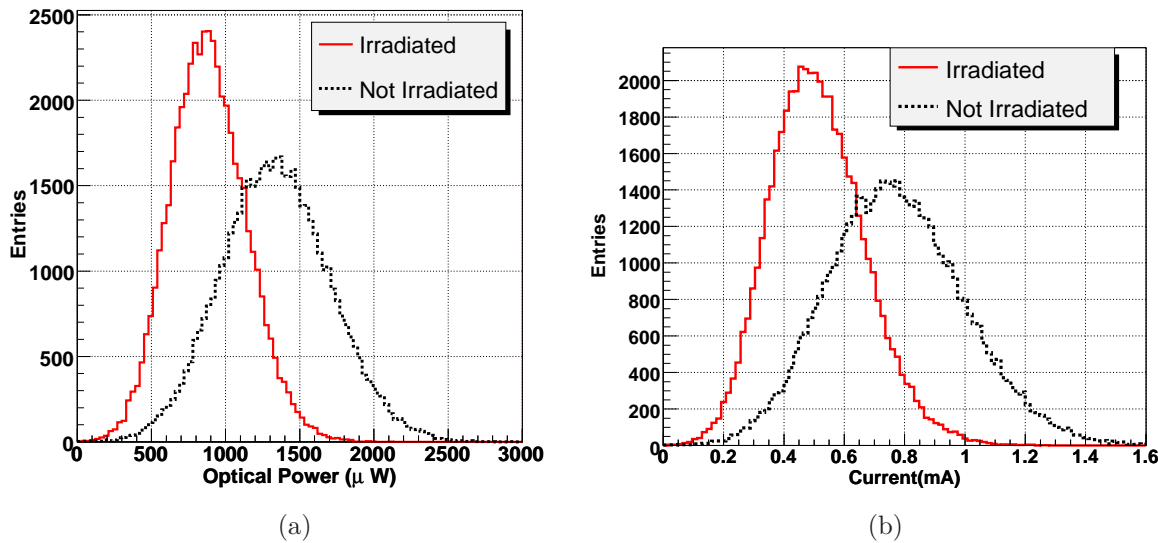


Figure 6.10: *Optical signal into the RX-plugin PiN (a) with mean 1.3 ± 0.36 mW and 0.88 ± 0.25 mW before and after irradiation and the corresponding PiN current signal (b) with mean 0.78 ± 0.36 mA and 0.51 ± 0.25 mA before and after irradiation. The minimum current is $60 \mu\text{A}$ which is above the stable minimum of $35 \mu\text{A}$.*

coupled to the RX-plugin PiN, and 6.10(b) shows the PiN current flowing out of the RX-plugin PiN. The values of the optical signal at the RX-plugin shown here include the transmission attenuation factors shown in Figures 6.5 and 6.3. Before irradiation, the data signal experiences a loss of 35% in amplitude on average. This accounts for attenuation due to fibre and connectors which is the only effect before irradiation. After irradiation it experiences an average drop of 58%. Within the mentioned percentage drop of 58%, about 24% is the irradiation attenuation aspect resulting from the irradiated fibre and irradiated opto-board.

The plots in Figure 6.10 show that at the nominal V_{Iset} of 0.9 V the data signal will survive even after 10 years of irradiation. Test results have shown that the RX-plugin works at minimum value of PiN current of $35 \mu\text{A}$ (See Fig 6.7), which taken as the stable minimum. Furthermore the RX-plugin has shown to work even at $16 \mu\text{A}$ and $22 \mu\text{A}$, though it cannot be considered as a safe margin nevertheless these values of amplitude PiN currents have demonstrated a working such as shown in Figure 6.7 region that can be used.

The few channels that can be at this limit can be rectified by an increase in the V_{Iset} if only they do not belong to a board with a large optical power dispersion. It is therefore necessary not to install opto-boards with large dispersion of optopower. On a general observation the RX-plugin PiN currents of the production opto-boards are well within

the range even when considering an attenuation by probable worst case factors. The worst case factors of attenuation is -5 dB, and in addition, a worst case of 48 % power loss due to an irradiated board.

6.5.3 The Minimum Opto-board Power Required

The minimum optical power required at the opto-board has been calculated. This is done by taking the lowest working range of the RX PiN current of $35 \mu\text{A}$ and calculating it back. This is done in view of two situations: one when optical power is coupled to the normally distributed attenuation and the second case when the power is coupled to a fibre experiencing worst attenuation. The first case gives the view of the minimum optical power needed to be set at the opto-board or the minimum to which they must meet before installation. Figure 6.11 shows that the opto-board ought to have optical power not less than $90 \mu\text{W}$ at the nominal at 10 mA lasing current for the lowest setting. A case where

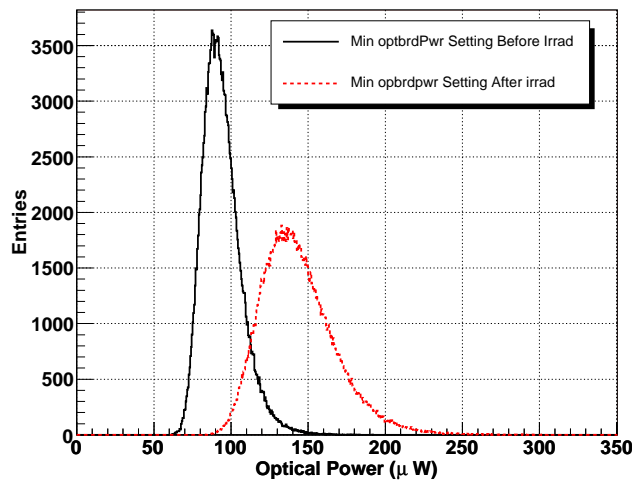


Figure 6.11: *Minimum power at the opto-board needed to meet the minimum RX-plugin working range. An average of $143.84 \pm 12.48 \mu\text{W}$ is required as the minimum setting to have the links work even after irradiation. An average of $94.14 \pm 12.48 \mu\text{W}$ the minimums setting at the beginning before irradiation on average.*

there is a possibility to have the high attenuation as shown by the value at the edges to the right of the distribution shown in Figure 6.3 is studied. An optical power setting of $\geq 370 \mu\text{W}$ is required to survive total attenuation even in case of a coupling to a fibre with high attenuation. The Q/A cut of minimum optical power was $500 \mu\text{W}$ thus even giving a margin of $\approx 130 \mu\text{W}$. However it must be stated that this observation applies for measurements of optical power taken at the temperature of 10°C (opto-board NTC of $\approx 24^\circ\text{C}$). An observation has been made of optical power fluctuations at low temperature as it will be shown and discussed in the next sections.

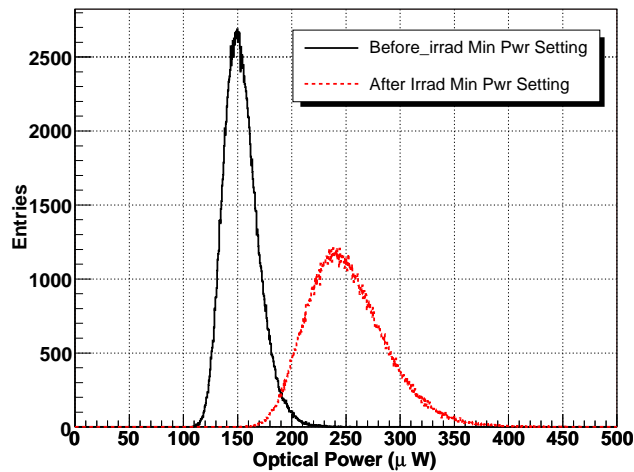


Figure 6.12: *Minimum power at the opto-board needed to meet the minimum RX-plugin working range and at highly attenuated fibre coupling. An average of $153.64 \pm 14.86 \mu W$ is required before irradiation and after irradiation the setting has to be on average $251.7 \pm 17.67 \mu W$ and should not be less than $160 \mu W$. A minimum setting of $400 \mu W$ will ascertain that the links have sufficient optical power even after irradiation.*

6.5.4 Opto-boards with an Optical Power Dispersion

In general power from the VCSEL array do show a power dispersion. The measurements from the opto-board production done at $24^\circ C$ and at $-10^\circ C$ provided the statistics to this observation. Optical power dispersion is as a result of variance in VCSEL array channel to channel characteristics. One V_{Iset} setting controls the opto-board VCSEL array lasing current thus there is no channel to channel adjustment which can reduce the dispersion. Part of measurements done at $-10^\circ C$ reveal that there are temperature dependences. The observation is that, at $-10^\circ C$ opto-board power dispersion increases by reason of some channels of the same opto-board reducing the optical power output. Thus, reviewed in the next section is the optical power dispersion at $24^\circ C$ and at $-10^\circ C$.

Dispersion at $24^\circ C$

The channels of the same opto-board showed a maximum to minimum ratio (referred here as dispersion factor) of optical power as shown in figure 6.13 for optical power measured at $24^\circ C$. Optical power of normally distributed opto-board should have optical power dispersion within 20% corresponding to a factor of 1.3 in dispersion. Figure 6.13 shows that the measured optical power dispersion ratios (Max/Min) had cases with dispersion factor ≥ 4.5 .

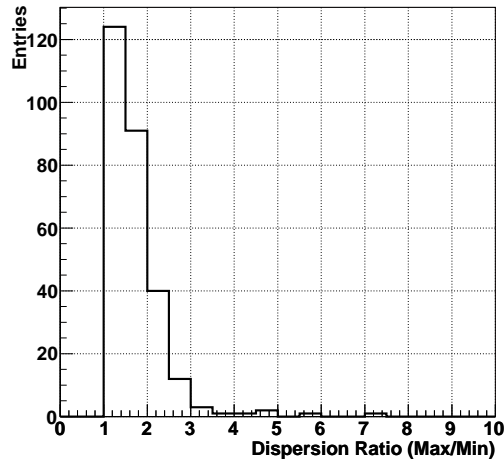


Figure 6.13: *Optical Power dispersion* The distribution of maximum to minimum ratios for 276 production boards. Five optoboards are above the limit of 4.5 in Max to min ratio.

One can relate the PiN current shown in Figure 6.10(b) and these dispersion factors with the RX-plugin working range in Figure 6.7. Such an inference leads to a conclusion that since the working range of the RX-plugin is $\approx 35 \mu\text{A}$ a stable minimum and a maximum amplitude $\geq 1200 \mu\text{A}$ it is possible to accommodate opto-boards with a large dispersion at 10°C . However since the opto-boards with large power dispersion at 10°C are few they can be excluded from being used. Boards with a dispersion factor ≥ 3.5 are 5 in number.

Dispersion at -10°C

The optical power has been observed to depend on temperature as discussed in section 5.10.5 of chapter 5. A number of opto-board channels have the power output decrease largely at -10°C . Figure 6.14 shows the measured and the calculated power before and after irradiation. It can be seen that there is quite a considerable percentage of the channels that have optical power below the power amplitude of $400 \mu\text{W}$ shown in section 6.5.3. This implies that at low temperature an approximated 30% of the channels of the opto-board cannot be operated. These are channels that yield to a PiN current below the minimum RX-plugin range of $35 \mu\text{A}$ as shown in Figure 6.15.

As shown in Figure 6.16 38 opto-boards out of the 252 opto-boards measured at OSU have the dispersion factor ≥ 10 at -10°C . The difficulty lies with the 8% of the total channels resulting into PiN currents below the stable minimum of $35 \mu\text{A}$ at the RX-plug. Though the RX-plugin can accommodate a wide dynamic range (see Figure 6.7) operating the optoboards at low temperatures is a challenge. However there is a study going on to find a working alternative in order to have the opto-boards operate at favourable higher temperatures [49].

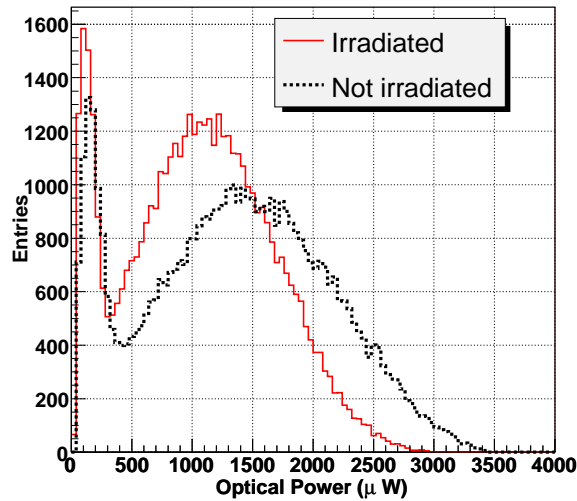


Figure 6.14: *Optoboard power at $\approx -10^\circ\text{C}$ before and after irradiation. Before irradiation the measured mean power is $1.33 \pm 0.7\text{ mW}$. The calculated optical power shows that it will drop to $1.033 \pm 0.6\text{ mW}$ after irradiation.*

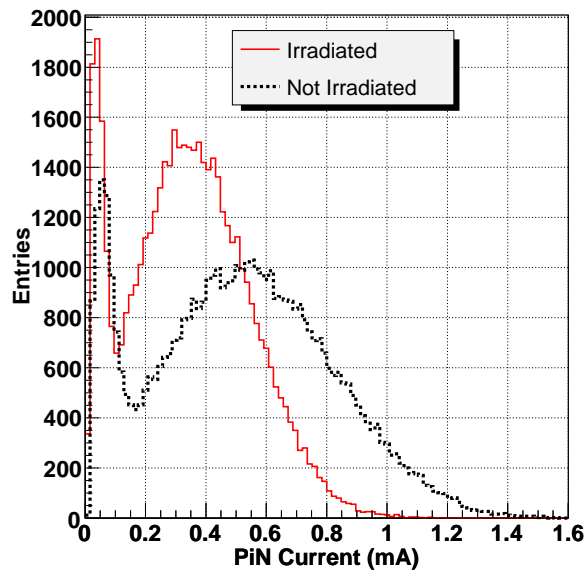


Figure 6.15: *The PiN current at the RX-plugin for optical power influenced by temperature of -10°C on the opto-board. A total of 8% of the channels from the 252 production opto-boards measured at OSU have PiN current below the optimum minimum of $35\ \mu\text{A}$.*

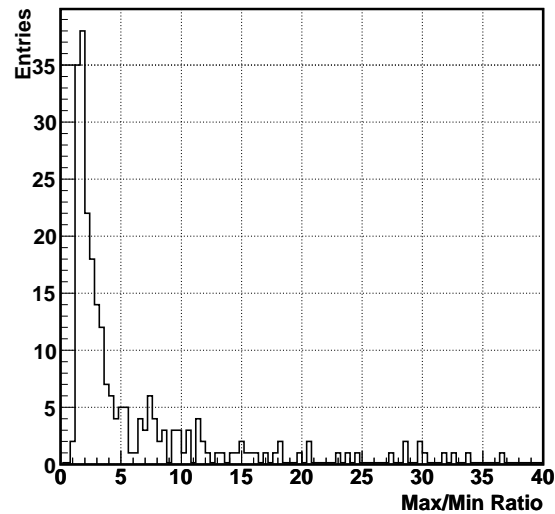


Figure 6.16: *The power spread at approximately -10°C . Power spread on half of the production opto-boards measured at OSU and analyzed here. This demonstrates the difficulty of accommodating the opto-boards at such temperatures for any read out.*

6.6 The TTC Link Optical Power Calculation

The parameters that are of importance to the TTC signal transmission from the BOC card transmitter, TX-plugin are the delay settings, the light amplitude and the mark-space ratio (the duty cycle). These parameters can be set channel wise. The light amplitude directly affects the mark-space ratio settings of the detector clock while the light amplitude out of the VCSELs at the TX-plugin must be optimized to survive the transmission attenuation of the fibres and the connectors, in addition to the requirement that the DORIC must receive a current signal that fits in its working range. This is especially important at the lower threshold. Figure 6.17 shows the measured distribution of the light power at the system working range laser power default settings. Combined two gaussian fit parameters are used to define the simulation function.

The TTC light signal encounters a total attenuation of the TTC transmission shown in Figure 6.4 for both non-irradiated and irradiated cases. Figure 6.18 shows the light signal amplitude before it is coupled to the PiN at the opto-board, that is, at the end of the optical transmission on PP0. One can observe from the three histograms showing the light amplitude before and after irradiation.

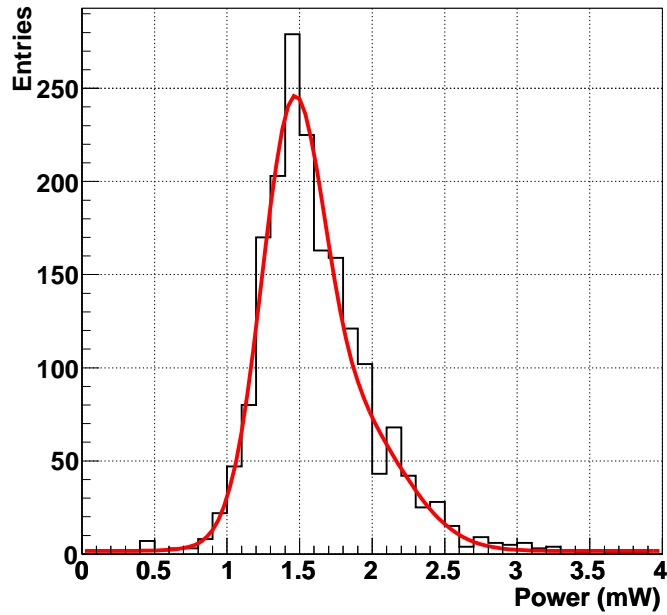


Figure 6.17: Measured optical power at the default RX-plugin settings. The measured mean power is 1.624 mW.

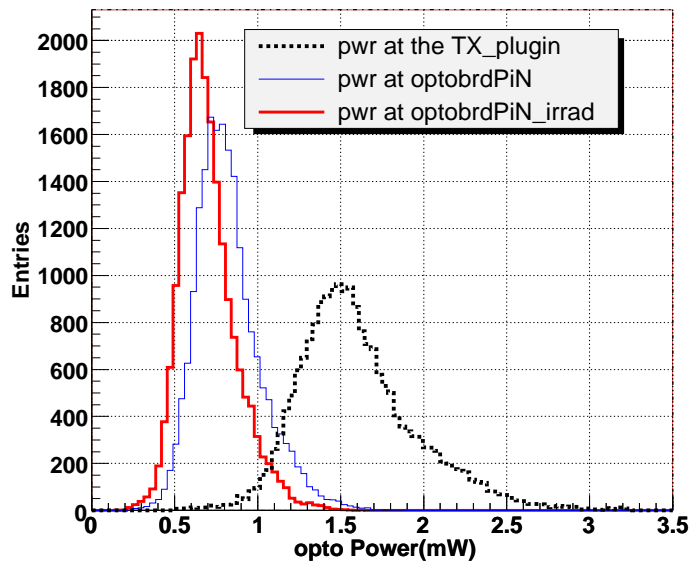


Figure 6.18: Optical signal into the Opto-board PiN diode at the default TX-plugin settings. The power drops by a half, from an average of 1.59 ± 0.36 mW to an average of 0.77 ± 0.17 mW after the irradiation of the fibers.

Figure 6.19 shows the simulated distribution of the opto-board PiN responsivities before and after irradiation. The measured mean responsivity before irradiation is $0.57 \pm 0.059 \frac{A}{W}$, while after irradiating the PiN the responsivity drops by $\approx 55\%$ to $0.33 \pm 0.05 \frac{A}{W}$. The PiN current at the DORIC distribution is shown in Figure 6.20.

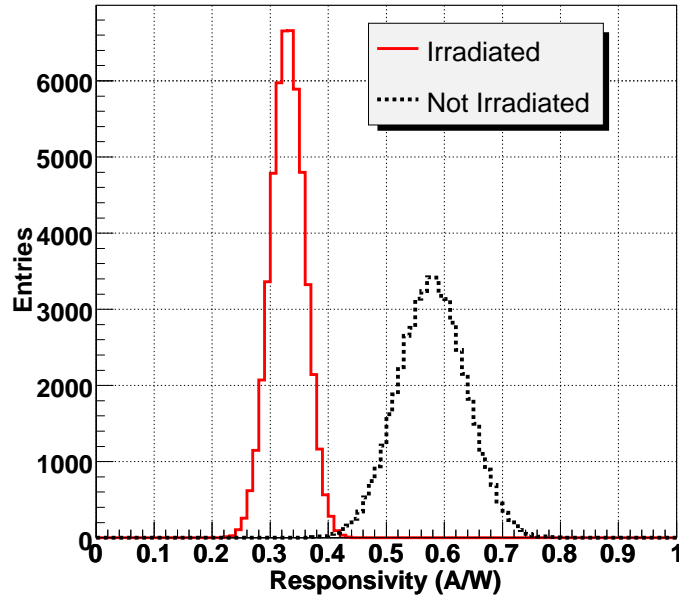


Figure 6.19: *PiN responsivities of the opto-board simulated based on production and irradiation study measurements [38, 39, 40]. The responsivity of an irradiated PiN drops by 55% on average to $0.33 \pm 0.03 \text{ A/W}$.*

Given that the DORIC works even at higher PiN currents than can be delivered by the detector TTC transmission VCSELs, the main point of interest is on the lower threshold. The DORIC threshold for the production opto-boards measured at Siegen and analyzed here show that, the threshold is less than $40 \mu\text{A}$ as shown in Figure 6.21. The thresholds do not change significantly with irradiation and still remain below the $40 \mu\text{A}$ value as has been indicated in Figure 4.11 of Chapter 4.

However, looking into the thresholds margin it can be concluded that the link will eventually have a few channels operating at the limit of $\geq 40 \mu\text{A}$. Operating on maximum laser current DAC settings (setting 0xff) will give higher margin. The adjustment from DAC laser forward current setting of 0xa0 to 0xff of the represent an increase of 55% in optical power shown in Figures 6.22.

From the Figures it can be seen that at the maximal setting there is a $20 \mu\text{A}$ margin between the DORIC lower thresholds of $40 \mu\text{A}$ and the channel with the lowest PiN current ($\approx 60 \mu\text{A}$). From a general observation the TTC link should work to the end of its life, with regard to the optical signal amplitude into the PiN. It has been demonstrated during production measurements that the decoded electrical signals of the 40 MHz clock

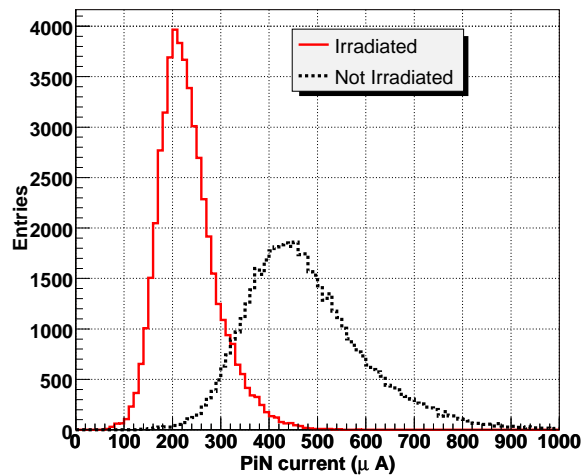


Figure 6.20: *The TTC signal PiN current into the DORIC before and after irradiation for laser DAC setting 0xa0 at the TX-plugin. The current drops from 448 μA to 231 μA after irradiation on average.*

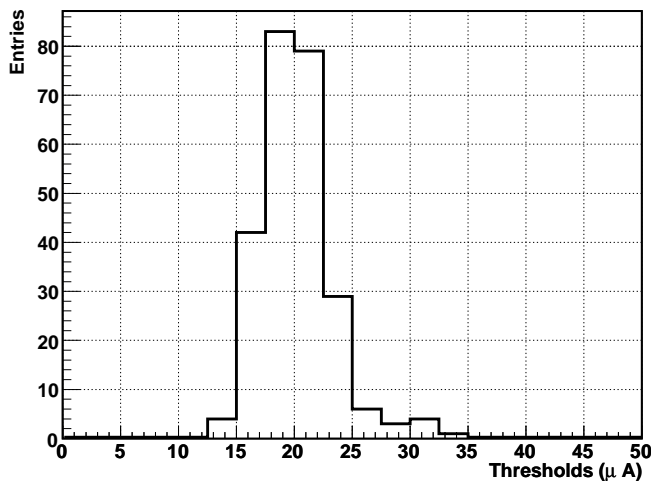


Figure 6.21: *DORIC thresholds, measured at Siegen and analyzed here for this work. The threshold PiN current is below 40 μA .*

and the command signals maintain functional quality at all ranges of DORIC-PiN currents above the lower threshold. This region defined by the 55% increase from laser DAC setting from 0xa0 setting to 0xff can be taken as the lower and the upper limits of the light signal amplitude for which the mark-space ratio and the BPM delay settings must be adapted to. However before irradiation the lower power setting will be utilized so as not to shorten the VCSEL life time due to self heating during the lasing process.

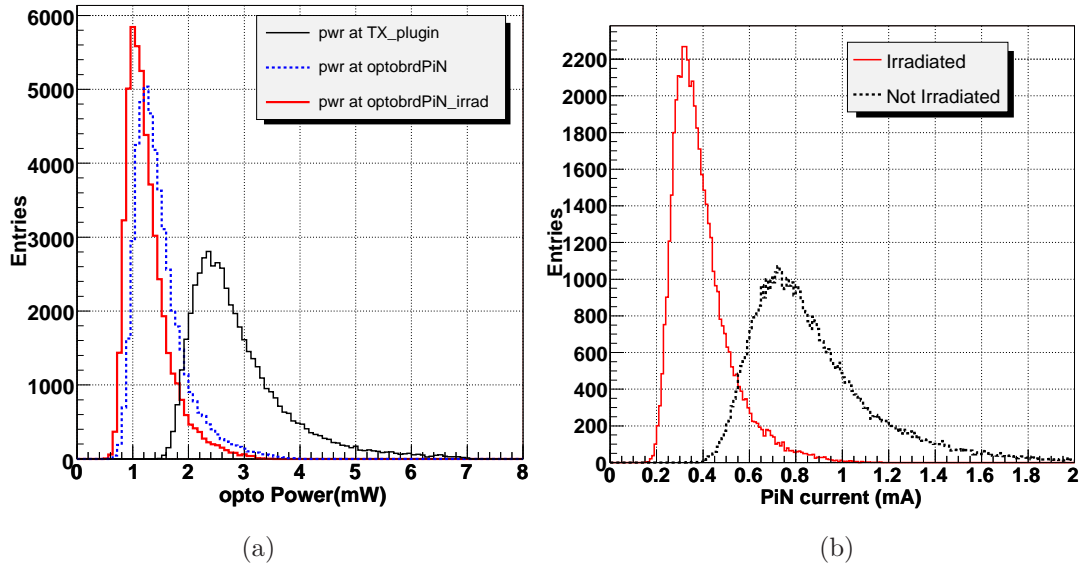


Figure 6.22: *The optical signal into the opto-board PiN (a) and the corresponding PiN current signal for 0xff DAC laser current setting (b). The Amplitude current after irradiation drops from 0.86 mA to 0.41 mA. There is sufficient optical power to operate the TTC links given the minimum PiN current for this setting is not less than 150 μ A as shown in (b).*

6.7 The TTC Limits

The TTC optical power is calculated taking into consideration the link coupling to a fibre with worst attenuation. This worst attenuation value of -5.5 dB is concluded from an attenuation at the edges shown in Figure 6.4 after irradiation. Figure 6.23 shows the minimum optical power needed at the TX-plugin to meet the distribution of the attenuation. Optical power $\geq 400 \mu$ W on average should be sufficient. But to cater for the possibility of a highly attenuated fibre the optical power should be above 540 μ W thus providing a safety margin. This is shown in Figure 6.24. With the best fibre having least attenuation (even after irradiation) 200 μ W at the TX is the limit while with the highest attenuating fibre a minimum of 540 μ W is required. It has been shown that at DAC laser setting of 0xa0, this condition is met. In case of the worst situation as shown in Figure 6.24(b), where minimum currents are nearly 40 μ A, there is a 55 % margin in optical power which can be increased.

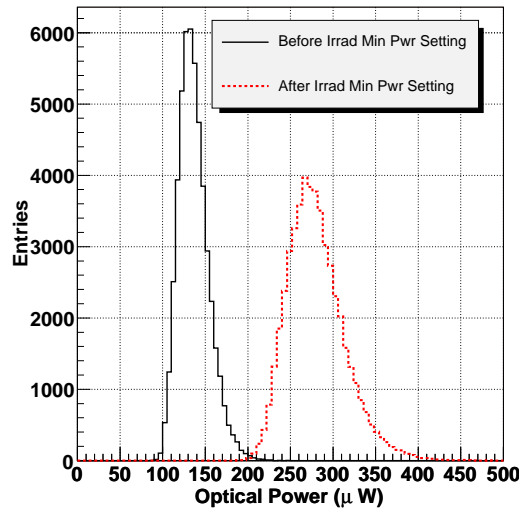


Figure 6.23: *The minimum optical power setting needed at the TX-plugin so as to have the PiN at the DORIC above $40 \mu\text{A}$ considering the “normal” attenuation distribution expected on the TTC links.*

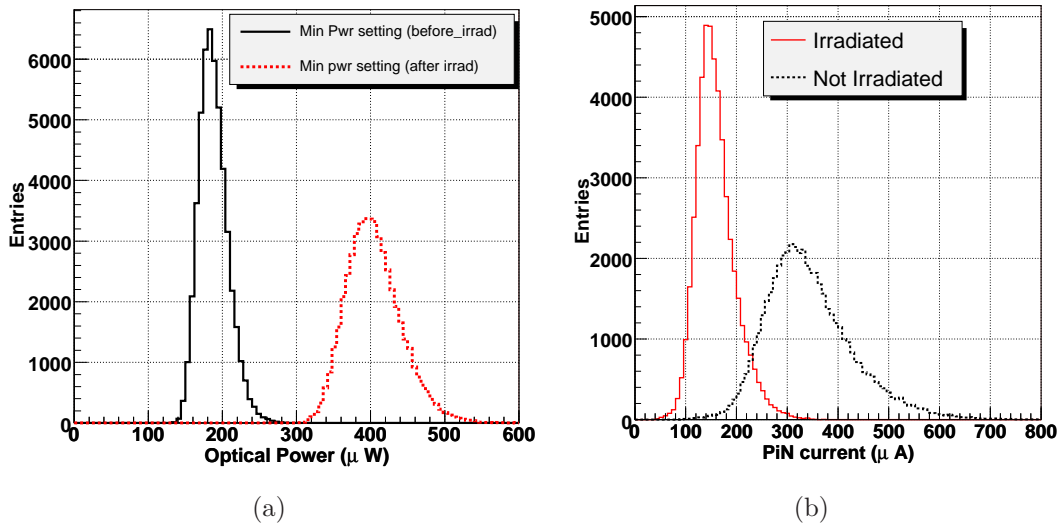


Figure 6.24: *Demonstrating the limits for a highly attenuating fibre. In Figure (a) the minimum optical power output at the TX-plugin required for the links to ensure that all channels have I_{PiN} above $40 \mu\text{A}$ is shown. In this case the optical power from the TX-plugins should not be less than $\approx 540 \mu\text{W}$. Figure (b) Shows the resulting opto-board current at the laser current DAC setting of $0 \times a0$ coupled to the worst possible attenuation in the TTC links.*

6.8 Conclusion

The above optical power calculation demonstrates that the optical link is functional in relation to the optical signal amplitudes delivered at the RX-plugin for the module data and at the opto-board PiN diode for the command signals. The functionality is maintainable even after taking attenuation and irradiation effects into account. However the phenomena where the optical power decreases with temperature for the data links, at -10 °C opto-board NTC, inhibits the link's usage at low temperatures. A solution has to be implemented where the opto-boards will be maintained at an optimum temperature where operation is guaranteed for all the channels.

Chapter 7

Timing Characteristics and Bit Error Rate

Introduction

In this chapter a study is done on the ATLAS Pixel optolink parameters at the BOC card transmitting end, mainly at the TX-plugin and on the receiving end at the RX-plugin in relation to timing properties. This has to do with their interplay with each other during operation and tuning. The main parameters considered in this study are the MSR^a, the BPM fine delay and the laser current setting which are at the TX-plugin and the RX-threshold at the RX-plugin. To study them, the characteristics of the signal duty cycle in relation to these correlative parameters has been done. This is achieved through measurements and enhanced by a simulation study. The measurements used to facilitate the study have been carried out during other ongoing studies related to optolink work [28, 53] and more enhancing measurements carried out within the scope of this work. The measurements are based on the System Test at Wuppertal which has 13 links for measurements. The few measurement points obtained were used to study the characteristics of the mentioned parameters and an extension of the study to a larger system can be done when it is in place at CERN.

Mis-tuned settings of the MSR will affect the TTC signal sent to the module and consequently to the return data path. The MSR is observed to change with laser current setting as shown by measurements. The MSR is also observed to change when the fine delay register is to be set per module. Depending on the degree of mistuning, this will result in fluctuations in the event registration. It can also be observed in not being able to communicate with the modules. Thus the optimized setting in MSR after the desired module timing is set must be maintained. The data link has been discussed in Chapter 6 and hence for this study a working data link is assumed. Conditions affecting the data

^amark to space ratio

link and the way to optimize for a functioning data link have been discussed in previous chapters in relation to the power budget.

In addition a bit error rate measurement based on the System Test has been done and the results will be discussed in this chapter.

7.1 The System Test at Wuppertal

The System Test set up at Wuppertal enables studies and tests of the Pixel read out system components in the laboratory as they function relatedly. The general out look of the System Test is as shown in Figure 7.1.

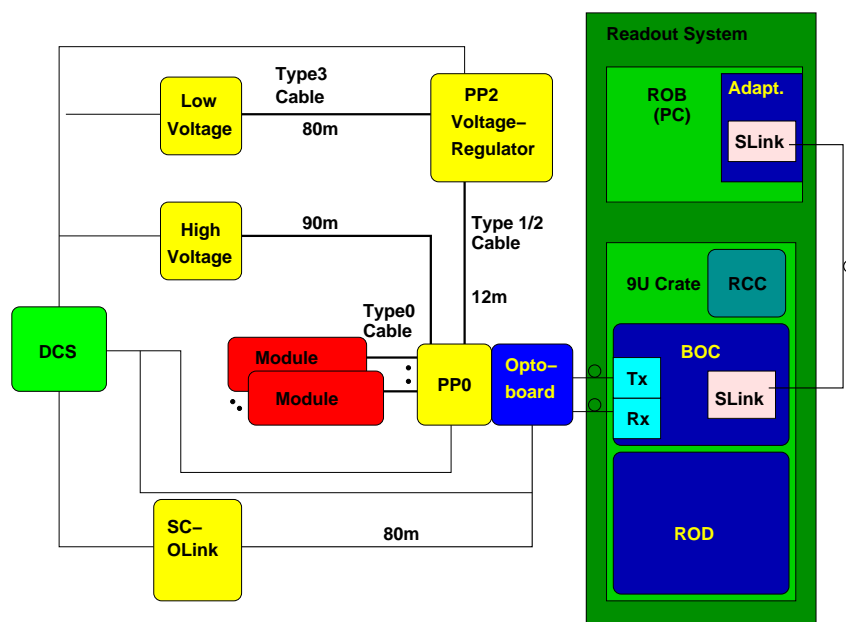


Figure 7.1: *The schematic of a typical System Test. The readout system is shown in green and blue. The yellow parts are the power supplies [52].*

The Wuppertal System Test is composed of: A bi-stave with 26 modules, but only 13 modules (half a bi-stave) are used hence 13 links. Two opto-boards and fibres connecting to a pair of TX-plugin and pair of RX-plugin. A BOC card, a ROD, a single board computer placed in a VME-crate. A control computer and the DCS^b for controlling and monitoring the voltages, currents, and temperatures. An attenuation has been implemented to reflect the actual fibre lengths expected in the experiment. This will be discussed in the latter sections.

^bDetector Control System

7.2 The Parameters Concerned

During an optolink tuning the main parameters concerned in the tuning process are the optical power setting, the MSR and the fine delay which are at the TX-plugin where the BPM TTC signal is sent to the links. These parameters directly affect the on-detector timing. The parameters on the return data path are the V_{Iset} on the opto-board, the RX threshold and the RX-delay at the receiving end and can affect the data sent back from the module. This study is concerned only with the BPM MSR, the BPM fine delay and the laser power setting at the TX-plugin. A mention of the RX threshold in relation to the MSR will also be done. To probe the relatedness of these parameters is important. This was done in the system test by setting the MCC to half clock return and probing by scans at the RX-plugin, the effect on the 25 ns pulse width as the settings are varied.

The MSR sets the signal to 50:50 ratio. This can be set in 32 steps each changing the duty cycle with percent. This has been measured in this study. The laser current setting can be set to a maximum of ≈ 3 mW (DAC setting 0xff) on the links but the working setting is 0xa0, sending ≈ 1.5 mW to the links. The VCSELs are to operate at this setting to avoid aging effects caused by high laser forward currents. There is sufficient optical power to operate the TTC links and with a 55 % space of play as discussed in Chapter 6. To do a fine delay (≈ 0.3 ns steps) the number of inverter gates as the BPM signal passes through are increased and this can distort the signal slightly affecting the MSR. The measurements of this effect will be shown in this chapter. For efficient communication with the module and for efficient data taking process, it has been shown the modules timing will have to be precisely set by the fine delay singly [28].

In Chapter 6 the range and the characteristics of the optical signal of the data transmission link has been shown. Assuming the nominal V_{Iset} setting of 0.9 V and at opto-board NTC of 24 °C there is sufficient optical data signal for the 10 years of operation. Thus in the calculation to be shown here a stable data transmission is assumed with respect to optical power signal. The settings of the opto-board will therefore be kept at this nominal values through out the study in this chapter.

7.3 The General Procedure of the Study

A general procedure for the study is given in this section while the specific steps will be discussed in the latter sections. Measurements have been done in the System Test and the data points have been fitted to get the relations. The measurements involve MCC half clock return scans at the receiving end of the BOC card thus having a complete view of the signal outlook as it passes through the optolink components. The measuring and tuning program tools utilized are developed from another related study [53]. These tools enable scanning stepwise as the MSR and the fine delay registers were varied one a time when the other is set to default. The distribution of the points is deduced and the corresponding describing function chosen. Due to lack of statistics the distribution of the measurement points are an estimate of the larger system. The parameters measured are

the MSR effect on the duty cycle and the fine delay effect on the duty cycle. Therefore the interrelating effect of the MSR on the fine delay and vice versa has been characterized.

The interrelation between the MSR, the fine delay and light power has been measured as well. This was done manually by varying the corresponding setting and recording the PiN currents values of the opto-board. Adjustment of the fine delay and MSR settings will affect the optical power and this result will be shown in this chapter also.

Using the relations a calculation of the optimum MSR has been done, then a delay has been applied and the resulting distributions are shown. Each of these measurement data sets will be discussed in the sections to follow.

7.4 The Tuning Process

During tuning the TX-plugin optopower is set to a certain value. For this study the laser settings were set at 0xa0. A default MSR value of 0x13 is then set, hence the communication can be initiated. The MCCs are set to return the half clock. At the opto-board the V_{Iset} is set to yield PiN currents at the DRX that are within the working range as discussed in Chapter 5. An RX-threshold tuning is then done. During these tests no delay had been applied in the tuning processes within the System Test [53]. The delay settings were set to 0. Thus the working setting for MSR is obtained by requiring that there is a minimal value in the pulse width difference between the two on detector clock modes: The on detector clock is in two modes at a wrong MSR setting, a clock mode with a period longer than 25 ns and another with a period shorter than 25 ns. This is reflected by the half clock sent back by the MCC. This is referred to as the clock hopping mode. This is rectified by MSR adjustments to 25 ns with least jitter (≈ 0.5 ns) at which value, the pulsewidth difference is nearly zero. This effect of MSR on 25 ns pulse can lead to hits registered a clock cycle earlier or later, thus optimizing for the 25 ns pulse is important.

With the real data taking, the fine delay adjustment is will have to be done. Adjusting the fine delay affects MSR. Hence MSR to fine delay looping adjustments are necessary with fine delay setting being fixed by the on detector timing. Thus in this study measuring these magnitudes of interplay is done.

7.5 Expected Effect

After the tuning for detector functionality and data taking are done and optimum settings obtained, later during operation the following scenarios may occur:

1. The degradation of the PiN diode and of the optical fiber will result to reduced PiN currents at the DORIC. As shown in Section 6.7, a highly degraded PiN channel can combine with a highly degraded fibre. This results to PiN amplitude currents that are nearly at the DORIC lower threshold of $40 \mu\text{A}$.

2. Reduced current at the PiN due to attenuation in the links transmission not necessary due to irradiation degradation but loosening connections.

It will then require that there is optical power adjustments at the TTC links by increasing to counter attenuation and degradation. This will be done for a few settings, which distorts the signal duty cycle and consequently the module timing fine settings. It is therefore important, as this study provides, to know the percentages of these effects and whether time settings are precisely retained after any adjustment. In the next sections the measurement on each parameters will be discussed.

7.6 The Mark-Space Ratio

The MSR setting changes the positive pulse width time of the BPM signal sent to the detector. The effect of this setting can be measured at the TX by looking directly to the light signal, at the opto-board by looking at the decoded electrical signal and at the RX-plugin by looking at the returned signal. For tuning purposes and determination of optimum settings looking at the resultant transmitted signal at the BOC card receiving end is the most important measurement. This is because, the signal coming back has the resultant transmission effect of the whole System Test. In Figure 7.2 it is shown a measurement done at the receiving end of the effect of the MSR setting to the on detector clock at two laser DAC settings.

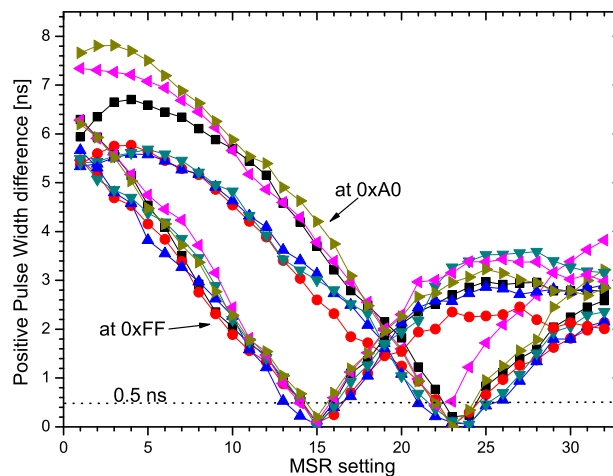


Figure 7.2: *The effect of MSR on the on-detector clock at two TX-plugin laser DAC settings, $0 \times a0$ and $0 \times ff$. The positive clock width difference increases with wrong settings of the MSR. Plotted are the values of the positive clock displacement from the 25 ns pulse. The displacement can be as much as 8 ns. Measurements are shown for the different channels of the TX-plugin differentiated by color.*

Two laser current settings are shown. It can be seen that the difference between the positive pulse width differences of the two pulse widths can be as large as 5 to 8 ns at MSR setting 0 for example. This means there is a difference from channel to channel. The optimal settings of the MSR at DAC laser setting 0xa0 and 0xff at the TX-plugin are 15 and ≈ 23 respectively. The latter has a spread of two MSR settings at the optimal value.

A further study has been done by investigating the magnitude by which the MSR setting changes the 25 ns pulse as seen at return section of the BOC card, the RX-plugin. This was done by changing the MSR register from 0 to 32 in single steps. The fine delay setting was set to zero and the laser setting was at 0xa0. Figure 7.3 shows a result from scans, of this relation between the MSR and the 25 ns pulse change. By this, it is deduced with how much the MSR setting changes the clock positive width, and hence the duty cycle. This is achieved by fitting linear the rising and the corresponding falling edge of the positive width on each of the channels for which the MSR is changed.

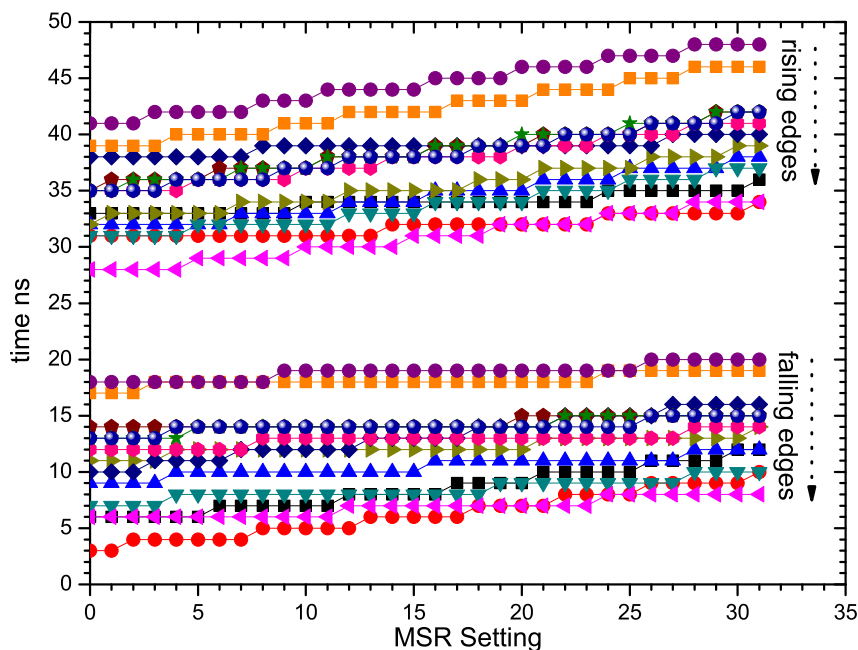


Figure 7.3: *The 25 ns positive width rising and falling edges against the MSR setting. The linear fitting of the edges give the magnitude at which the MSR register changes the positive pulse width.*

The linear fitting of the relation yields values which are distributed with a mean of 0.1486 and a standard deviation of 0.024. From the ratio by which the pulse width changes with the MSR setting, the change in the duty cycle has been calculated using:

$$\text{Change in duty cycle} = \frac{\text{pulse width change with MSR} \times 31}{50 \text{ ns}} \quad (7.1)$$

Where 31 is the full range of the MSR DAC settings. This calculation is for fixed V_{Iset} value and a fixed threshold. It is deduced that the duty cycle change by MSR setting for the two TX-plugins is 9.21 % on average as shown in Figure 7.4. The measurement indicates that the pulse width change as a result of MSR can differ from channel to channel.

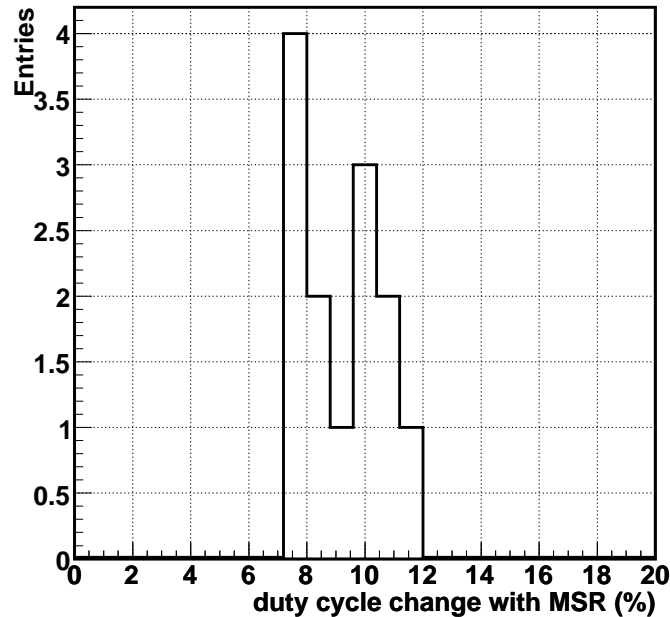


Figure 7.4: *The deduced change on the duty cycle caused by a MSR full range variation. The mean change of the duty cycles is 9.21 % ranging from 7.5 to 12 %. The change of the duty cycle with MSR setting seems to differ from channel to channel.*

The measurement result shown in Figure 7.4 is used to deduce the distribution shown in Figure 7.5 is used as input to the simulation. From the distribution limits of the effect of the MSR on duty cycle. The possible limit of the duty cycle change with MSR setting range is 14 %. However this is just a rough estimate due to the low statistic of the data points that were taken.

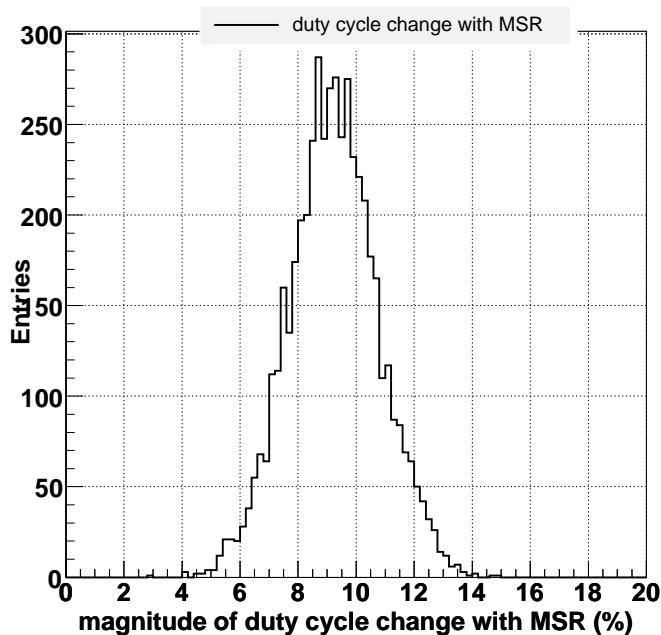


Figure 7.5: *The simulated duty cycle change with MSR. The distribution has an average mean of 9.2 %. The simulation shows the maximum change of the duty cycle with the MSR can be 14 %.*

7.6.1 The MSR and the RX-Threshold

The threshold at the RX-plugin affects the MSR settings. Measurements have shown that the setting of the threshold with respect to the incoming PiN current signal has up to ≈ 8 ns effect on the MSR which translates to a magnitude of up to 16 % change on the positive pulse width. As an example, from Figure 7.6 one illustration is given where the effect is $4.8+1.7=6.5$ ns, which means 13 %. The stable regions of the signals are the regions where there is less change of the displacement from the 25 ns with threshold steps. To set the threshold values, the MSR settings are optimised first. This optimisation means that the BPM signal sent to the detector has no mode hopping thus aligning the on-detector timing.

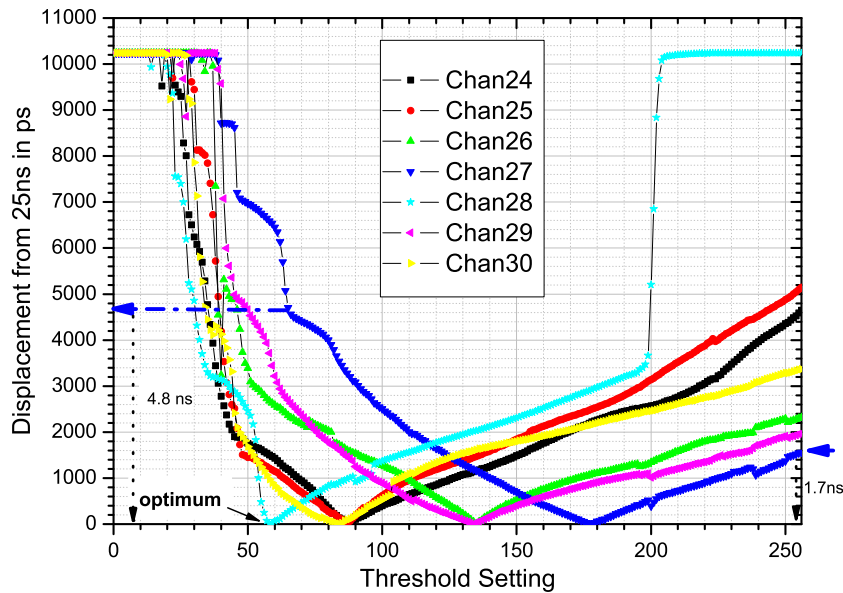


Figure 7.6: *The displacement from 25 ns pulse with respect to the threshold setting shown for one of the two RX-plugins in the System Test. The time difference is deduced from the time length when they enter and leave the stable threshold region. The optimized threshold settings for which the displacement in minimal can be observed.*

7.7 The Fine Delay

With the fine delay the precise detector timing can be achieved. This is done by setting the proper delay corresponding to the module position on the detector and the bunch crossing time. The need for this is critical for the optimizing data taking efficiency. By optimizing the delay the correct hits are allocated to the correct timing window. The magnitude to which the fine delay changes the BPM signal pulse width was measured by varying the delay from setting 0 to 128 stepwise with MSR set to the default value and at a laser power setting of 0xa0. This result is shown in Figure 7.7. From this result the edges are fit linear to obtain the step sizes by which each delay setting varies the rising and the falling edge and the result to this fitting is shown in Figure 7.8. The delay stepping changes the falling and the rising edge differently from channel to channel with differences up to 27 ps deduced from the differences in change of the two edges per channel. This leads to the two edges being displaced by 3.4 ns maximum after a full delay range. This is a negligible effect since no tuning step will require a full range stepping in fine delay.

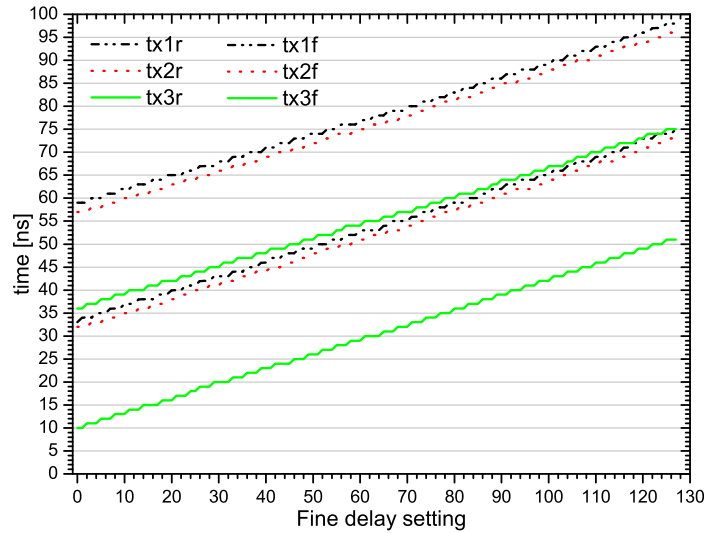


Figure 7.7: A plot showing how the fine delay setting changes the timing of the rising and the falling edges of the BPM signal for 3 channels. The “r” notation in the plot denotes the rising edge and the “f” denotes the falling edge. The linear fit to the curves gives the magnitude of the pulse change with the fine delay setting as varied from setting 0 to 128.

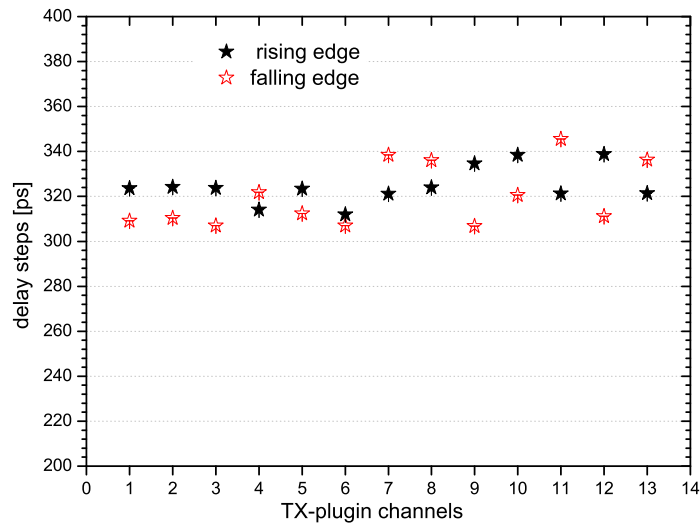


Figure 7.8: A plot showing how one fine delay step changes the delay itself. The measurement points fitted for rising and the falling edges of the 25 ns pulse are shown for 13 channels. The fine delay steps are 324 ps in size on average.

The percent change ranges from 1.24 % to 7.1 %. This is a wide range that needs more statistic to clarify the deviations. The percentage change in duty cycle was calculated from the ratios deduced from the magnitude by which the delayed edges are apart from each other after 127 fine delay steps shown in Figure 7.8. Using a similar relation as shown in equation 7.1 the percentage change is calculated. The result shows a mean change of 4.1 % and a deviation of 1.7 % to the duty cycle.

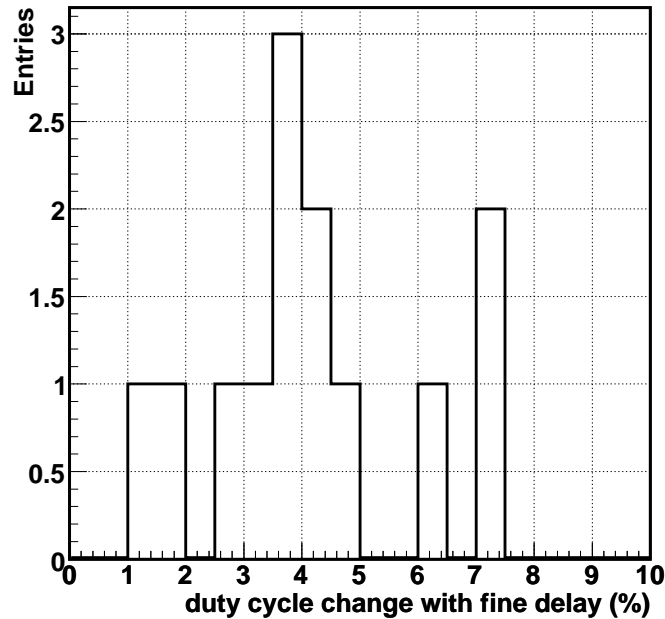


Figure 7.9: *The fine delay effect on the duty cycles of the signal as measured in the system test at the receive section of the BOC card (the RX-plugin). The fine delay alters the positive pulse width by 2 ns on average. This is a magnitude of 4.1% change in duty cycle.*

From the above result the distribution shown in Figure 7.10 can be deduced which is used in the simulation. The distribution shows that the maximum possible change of duty cycle by fine delay stepping is 5 ns which translates to 10 %. The implication of this will be mentioned later sections in relation to the minimum pulse width measured at the TX-plugin.

7.8 The Inter-relation between MSR and the Fine Delay

From the relations of the MSR and the fine delay to the duty cycles the inter-relation between the two parameters which are observed to influence each other can be deduced.

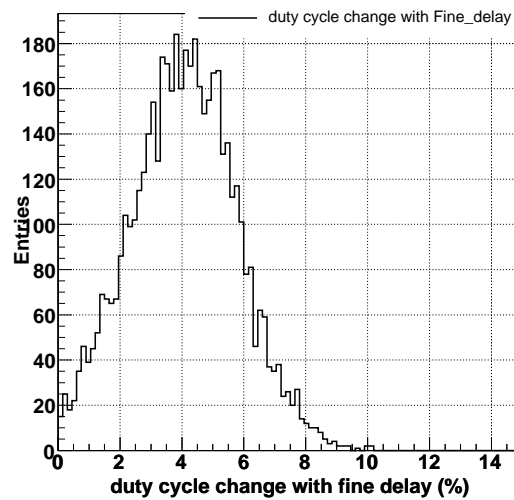


Figure 7.10: *The simulated percentage change of duty cycle with respect to the full fine delay change of 128 settings. The distribution shows an 4.1 % change in the duty cycle on average with a maximum of 10 %.*

The magnitude of influence on each other is important in determining whether the time settings can be precisely retained when the MSR settings are changed.

From the distribution of the MSR in Figure 7.5 and that of the fine delay in 7.10 the influence of the fine delay on the MSR can be deduced. This relation of the interplay between the MSR and the fine delay is shown in Figure 7.11. The effect to the delay of changing an MSR step ($2.49/31=0.08\pm 0.0005$) on average. The effect to MSR of changing the fine delay is ($0.49/127=0.0035$) on average. It can be deduced that changing the MSR after the fine delay is set has a larger effect than changing the fine delay after the MSR is set.

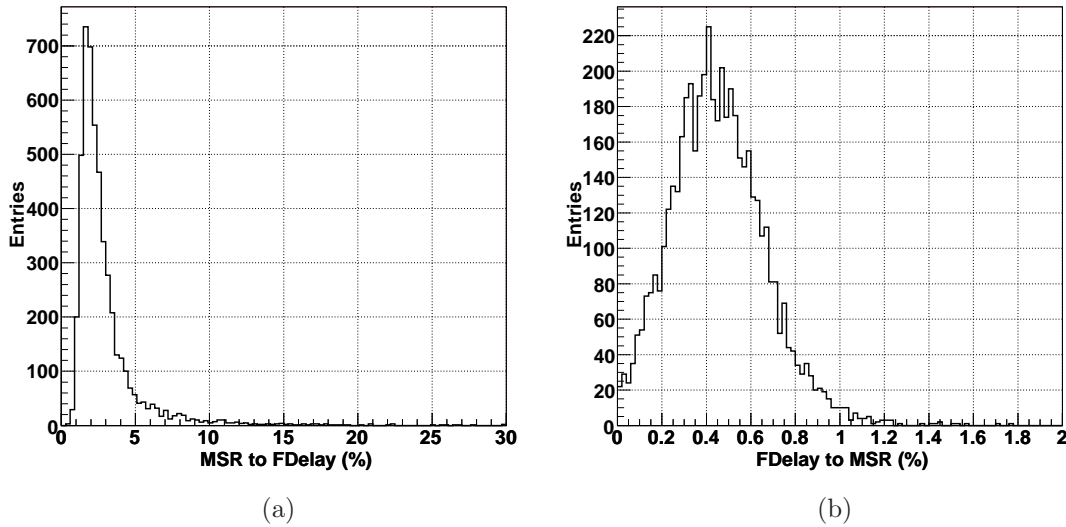


Figure 7.11: *The Inter-relationship between the MSR and the fine delay. The ratio $MSR:finedelay \approx 2.9$ and $finedelay:MSR \approx 0.45$. Changing the MSR after the fine delay is set has a larger effect than changing the fine delay after the MSR is set.*

7.9 The Optimum MSR Settings when No Fine Delay is Applied

To calculate the optimum MSR settings the relation of the MSR to the duty cycles was utilized. These are settings of the MSR at the TX-plugin for which an on detector 25 ns pulse can be achieved. The intersection of the fit to the pulse width changes with MSR, that is at MSR setting 0 gives the value of the initial BPM pulse. This initial value was for one channel measured to be 23 ns as shown in Figure 7.12. It is the initial BPM signal at the TX-plugin. The delay is set to zero in this case. At the maximum MSR setting the measured pulse is 30 ns.

By requiring that the optimal on-detector BPM signal be 25 ns and with least jitter of 0.5 ns which is the tuned required time, the optimal settings at the TX-plugins are calculated. Figure 7.13 shows this result of the optimal MSR settings. This result deviates from what is observed from the measurement. The settings of a tuned system, through measurements are 19 ± 2 settings. Thus the result shows that for one to have a BPM signal with 50 % duty cycle on-detector which is within the measured working settings of the MSR, the optimal BPM optical signal out of the TX-plugin into the optoboard are different from 25 ns. By requiring that the optimal measured settings of the MSR 19 be met the optimal pulse is 26 ns which gives the MSR settings shown in Figure 7.13(b). Hence it can be concluded that BPM signal ending with a 25 ns on detector is not exactly 50 % in duty cycle. The optimum pulse width that is required to set the on-detector 25 ns clock is 26 ± 0.5 ns.

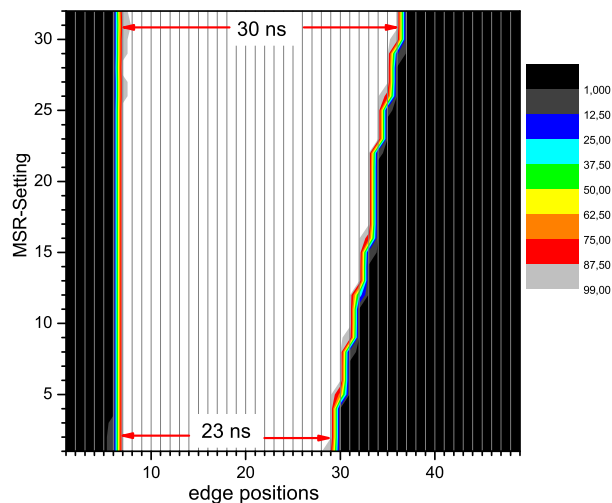


Figure 7.12: The measured pulse width at the TX-plugin in relation to the MSR. The initial pulse width is 23 ns long at MSR setting=0 and the longest pulse is 30 ns at MSR setting=31. The black color region is a '0' and the whiteregion is a '1'. The colors between show the signal transition from '0' to '1'.

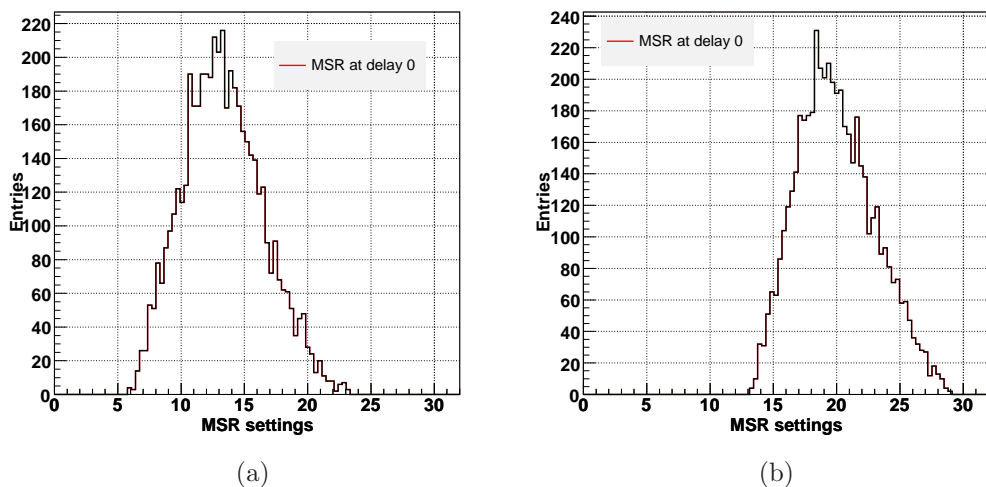


Figure 7.13: The simulated MSR settings at the TX-plugin at delay setting 0. Shown in figure (a) are the MSR settings at the TX-plug in for an exact 50 % BPM signal optical signal. The average MSR setting=13. In Figure (b) the average setting is 19 showing that the optical BPM pulse is 26 ns which corresponds to the tuned system settings.

7.10 The Opto-board PiN Current in relation to MSR and the Fine Delay settings

A measurement of the PiN current at the opto-board was done to access the magnitude by which the MSR and the fine delay affect the optical signal characteristic at 0xa0 laser forward current DAC setting. The measurement of the mean PiN current at the minimum and the maximum setting of MSR and the fine delay is shown in Figures 7.14. It can be observed that the MSR increases the mean PiN current by 30 % on average for the 31 MSR steps, while the fine delay decreases it by 16 % on average for the full 127 steps applied. As expected the MSR has a larger effect on the optical signal characteristic into the PiN than the fine delay and the effect in inverse. The MSR increases the mean PiN current by an approximate of 1 % per MSR step and the fine delay decreases it by an approximated 0.12 % per step.

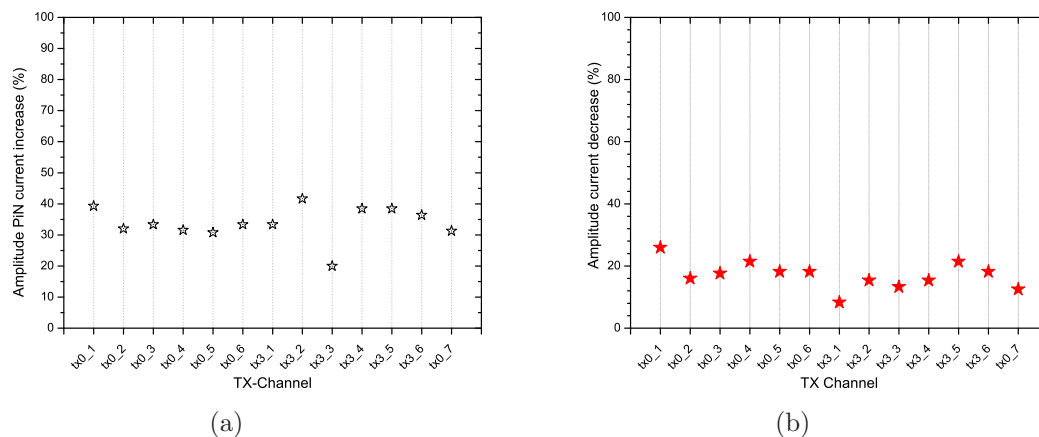


Figure 7.14: *The magnitude by which the MSR and the fine delay changes the shape of the optical signal.*

7.11 The Interplay of Parameters and Tuning

Tuning the optolink can be complicated by the fact of these interplaying parameters. Thus understanding the magnitude of the interrelation was important which will guide to knowing the optimum region and the limits. The work shows the interplay between the MSR setting and the fine delay at a fixed optical power setting of 0xa0 laser DAC setting. From the results in this chapter the ability to tune the system is accessed. From the measurements and the calculation the following useful points to tuning can be summarized:

1. From the relations between the MSR and the fine delay, it can be concluded that there is an inverse behavior of these parameters shown in section 7.8. The effect of

the fine delay on MSR is small. Therefore setting the MSR to the optimal value at delay=0 and then setting the fine delay will have only an effect of 0.3 % on average to the MSR. If an optimal value of $MSR=19\pm 2$ is set adjusting the fine delay by the maximum useful delay of 25 ns, for example, changes the MSR by: $0.003 \times 85 \times 31 \approx 8$ steps on average. This is within the MSR range.

2. The BPM pulse out of the TX-plugin is 26 ns which is needed to have 25 ns pulse on detector as discussed in section 7.9. Thus the minimum allowable pulse ought to be $26-7=19$ ns, where the 7ns is the maximum MSR ratio range. From this one can deduce the maximum allowable change of the pulse width due to delay which is $23-19=4$ ns, where 23 is the measured initial pulse at $MSR=0$. Thus any channel exceeding 8 % change of pulse width due to delay is at the limit.

There are dependencies of these parameters with laser current setting and also the levels of the optical power that that is set to the DORIC. However from the result a working range is always achievable assuming a minimum pulse of 23 ns at $MSR=0$ and if no channel exceeds 8 % duty cycle change by fine delay setting.

7.12 Bit Error Counting in the System Test

Bit error counting was performed within the System Test at Wuppertal. The essential of this measurement was to access the performance of the system in the configuration that reflects an approximate of the actual optolink transmission fibre length and an irradiation degraded system in the possible and achievable way within a laboratory set up. During the detector rest periods, bit error testing can be implemented, thus this becomes a useful study which can be implemented for the Pixel detector readout links. This measurement was done alongside other weekly stability studies on the System Test [54]. As shown in Chapter 6 radiation degraded system and signal amplitude loss due to transmission attenuation is in a summary characterized reduced PiN currents into the DORIC and reduced optical power signal into the RX-plugin. In the laboratory setting, this is simulated by implementation of attenuators as shown in Figure 7.15 illustrating the schematic of the setup utilized for the BER measurement. The low current can in principle be achieved through setting lower laser current using DAQ settings at the TX-plugin for the TTC link and lowering the V_{Iset} setting at the opto-board for the data links. This however undermines the signal quality thus attenuation is preferred.

The system test has 13 links in operation communicating half a bi-stave (13 modules). The front ends are disabled for this measurement. All the nominal power supply configurations were used during this measurement as utilized by the stability measurement study [54]. The configuration unique to this measurement was the attenuation of the links to ≈ -9 dB. Sessions in between the weekly stability measurement were utilized for bit error counting.

For the bit error count measurement a known pattern generated from the ROD was transmitted through the links to the MCC memory FIFOs. This step constitutes the

Measurement session	No. of sent Bits per Link	No. of Errors	Error rate 1 error assumed
1	6.63103×10^8	0	$1.50806 \cdot 10^{-9}$
2	1.12181×10^8	0	$8.91413 \cdot 10^{-9}$
3	3.39531×10^9	0	$2.94524 \cdot 10^{-10}$
4	2.32168×10^9	0	$4.30723 \cdot 10^{-10}$
5	5.79381×10^8	0	$1.72598 \cdot 10^{-9}$
6	1.23794×10^{10}	0	$8.07797 \cdot 10^{-11}$
7	2.33039×10^9	0	$4.29113 \cdot 10^{-10}$
8	6.22138×10^8	0	$1.60736 \cdot 10^{-9}$
8	6.15216×10^8	0	$1.62545 \cdot 10^{-9}$
10	6.39364×10^8	0	$1.56406 \cdot 10^{-9}$
11	3.91489×10^7	0	$2.55435 \cdot 10^{-8}$
12	1.44749×10^8	0	$6.90852 \cdot 10^{-9}$
13	1.17056×10^9	0	$8.5429 \cdot 10^{-10}$
14	8.92004×10^8	0	$1.12107 \cdot 10^{-9}$
15	2.28346×10^9	0	$4.37932 \cdot 10^{-10}$
16	1.4887×10^9	0	$6.71726 \cdot 10^{-10}$
TOTAL	$2.964155 \cdot 10^{10}$	0	$1.1493 \cdot 10^{-12}$

Table 7.1: *The Table summarizes the measurements sessions during the BER measurement done at the system test. The bit count and the error rate is given.*

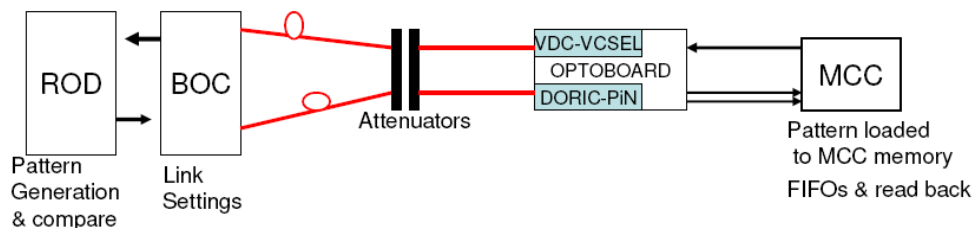


Figure 7.15: *The schematic of the set up utilized for bit error count measurement. The attenuators simulated the fibre length and the link degradation due to irradiation. A known bit pattern was downloaded to the MCC and read.*

downloading of the pattern to the MCC at an approximated rate of 5Mbits/s. Then the pattern was read back to the ROD through the data links at 40 MHz mode. Thus the error counting was on the basis of comparing the bit pattern sent to the bit pattern received back. The first 5 sessions of measurement (see Table 7.1) were taken with PiN current settings on 7 links having an average of current amplitude $50 \mu\text{A}$ and with three links operating at $16 \mu\text{A}$, $22 \mu\text{A}$ and $35 \mu\text{A}$ current amplitude at the RX-plugin. The rest of the amplitude PiN currents at the RX-plugin are shown in Figure 7.16 for which the

setting was maintained for 11 out of the 16 counting sessions.

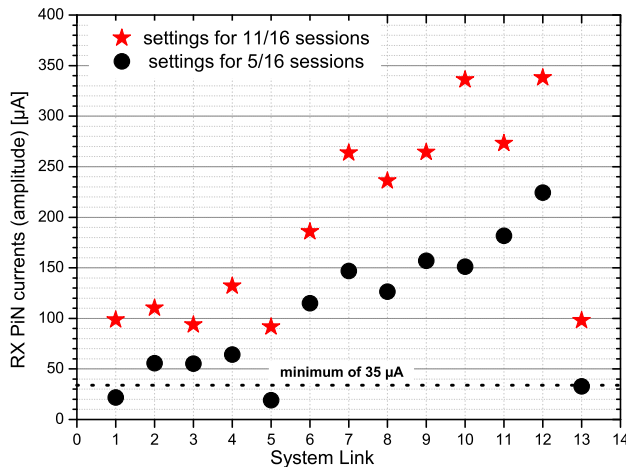


Figure 7.16: *The System test RX-plugin PiN currents at which bit error counting was done. For the 11/16 sessions the Pin currents were $\approx 200 \mu\text{A}$ on average with 4 links having amplitude PiN currents below $100 \mu\text{A}$. For 5/16 sessions the current 7 links operated at an average $50 \mu\text{A}$. Generally the data links were able to work at RX-amplitude PiN currents below $350 \mu\text{A}$.*

In 4 data links the PiN current was between 90 and $100 \mu\text{A}$ for the later sessions. A setting of $35 \mu\text{A}$ can be taken as a safe stable minimum going by no error counts observed for the first five sessions.

The amplitude current of the TTC links at the opto-board are also shown in Figure 7.17 these currents are at the mid-region.

Table 7.1 summarizes the measurement sessions and the error rate. The bit error rate assuming one error was calculated using the formula:

$$\text{BER} = \frac{\text{error counts}}{\text{total transmitted bits}} \quad (7.2)$$

In Chapter 6, it has been shown that the ATLAS Pixel optical links will experience worst case total attenuation of -5 dB . The operation of the TTC links has shown stability at PiN currents $250 \mu\text{A}$ on average. From the simulation in Chapter 6 the TTC links will operate at this average. Thus the operations of the 13 links in the System Test indicate that the links can operate stably. TTC links have actually shown good performance deducing from many tests done at near DORIC thresholds of $40 \mu\text{A}$ during production measurements.

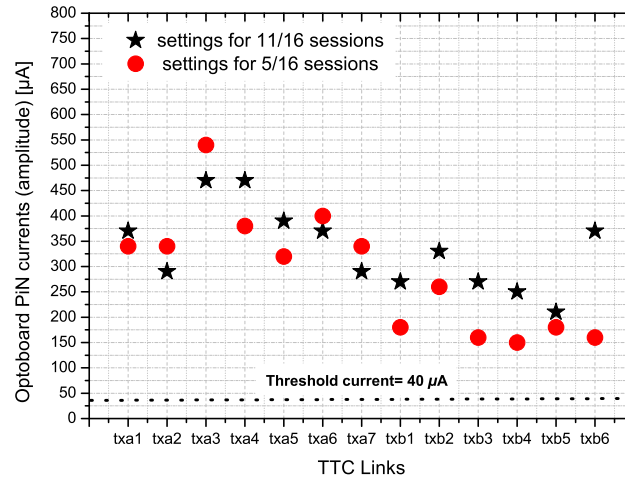


Figure 7.17: *TTC PiN currents at the opto-board, the setting for which the bit pattern has been downloading to the MCC. The currents are in the mid region.*

7.13 Conclusion

The measurements and the calculation in this chapter are useful in accessing the ability to always tune the system. The statistic for this study was however since only 13 links were used. From the inter-relation between the MSR and the fine delay, it has been shown that the inverse property of the two parameters enables that the system can be tuned provided the influence of the delay on MSR is not large to exceed more than 8 % effect on duty cycle. By the BER measurement a stability checking of the optolink was done. However again, the statistic is low since the rate of pattern transfer to the MCC was slow. It can be recommended for the Pixel optolink to keep accessing the link quality during the detector rest sessions. The enhancement of this test to cover the whole system can be done.

More data points are required to enhance the timing calculations. This can be done when the Pixel optolink detector system is set in place at CERN.

Conclusion and Outlook

A careful assessment of the hardware components being installed in the detector is very important. The ATLAS Pixel sub detector will be read out and be controlled by use of an optical transmission link.

The opto-board, placed on detector, interfaces the optical transmission and the on-detector electronics. This thesis has presented an analysis of the opto-board production data. Apart from the known problem with the VCSELs, the opto-board properties met the qualification limits. The TTC links on the opto-board have shown no problem of functionality. But the VCSEL signal continues to pose a challenge in relation to operation at lower temperatures ($-10\text{ }^{\circ}\text{C}$) and in relation to slow turn on. These problems are being investigated at CERN and a decision to implement opto-board heaters has been reached [49].

The data obtained from the production has then been utilized in the optical power simulation which enables understanding, beforehand the functionality of the link in relation to the optical signal transmitted for both TTC and the data link. The optical signal will face the fiber and irradiation degradation challenge, but according to the calculation there is sufficient optical signal amplitude for operation during the next 10 years.

The description of the timing characteristics presented in this work gives the knowledge of the interplaying parameters during tuning. For this specific study the statistic is lacking but it was possible to deduce the tunability of the system by a characterization and a simulation study of the parameters using the available data points.

List of Figures

1	The Large Hadron Collider at CERN	1
1.1	QED Feynman graphs	6
1.2	QCD Feynman graphs	8
1.3	The lowest order <i>top</i> – <i>quark</i> production QCD processes	10
1.4	The main top decay mode	10
1.5	The $t\bar{t}$ branching ratios	11
1.6	The higgs scalar potential	13
1.7	The higgs production cross section	14
1.8	The branching ratios for the SM higgs	15
2.1	Collision activity	18
2.2	The Cross Section of Processes	19
2.3	ATLAS experiment Schematic	21
2.4	Monitored drift tubes	22
2.5	Electromagnetic calorimeter	23
2.6	The ATLAS Trigger scheme	25
2.7	LVL1 trigger system	26
2.8	The High Level Trigger	27
3.1	The Pixel detector layout	29
3.2	The Pixel module schematic	30
3.3	A Bi-stave	31
3.4	The Pixel sector	32
3.5	The Sensor Silicon bulk	34
3.6	Pixel sensors under irradiation	35
3.7	Bethe-Bloch curve	36

3.8	The Pixel cell	37
3.9	Energy deposition in the sensor	38
3.10	The module controller chip logic	39
3.11	Event Data format at the MCC output	40
4.1	The Pixel detector Readout chain	43
4.2	The ROD and BOC card overview	45
4.3	On-Detector electronics communication flow	46
4.4	The TX-plugin and the TTC sending	47
4.5	BPM encoding	48
4.6	The BOC receiving signal processing	49
4.7	The Opto-board	49
4.8	The VCSEL Optopack	51
4.9	DORIC circuit	52
4.10	The DORIC decoding logic	53
4.11	DORIC thresholds during irradiation	54
4.12	The VDC circuit	54
4.13	V_{Iset} to I_{Iset} relation	55
4.14	The optical linking infractructure	57
4.15	The "Y" cable at the PP1	57
4.16	Connector types utilized at the PP1	58
5.1	The Opto-board production set up	59
5.2	Opto-board production process steps	60
5.3	Components in the full loop-back mode	64
5.4	Measured optical power of standardizing measurements	66
5.5	Optical power rise and fall time	66
5.6	Decoded data and clock signal amplitude	67
5.7	The electrical duty cycle	67
5.8	The optical power of the VCSEL 260 opto-packages	69
5.9	Optopower ratio	70
5.10	Responsivities of 470 Opto-boards	70
5.11	The I_{vdc} behavior during burn in	72
5.12	Power consumption of the opto-boards during burn-in	73

5.13	A typical thermal testing phase	74
5.14	The decoded DORIC clock and command signal measurement set-up	75
5.15	The clock duty cycle and clock positive width jitter	76
5.16	The decoded 40 Mhz clock signal rise and fall time	77
5.17	The decoded command PRBS signal rise time and fall time	77
5.18	VCSEL signal characterization set up	79
5.19	Optical power at the nominal setting of 0.9 V	80
5.20	The optical power at the nominal setting of 0.9 V at -10 °C	80
5.21	The optical power ratios	81
5.22	The optical power at the saturation region	82
5.23	The optical power at $V_{Iset}=1.2$ V	82
6.1	Measured and fitted attenuation for TTC	89
6.2	Measured and fitted attenuation for PP0 to PP1	89
6.3	The total attenuation of the data lines	92
6.4	Total attenuation of the TTC lines	92
6.5	Fraction of power lost by the VCSEL as a result of irradiation	93
6.6	The logic output signal of the RX-plugin	95
6.7	The RX-plugin working range	96
6.8	Opto-board power measured during the Q/A	97
6.9	Opto-board power before and after irradiation at setting of 0.9 V	97
6.10	Optical signal into the RX-plugin PiN	98
6.11	Minimum power at the opto-board needed to meet the minimum RX-plugin	99
6.12	RX-plugin working range and at highly attenuated fibre coupling	100
6.13	Optical power dispersion	101
6.14	Opto-board power at ≈ -10 °C before and after irradiation.	102
6.15	The PiN current at the RX-plugin for optical power at -10 °C	102
6.16	The power spread at approximately -10°C	103
6.17	Measured optical power at the default RX-plugin settings	104
6.18	Optical signal into Opto-board PiN diode at the 0xa0 laser settings	104
6.19	PiN responsivities of the opto-board simulated based on production	105
6.20	The TTC signal PiN current into the DORIC	106
6.21	DORIC thresholds, measured at Siegen	106
6.22	Opto-board PiN current signal the for maximum TX-laser setting	107

6.23	The minimum optical power setting needed at the TX-plugin for $40 \mu\text{A}$. . .	108
6.24	Demonstrating the limits for a highly attenuating fibre	108
7.1	The schematic of a typical System Test	112
7.2	The effect of MSR on the on-detector clock at 0xa0 and 0xff	115
7.3	The 25 ns positive width rising and falling edges against the MSR	116
7.4	The change of the positive pulse width with MSR setting	117
7.5	The simulated duty cycle change with MSR	118
7.6	The displacement from 25 ns pulse with respect to the threshold	119
7.7	Fine delay and the pulse width	120
7.8	A plot of the fine delay setting changing the delay itself	120
7.9	The fine delay effect on the duty cycles	121
7.10	The simulated percentage change of duty cycle with fine delay	122
7.11	The inter-relation between the MSR and the fine delay	123
7.12	The measured pulse width at the TX	124
7.13	The simulated MSR settings at the TX-plugin at delay setting 0	124
7.14	The optopower MSR and the fine delay	125
7.15	The set up utilized for BER measurement in the System test	127
7.16	The System Test RX-plugin PiN currents during BER	128
7.17	TTC PiN currents at the opto-board during BER	129

List of Tables

1.1	Standard Model elementary particles	4
1.2	The dimensionless constant α	5
1.3	CKM Matrix	8
1.4	The $t\bar{t}$ quark final topologies	11
2.1	The LHC machine parameters	19
3.1	Pixel module geometrical positions	32
4.1	I_{Set} at $V_{Iset}=0.9$ V	55
5.1	A summary of the opto-board components	61
5.2	Opto-board quality assurance limits	62
5.3	The measurements sets	68
5.4	Opto-board production yield during Q/A	83
6.1	The irradiation levels	90
6.2	The attenuation values due to irradiation on the SIMM fibre	90
7.1	The Bit Error Rate	127

Bibliography

- [1] CERN Press office Photo Selection. <http://press.web.cern.ch/press/Photo-Database/welcome.html>
- [2] arXiv:hep-ph/0205126v2., *(FINAL) HIGGS RESULTS FROM LEP*. 14th may 2002.
- [3] Journal Of Particle physics. Nuclear and particle physics. Vol 33. July 2006. pg 390
- [4] The LEP Collaborations and the LEP Electroweak Working Group, as reported by J. Dress at the XX International Symposium on Lepton and Photon Interactions at High Energy, Rome, Italy (July 2001).
- [5] J. Drees *Comments: Proceedings of the International Symposium on Lepton and Photon Interactions at High Energies*. Rome, Italy, July 2001 Journal-ref: Int.J.Mod.Phys. A17 (2002) 3259-3283.
- [6] F. Halzen and A.D Martin. *Quarks and Leptons: An introductory Course in modern Particle Physics*. Ed. John Willey, New York, 1984.
- [7] Martin B.R and Shaw G., *Particle Physics*. Wiley and Sons. Second Edition pg 188-190.
- [8] H. Bele et. al. *Quark Mixing, The CKM Unitary Problem*. Eur.Phys. J. C 33, 1-8 (2004).
- [9] T.Affolder et al, *Physics Review D*63, 032003 (2001)
- [10] B. Abbot et al, *Physics Review D*60, 052001 (1999)
- [11] Z. Sullivan, *Physics Review. D* 66, 075011 (2002).
- [12] V. M. Abazov et al., *$t\bar{t}$ production cross section in $p\bar{p}$ collisions at $\sqrt{s}=TeV$* PHYSICAL REVIEW D 67, 012004 2003.
- [13] I. Borjanovic et al., *Investigation of top mass measurements with the ATLAS detector at LHC*. SN-ATLAS-2004-040.
- [14] W. N. Cottingham and D. A. Greenwood., *An introduction to the standard model of particle physics*. Cambridge Univ. Press. 1998.

- [15] Abdelhak Djouadi *The Anatomy of Electro-Weak Symmetry Breaking. I: The Higgs boson in the Standard Model*. arXiv:hep-ph/0503172v2. May 2005
- [16] F Gianotti *Collider Physics at LHC. European school of High Energy Physics*, ATLAS Note ATL-CONF-200-001,2000.
- [17] D. Denegri. *Standard model physics at the LHC (p-p collisions)*. Large Hadron Collider Workshop, volume 1. CERN, October 1990. CERN-90-10-V-1.
- [18] The ATLAS Technical Design Report, CERN, 1999. Design Report
- [19] M Elsing and T. Schörner-Sadenius., *Configuration of the ATLAS Trigger System*. Atlas Note. ATL-DAQ-2003-038.
- [20] F. Hugging et al. *Design and test of pixel sensors for operation in severe radiation environments*. Nucl. Instrum. Meth., A439:529, 2000.
- [21] K. E. Arms et al. *ATLAS Pixel Opto-Electronics*, Nuclear Instruments and Methods in Physics Research A 554 (2005) 458-468.
- [22] Michael Moll., *Radiation Damage in Silicon Particle Detectors - microscopic defects and macroscopic properties*. PhD thesis, desy-thesis-99-040. DESY Hamburg, 1999.
- [23] Shota Shanava. New uncoated stave. Technical report, CERN, 2006.
- [24] CERN. Integration photos. <http://atlas-pixel.mi.infn.it/wiki/index.php/>
- [25] R. Wunstorf et. al., *Radiation of Silicon Detectors by Monoenergetic Neutrons between 1 and 14 MeV and 1.8 MeV Electrons*, Nuclear Physics B 23A. 1991
- [26] R. Wunstorf *Radiation Tolerant sensors for Atlas-Pixel Detector* Nucl. Instr. and Methods In Physics Research. A 466 (2001) 327-334.
- [27] Michael Moll., *Radiation Tolerant Semiconductor Tracking Detectors for SUPER-LHC*, Seminar, Bergische Universität Wuppertal, 16. June 2005
- [28] Tobias Flick., *Studies on the Optical Readout for the ATLAS Pixel Detector Systematical Studies on the Functions of the Back of Crate Card and the Timing of the Pixel Detector*. PhD thesis, University of Wuppertal, WUB-DIS 2006-5, July 2006.
- [29] T. Rohe. et al., *Sensor design for the ATLAS-pixel detector*. Nuclear Instruments and Methods in Physics Research A 409 (1998) 224-228
- [30] Glenn Knoll., *Radiation Detection and Measurement*, 3rd Edition, Wiley, New York, 2000;
- [31] Christian Grah., *Development of the MCM-Technique for Pixel Detector Modules*. PhD thesis, Bergische Universität Wuppertal, March 2005. pg 27.

- [32] Landau L., On the energy loss of fast particles by ionization. *J Phys (USSR)* 8:201, 1944.
- [33] R. Beccherle et al. *MCC: The Module Controller Chip for the ATLAS pixel detector*. NIM-A, 492:117-133, 2002.
- [34] Andreas Korn., *How to readout a 80 million channel Silicon Pixel Detector*. A talk at Uni-Wuppertal, 1 June 2006.
- [35] Maurice Goodrick. *BOC - The Back of Crate interface for the SCT ROD*. Technical report, Cavendish-Laboratory, Cambridge, 2003.
- [36] M. L. Chu et al. *The off-detector opto-electronics for the optical links of the ATLAS semiconductor tracker and pixel detector*. Nucl. Instrum. Meth., A530:293-310, 2004.
- [37] G Mahout et al., *Radiation Hardness and Lifetime Of VCSELs and PiN Photo diodes For use in the Atlas SCT*, Proc. SPIE Vol 4134, p.206-213, Photonics for Space Environment.
- [38] Alexander Ciliox. *Radiation hardness tests of the optical data transmission system of the ATLAS pixel detector*, Diplomarbeit, Universität Siegen, April 2003.
- [39] Simon Kirichu Nderitu. *Evaluation of the Optical Data Transmission System for the ATLAS Pixel Detector*, M.Sc Thesis, University of Siegen, January 2004.
- [40] Axel Roggenbuck *Untersuchungen zur Strahlenhärte des optischen Datenübertragungssystems für den ATLAS-Pixeldetektor* Diplomarbeit, Universität Siegen, Dezember 2005.
- [41] Ingrid-Maria Gregor., *Optolinks for The Atlas Pixel Detector*. PhD Thesis. Uni-Wuppertal. WUB DIS 2001-03.
- [42] True Light. TSD-8B12-000, *High Performance Oxide-Confined VCSEL*, Specifications Sheet Rev. 2.03.
- [43] Paul D. Jackson. *Radiation-Hard Optical Link for the ATLAS Pixel Detector*, Presentation CAP congress, 8. Juni 2005.
- [44] G.Mahout et al, *Irradiation studies of multimode optical fibres for use in ATLAS front-end links*, Nuclear Instruments and Methods in Physics Research A 446 (2000) 426-434.
- [45] Atlas doc, *Minutes of the ATLAS Front end Link Working Group and Irradiation scheme* <http://atlas.web.cern.ch/Atlas/GROUPS/FRONTEND/links/minutes/sept99-minutes.html>

- [46] Minglee Chu, *On Detector Array Opto Pakage For Pixel Production and Quality Assuarance*, Pixe PRR document, <http://www-hep.phys.sinica.edu.tw/atlas/PIXEL/PRR/opto-array.pdf>
- [47] K.K. Gan, et al., *Opto-board Assembly Procedure* ATLAS Project Document No ATL-IP-AP-0014.
- [48] K.K. Gan and Michail Ziolkowski. Atlas Doc. *Atlas Pixel Opto-Board QA*, ATL-IP-QA-0014
- [49] Personal communication with Atlas opto-link Taskforce. <https://twiki.cern.ch/twiki/bin/view/Atlas/OptoLinkTaskForce>
- [50] Ohio production website. <http://www.physics.ohio-state.edu/gan/optoboard/optoboard.html>
- [51] ATLAS Project Document ATL-IP-ER-0007. *Pixel Detector Optolink, On- and off detector optoelectric components*, modified 19.02.2003.
- [52] J. Weingarten et al., *Experiences with module-production and system tests for the ATLAS Pixel Detector* Proc. Pixel 2005, Bonn, 5-8 Sep., 2005;
- [53] Jens Dopke., *Studies for Automated Tunning of the Quality of thr Back-of-Crate Card for the Atlas Pixel detector*. WU D 07-02. February 2007.
- [54] Jenny Flügge., *Das Langzeitverhalten des Wuppertaler Systemtests für den ATLAS Pixeldetektor*.

Erklärung

Hiermit versichere ich, dass ich diese Arbeit selbstständig verfasst und keine anderen als die angegebenen Quellen und Hilfsmittel benutzt, sowie Zitate kenntlich gemacht habe.

Acknowledgements

My heartfelt appreciation goes to all those who contributed towards the realisation of the work in this thesis by offering all kind of help as expected in collaborative research, without which progress and completion would not have been possible. If i were to list each one them and what invaluable thing they did i would have to dedicate much space for that. I will however point out a few who had a key role. The work may not be award winning, but i feel so previlaged to have made a contribution towards such a groundbreaking experiment.

Prof. Dr Peter Maettig, thanks, first of all for the oppotunity you gave me to do this work and in addition, your supervision and great support as my “Doktorvater”. Dr. Peter Gerlach, many times you were over my shoulder looking over. Thanks for your advice, discussssions and close supervision. Dr. Kendall Reeves, you just know that you had timely “words of wisdom from experience” for me. Dr. Tobias Flick thanks for the discussions especially for the work in chapter 6. Jens Dopke and Andreas Korn(LBNL), thanks for the discussions on work in chapter 7. I thank Dr. Michael Ziolkowski (Uni-Siegen) and Ohio State University optolink team for the discussions on work in chapter 5. Peter kind, thanks for your technical assistance. I also acknowledge those others who were working in the Detector lab, either for study or the technical stuff, between January 2003 and April 2007, who contributed towards this work through related discussions or by technical assistance.

Sue, my wife you are a strong lady. I love you. Many are the times i had to be away in the lab or in the house, closed in, working to finish this work. Given that Steve and Sheena (born during this work) were small and needing much attention, you endured the great pressure. You know we owe it only and only unto God’s grace that we went through to the end. Stephe, Steve and Sheena you motivated me. Your little smiles brightened tough moments.

Finally: I would consider this work greatly lacking if i would not recognise my very special Friend even the Lord Jesus Christ, the Son of the living God. All that is said about You in Your Word is true: For by You were all things created, that are in heaven, and that are in earth, visible and invisible, whether they be thrones, or dominions, or principalities, or powers: **all things were created by you, and for you: And you are before all things, and by you all things consist** (Col 1:16,17 KJV). Therefore, would i say that i have worked to know or have measured or concluded something of your creation without acknowledging you?...no! i will not trespass your work, therefore you deserve all of my thanksgiving and acknowledgement. I deeply appreciate your grace.